MSc thesis in Electrical Engineering

Impact of Antenna Gain Distortions due to Bumper Presence in DoA Estimation for Automotive Radar

by

Freya Ningyuan Ma

to obtain the degree of Master of Electrical Engineering
at the Delft University of Technology,
to be defended publicly on **Jan, 2026**

Student number:	5814987
Project duration:	May., 2025 – Jan., 2026
Thesis Supervisor:	Prof. Dr. Yanki Aslan, TU Delft

An electronic version of this thesis is available at http://repository.tudelft.nl/.

The work in this thesis was carried out in the:

Microwave Sensing, Signals and Systems (MS3) Group
Department of Electrical Engineering, Mathematics and Computer Science (EEMCS)
Delft University of Technology

Abstract

This thesis investigates the impact of realistic electromagnetic impairments, such as bumper obstruction and rainwater deposition, on automotive MIMO radar Direction of Arrival (DoA) estimation. This study incorporates high-fidelity realized gain patterns directly into FMCW MIMO radar simulations and assessing Beamscan, MUSIC, and MVDR under both deterministic and stochastic scenarios. The methodology includes CST modeling of antennas and bumpers with water-layer and droplet effects, deterministic DoA analysis at representative high- and low-gain angles, and statistical simulations of RMSE and MAE to evaluate algorithm robustness. Results show that Beamscan is sensitive to amplitude loss, while MUSIC consistently achieves the lowest RMSE and MAE. MVDR algorithm achieves higher RMSE compared to MUSIC, indicating lower overall accuracy, yet it is relatively insensitive to signal amplitude attenuation. The framework provides a replicable pipeline linking EM level antenna degradation to DoA performance. These findings provide practical guidance for radar system design and highlight the necessity of optimized signal processing strategies for reliable automotive angle estimation in real life scenorio.

Contents

1 Introduction **3**

1.1 Motivation: Automotive MIMO Radar and ADAS . . . 3

1.2 Problem formulation: Direction of Arrival Estimation in Automotive Applications under EM effects . . . 5

1.3 Research Objectives . . . 5

1.4 Literature Study . . . 6

1.4.1 EM effects of bumpers on radar signal propagation . . . 6

1.4.2 DoA algorithms . . . 7

1.4.3 Gaps in the literature . . . 8

1.5 Thesis scope and novelties . . . 8

1.6 Thesis structure . . . 9

2 Electromagnetic and Environmental Modeling **11**

2.1 Subarray Antenna Design . . . 11

2.2 Material Effects on Signal Transmission . . . 14

2.3 Bumper Model . . . 16

2.3.1 Bumper Structure Modeling . . . 16

2.3.2 Impact of Bumper-to-Antenna Distance . . . 19

2.4 Rainwater Modeling on Bumper Surface . . . 19

2.4.1 Thin Film Layer Model . . . 19

2.4.2 Discrete Droplet Models . . . 24

2.5 Higher Resolution Antenna Model . . . 25

2.6 Conclusion . . . 27

3 DoA Estimation Algorithms **31**

3.1 FMCW Waveform and MIMO Configuration . . . 31

3.1.1 FMCW Parameters . . . 31

3.1.2 MIMO Configuration . . . 32

3.2 Beamscan Algorithm . . . 33

3.2.1 Beamscan Algorithm Overview . . . 33

3.2.2 Antenna–bumper–water layer analysis . . . 34

3.2.3 Antenna–bumper–water droplets analysis . . . 37

3.3 MUSIC Algorithm . . . 38

3.3.1 MUSIC Algorithm Overview . . . 38

3.3.2 Antenna–bumper–water layer analysis . . . 39

3.3.3 Antenna–bumper-water droplets analysis . . . 40

3.4 MVDR Algorithm 40
3.4.1 MVDR Algorithm Overview 40
3.4.2 Antenna–bumper–water layer analysis 44
3.4.3 Antenna–bumper–water droplets analysis 44
3.5 Conclusion 47

4 Statistical Results and Comparative Analysis **50**

4.1 Performance Evaluation 50
4.1.1 Beamscan Algorithm 51
4.1.2 MUSIC Algorithm 54
4.1.3 MVDR Algorithm 59
4.1.4 Conclusion 63
4.2 Conclusion and Recommendations for Future Work 64

1 Introduction

1.1 Motivation: Automotive MIMO Radar and ADAS

Autonomous driving technologies have attracted more attention from academia and industry because to the quick development of intelligent transportation systems. Advanced Driver-Assistance Systems (ADAS) have become crucial elements, designed to improve driving safety and comfort through a collection of onboard sensors. ADAS generally encompasses several essential functions: Blind Spot Detection (BSD), Intelligent Headlamp Control (IHC), Adaptive Cruise Control (ACC), Lane Departure Warning and Keeping Systems (LDW/LKS), and Emergency Brake Assist (EBA)[1].

These functions rely on sensors integrated into vehicles-such as cameras, LiDAR, ultrasonic sensors, and notably radar-are to precisely detect the surrounding environment so as to assist drivers in real time [2]. Reliable ADAS requires that it must be equipped with advanced sensing capabilities that provide real-time awareness of the driving environment. These include identifying the positions of surrounding vehicles, estimating traffic density, detecting objects on the road, and evaluating distances to nearby vehicles from all directions.

Radar (Radio Detection and Ranging) is a critical sensing technology that plays a central role in modern vehicle safety systems. It serves as a fundamental component of ADAS in automotive applications. Radar operates by transmitting electromagnetic signals toward targets and interpreting the reflected echoes to detect, locate, and identify objects. Modern vehicles integrate multiple radar units with different ranges and placements to ensure comprehensive environmental perception. For example, long-range radars (LRR) are typically mounted at the front of the vehicle for adaptive cruise control; medium-range radars (MRR) at the front and rear assist with cross-traffic alerts and lane changes; and short-range corner radars (SRR) are utilized for blind spot monitoring and low-speed maneuvers such as parking and pedestrian detection[3]. These radars operate collaboratively to enhance sensing robustness.

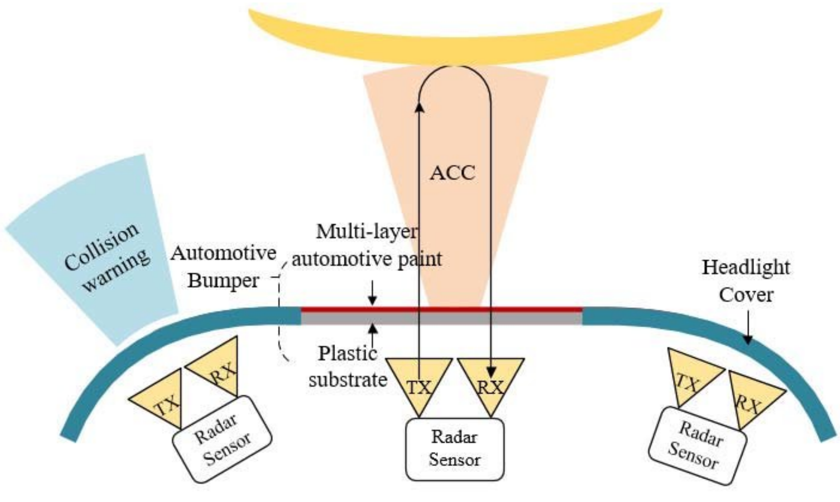

Figure 1.1: Schematic Layout of Automotive Radar Sensor (Radar installed behind the bumper) [4]

As vehicles advance toward higher levels of driving automation, as defined by the Society of Automotive Engineers (SAE), radar systems must meet increasingly stringent performance criteria. These include higher spatial resolution, faster response times, greater resilience to interference, and robust performance under adverse weather and environmental conditions. The development of Level 3 to Level 5 autonomous vehicles, which involve minimal to no human intervention, further amplifies the need for reliable radar-based perception systems [2]. These systems must also integrate seamlessly with other sensor modalities (e.g., LiDAR, cameras) and support advanced signal processing techniques such as high-resolution Direction-of-arrival (DoA) estimation to accurately localize and track multiple dynamic objects in real time.

The 76–77GHz (for long-range radar) and 77–81GHz (for short-range radar) bands are allocated specifically for automotive radar in many countries. These high-frequency bands are preferred due to several advantages. The 77GHz band offers over 4GHz of bandwidth, which improves range resolution and enables better distinction between nearby targets. Higher frequencies also yield more accurate velocity measurements and allow for smaller antenna designs due to shorter wavelengths, which is crucial for the compact and high-precision requirements of automotive integration. Furthermore, regulations for the 77GHz band permit higher transmit power [3].

For automotive radars, FMCW waveform is currently the most widely used waveform due to its convenience in generation by a phase-locked loop (PLL), as well as the high efficiency in obtaining the range information from the baseband. While range and Doppler parameters can be effectively derived using a single receive antenna [5], accurate estimation of the angular location of targets, commonly referred to as Direction of Arrival (DoA), necessitates the deployment of antenna arrays.

Arrays combine multiple sensors to achieve beamforming or interference suppression. Sampling theory governs array design, where element spacing must satisfy spatial Nyquist criteria to avoid aliasing[6]. The spatial resolution of a sensor is fundamentally governed by its aperture size and shape. Larger apertures yield narrower mainlobes in the aperture smoothing function, enabling finer angular separation of plane waves. Finite apertures introduce trade-offs between resolution (larger apertures) and practical constraints (e.g., size, cost).

The limitations of conventional single-antenna setups in angular resolution have led to the adoption of Multiple-Input Multiple-Output (MIMO) radar systems, which offer substantial advantages in terms of spatial resolution and system flexibility [3]. MIMO radar systems employ multiple transmit and receive antennas arranged in a configuration that enables the synthesis of a larger “virtual array.” By ensuring the orthogonality of transmitted waveforms, contributions from individual transmit antennas can be distinguished at the receive side. This configuration significantly enhances the angular resolution of the radar system, which makes it well-suited for automotive applications. For example, it is essential for distinguishing between low-profile obstacles that can be safely driven over and hazardous situations such as large vehicles with ground clearance that may deceptively appear as passable spaces — so-called drive-over and drive-under detection.

Furthermore, the incorporation of MIMO radar technology aligns with the increasing complexity of autonomous driving systems, which demand reliable and precise object localization. The high-resolution DoA capability of MIMO radars supports essential functions such as obstacle detection, lane change assistance, and pedestrian tracking, making them indispensable components of modern vehicular sensing platforms.

1.2 Problem formulation: Direction of Arrival Estimation in Automotive Applications under EM effects

In automotive radar systems, DoA estimate is a crucial function that enables accurate localization of objects within the surroundings. Precise angular estimation is essential for numerous safety-critical applications, including adaptive cruise control, lane maintaining, and collision avoidance. Conventionally, DoA estimation techniques are formulated under idealized circumstances, presuming free-space propagation and disregarding the effects of materials or structures intervening between the radar antenna and the surrounding environment.

However, in most commercial implementations, automotive radar sensors are mounted behind the vehicle bumper for aesthetic and aerodynamic reasons. These bumpers are typically made of frequency-sensitive dielectric materials and may consist of multiple layers, typically paint coatings. As the radar signal propagates through the bumper, it undergoes various electromagnetic (EM) interactions, such as reflection, refraction, attenuation, and phase distortion. These effects, unless they are somehow calibrated, alter the spatial characteristics of the received wavefronts, introducing errors in DoA estimation that are not captured by standard models.

Furthermore, real environmental conditions-such as water, dirt, or snow on the bumper surface-exacerbate the complexity of the signal transmission path. These non-idealities may induce spatially non-uniform and perhaps temporally variable distortions, resulting in biased or impaired DoA outputs. Inaccurate angular information could be produced by current radar systems if these elements are not taken into consideration, which would ultimately affect the reliability of autonomous perception and decision-making.

Despite their practical significance, bumper-induced electromagnetic effects have not been routinely integrated into the design or assessment of direction of arrival estimation systems. The deficiency in modeling and simulation undermines the reliability of existing car radar systems, especially under real-world operational settings.

These observations underscore a significant gap between real-world automotive radar implementations and the foundational assumptions of traditional DoA estimation models. Addressing this gap necessitates a methodical examination of bumper-induced electromagnetic effects and their influence on DoA performance in realistic operational contexts.

1.3 Research Objectives

This thesis aims to conduct a preliminary study on the impact of bumper structures and environmental contaminants on electromagnetic signal propagation in automotive radar systems, as well as how these factors affect DoA estimate performance. This study focuses on modeling a 77 GHz radar antenna array and simulating its interaction with actual bumper configurations, which include polymer materials, paint layers, and surface contaminants (water), utilizing full-wave electromagnetic simulation techniques. The signal model is developed under simplifying assumptions in EM (e.g. same common distorted pattern for all subarrays) for the first-order analysis of gain distortions in DoA estimation.

This study assesses the performance of the DoA algorithm under modified signal conditions based on these simulations and offers insights into EM-aware DoA estimate concerns. The primary aim is to improve the understanding of DoA robustness in radar systems operating in real-world environments.

1.4 Literature Study

1.4.1 EM effects of bumpers on radar signal propagation

The vehicle bumper, located at the front and rear ends, is primarily composed of polymer materials and a multi-layered paint system [7]. Most bumpers consist of polypropylene (PP) blends with additives such as high-density polyethylene (HDPE) and ethylene propylene diene monomer (EPDM), as well as fillers including carbon black (for UV resistance) and talc(for structural reinforcement) (Mano et al., 2000, as cited in [7]). Additionally, the outer surface of the bumper is coated with a multi-layer automotive paint system, including a primer, surfacer, topcoat (basecoat, and clear coat) [7]. Table 1.1 provides an overview of the structure and function of these layers [8][9]. These layers collectively contribute to signal attenuation, phase shift, and distortion, which may degrade the accuracy of DoA estimation.

Table 1.1: Functions of Individual Layers in Automotive Bumper Coating System

Layer	Function
Clear Coat	Provides gloss and protects surface from UV and scratches
Basecoat	Adds color and determines visual appearance
Surfacer	Smooths surface and improves adhesion
Primer	Enhances bonding to substrate and prevents corrosion
Substrate	Structural base; typically a polymer in bumpers

The primary function of bumpers is to absorb and dissipate impact energy during low-speed collisions, optimizing passenger safety and minimizing damage to the vehicle body. Modern bumpers are frequently aesthetically incorporated into the vehicle's design. Bumpers also function as housings for embedded sensors, including radars, cameras, and ultrasonic devices, in addition to their mechanical protective function. But this configuration introduces significant performance degradation. As reported by Dash and Sarkar (2021) [10], key issues arise primarily from the electromagnetic interaction between radar signals and bumper materials. Dielectric losses in bumper materials lead to a bidirectional loss, effectively reducing the radar's detection range. Additionally, far-field pattern distortion results in angular ambiguities and elevated sidelobes in the angular ambiguity amplitude function, increasing the risk of false detections in DoA estimation.

Schwarz et al. (2024) conducted a comprehensive experimental study on the impact of bumper materials on low-, mid-, and high-resolution MIMO radar systems operating at 77 GHz[11]. Their results demonstrate that the dielectric properties of bumpers alter wave propagation, introducing phase shifts that are not fully compensated by calibration, especially in dynamic conditions such as mud or rain contamination.

Previous studies have analyzed the combined effects of rainwater and bumper structures on 76–81 GHz automotive radar at the electromagnetic level, including signal transmission and array gain patterns [12]. Using continuous water films and discrete droplets in electromagnetic simulations, these works provide a benchmark modeling approach, although the impact on DoA estimation was not assessed.

Moreover, the effect of multi-layered painting on bumpers has also been studied. A physical optics (PO)-based mathematical model was proposed to quantify both dielectric and mismatch losses through multi-layered bumper assemblies [13]. This model advances beyond existing radome analysis techniques by specifically addressing automotive design constraints where electromagnetic transparency often conflicts with aesthetic and aerodynamic requirements. These works provide valuable insights into rain-induced signal degradation and effects of painting layer on bumper but leaves the system-level impact on radar processing algorithm unexplored. Table 1.2 provides a summary of the experimental setups and major findings reported in relevant literature.

Table 1.2: Experimental Setup and Results from the literature

Freq. (GHz)	**Antenna Used**	**Model Overview**	**Measurement Setup**	**Major Results**
76–81[7]	Vertical polarization	Flat and curved bumper samples analyzed	Anechoic chamber; absorbers around samples; temperature controlled (21±1°C)	Attenuation smaller than 1.25 dB for flat samples; up to 33.5m detection loss; curvature increases variability
76–81[14]	Not specified	Painted polycarbonate samples characterized with material characterization kit	Optical free-space measurement setup	Basic attenuation measured; no detailed uncertainty given
77, 300, 670[15]	Linear polarization	Samples with three types of paint (details of shape and origin not specified)	Lab-based free-space setup; absorber on one wall	Standard deviation shown as error bars; no numerical uncertainty provided
76–81[16]	Not specified	Actual automotive bumper samples	Free-space method in lab; no absorbers used	No uncertainty provided; reduced measurement accuracy

1.4.2 DoA algorithms

Subspace-based methods have become a cornerstone in the field of direction-of-arrival (DoA) estimation due to their high resolution and robustness under certain ideal conditions. Among these, the most widely used algorithms are MUSIC (Multiple Signal Classification) and ESPRIT (Estimation of Signal Parameters via Rotational Invariance Techniques). Prior to ESPRIT, subspace-based methods such as MUSIC [17] dominated high-resolution parameter estimation but were computationally intensive due to spectral searches and sensitive to array calibration errors. MUSIC exploits the orthogonality between the noise and signal subspaces, and its asymptotic unbiasedness along with superior resolution over conventional beamforming established it as a gold standard. ESPRIT [18] further advanced the field by leveraging translational invariance in sensor arrays, eliminating the need for exhaustive spectral searches and precise array characterization. By exploiting the geometric symmetry of array doublets, ESPRIT derives closed-form parameter estimates via eigenvalue decomposition [19].

This section focuses on the effects of electromagnetic (EM) environments on three representative DoA estimation used in later study; these algorithms are BeamScan, MUSIC, and MVDR. BeamScan, or conventional beamforming, is a fundamental DoA estimation technique that determines the angle of arrival by scanning all possible directions and measuring the array output power. Its main advantages are simplicity, robustness, and low computational cost, making it a reliable baseline for assessing EM effects. However, its resolution is limited, particularly when multiple sources are closely spaced. MUSIC [17] is a high resolution subspace based algorithm that separates signal and noise subspaces via eigen-decomposition of the covariance matrix. By exploiting the orthogonality between the noise subspace and steering vectors, MUSIC can resolve sources that are much closer than those distinguishable by BeamScan, providing superior resolution and asymptotically unbiased estimates. Its performance, however, is sensitive to noise, snapshot number, and array calibration errors, which can be aggravated under non ideal EM conditions. MVDR (Minimum Variance Distortionless Response) is an adaptive beamforming technique that minimizes output power in all directions except the look direction, effectively suppressing interference while maintaining a distortionless response toward the desired source. MVDR typically achieves higher resolution and better interference rejection than BeamScan but is also sensitive to array imperfections and environmental perturbations, making it particularly relevant for studying EM effects. While other high-resolution algorithms exist, including ESPRIT [18], Matrix Pencil, and the Propagator Method [20, 21, 22, 23, 24], they require more precise array characterization or complex computations and are not considered in this study. Their mention here serves only to provide context, as the primary focus is on evaluating EM influences on the aforementioned representative DoA algorithms.

1.4.3 Gaps in the literature

While prior studies have extensively explored the performance of DoA estimation algorithms in MIMO radar systems under ideal propagation conditions, real-world automotive implementations often involve effects from the environment. Separately, a growing body of research has examined the electromagnetic impact of automotive bumpers, revealing that materials, coatings, and curvature can cause attenuation, multipath, or phase shifts in radar signals.

However, these two lines of research have yet to be fully integrated, and connections between them are still emerging. Current DoA estimation models often assume free-space or ideal propagation scenarios, overlooking the practical degradations introduced by bumper enclosures. As autonomous vehicles increasingly integrate radars behind non-metallic bumpers for aesthetic and aerodynamic reasons, this modeling gap becomes more critical.

Therefore, this study aims to address this gap partially by investigating the impact of bumper-induced signal distortions on DoA estimation accuracy in automotive MIMO radar systems. By combining electromagnetic simulation with algorithm-level performance evaluation, this research seeks to provide a more realistic understanding of radar performance in production vehicle environments.

1.5 Thesis scope and novelties

This thesis investigates the influence of car bumpers on radar signal transmission and system performance, specifically on DoA estimation within the 77 GHz frequency band. The study models the automotive radar antenna array using CST Microwave Studio to accurately simulate electromagnetic wave interactions at this high-frequency range. It thoroughly examines diverse bumper configurations, encompassing their shape, material composition, and distance to antenna array, and assesses the impact of these elements on antenna gain patterns. The research investigates the impact of environmental pollutants, precipitation (with different models) on the bumper surface, measuring their influence on radar signal degradation. The electromagnetic simulation results are subsequently included into DoA estimation methods with simplifications (same common pattern for all MIMO subarrays) to evaluate and potentially improve radar performance under realistic vehicular and environmental situations. This study employs a method that integrates electromagnetic simulation, materials characteristics, and signal processing to comprehensively analyze bumper-induced distortions in car radar systems.

This study integrates electromagnetic modeling results from CST into a traditional beamscan-based DoA estimation, as well as MUSIC and MVDR DoA estimation methodologies. A traditional beamforming method is utilised, wherein the spatial spectrum is calculated by sweeping the primary beam over the angular domain to determine the angle that optimises the received signal power. This method is chosen due to its provision of a direct and interpretable correlation between bumper-induced distortions in the antenna array response, such as gain attenuation, phase disturbances, and steering vector deformation and the consequent alterations in the beamscan spectrum. This work objectively evaluates the impact of various bumper configurations and environmental contaminants on angular resolution and Direction of Arrival accuracy by utilising CST derived distorted array patterns within the beamscan algorithm under realistic settings.

The novelty of this research lies in the integration of detailed electromagnetic bumper modeling into signal modeling and performance evaluation for DoA estimation algorithms. The modeling framework incorporates an antenna array and a multilayered bumper model, including geometry, material properties, paint layers, and realistic contamination effects, providing a more accurate approximation of real-world automotive conditions. It connects physical electromagnetic modeling with algorithmic performance by combining EM simulations with several DoA estimation algorithms, such as BeamScan, MUSIC, and MVDR. The research examines both single-angle DoA behavior, including array radiation pattern distortions and gain variations, and statistical performance across a large set of scenarios, providing a thorough evaluation of environmental contamination effects on radar signal propagation and algorithm robustness. This work represents a preliminary investigation as a more comprehensive electromagnetic modeling framework would require considering embedded element pattern variations, mutual coupling, and complex phase-dependent radiation characteristics. These analyses may support the design of robust perception systems for intelligent vehicles and advanced driver-assistance systems (ADAS).

1.6 Thesis structure

The research objective, problem formulation, and primary contributions are introduced in Chapter 1, which also provides an overview of the thesis's general structure. The creation of CST electromagnetic (EM) models for an antenna array, rainstorm impacts, automobile bumper structures, and the 77 GHz tapered 2Tx-4Rx MIMO subarray antenna is covered in Chapter 2. This chapter focuses on characterizing antenna performance under various structural and environmental conditions, including attenuation and radiation pattern distortion induced by the bumper and water accumulation. Important electromagnetic parameters, like S11 and realised gain patterns, are retrieved to facilitate the processing of radar signals and the assessment of algorithms.

Chapter 3 examines deterministic direction-of-arrival (DoA) estimate performance by integrating the EM-level antenna responses into FMCW MIMO radar simulations, building on the results of the EM modelling. The susceptibility of the Beamscan, MUSIC, and MVDR algorithms to amplitude loss and pattern distortion brought on by environmental obstructions is examined under representative high- and low-gain angles. The impact of realistic antenna degradations on deterministic DoA performance is discussed through comparisons with ideal uniform linear arrays.

In order to assess the resilience of the DoA estimate algorithms under consideration in stochastic environmental conditions, Chapter 4 expands the investigation to a statistical framework. The influence of various rainwater configurations and bumper-induced attenuation on algorithmic performance is quantified using metrics such as RMSE and MAE, highlighting trends in robustness and vulnerability across different scenarios. The main conclusions are also outlined in this chapter, along with the practical ramifications for designing automotive radar systems and future research directions, such as full system integration, adaptive algorithm compensation, and other surface contamination.

2 Electromagnetic and Environmental Modeling

2.1 Subarray Antenna Design

Initially, the antenna element model (Figure 2.1b) was constructed based on dimensions of 7-element series-fed 77GHz linear broad-side array antenna reported in [12] and [13]. The antenna was designed on a 0.25 mm thick RT5880LZ substrate with a relative permittivity (ϵ_r) of 2 and a loss tangent (tanδ_r) of 0.0021 [12, 13].

However, it was found that the simulated resonant frequency was slightly lower than the expected level as in Figure 2.2a. This discrepancy could be attributed to a variety of factors, such as simplifications in the original design geometry that were not expressly stated in the referenced works, differences in simulation settings or meshing resolution. The patch dimensions were then adjusted to get the desired resonance frequency at 77 GHz Figure 2.1a.

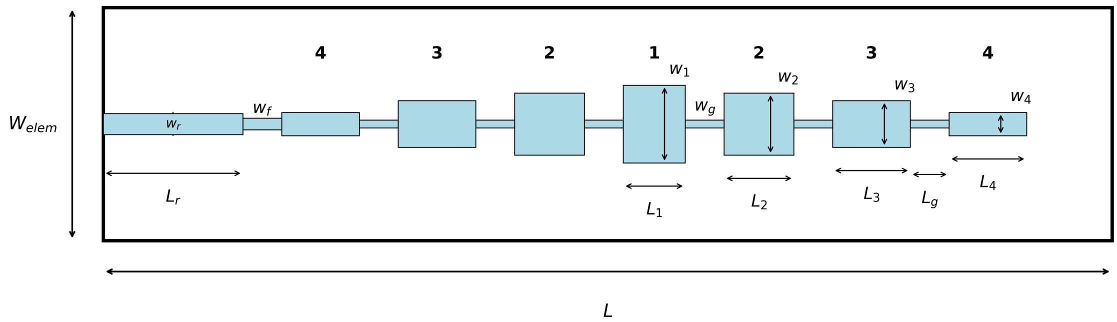

(a) Geometry and dimensions of the linear series-fed radar antenna subarray used in the MIMO radar. (Key dimensions are: $W = 5.6$mm, $L = 22.645$mm, $L_1 = L_2 = 1.31$mm, $L_3 = 1.315$mm, $L_4 = 1.325$mm, $W_1 = 1.58$mm, $W_2 = 1.18$mm, $W_3 = 0.553$mm, $W_4 = 0.158$mm, $L_g = 1.085$mm, $L_r = 3$mm, $W_r = 0.12$mm,$W_f = 0.1$mm, $W_g = 0.03$mm)

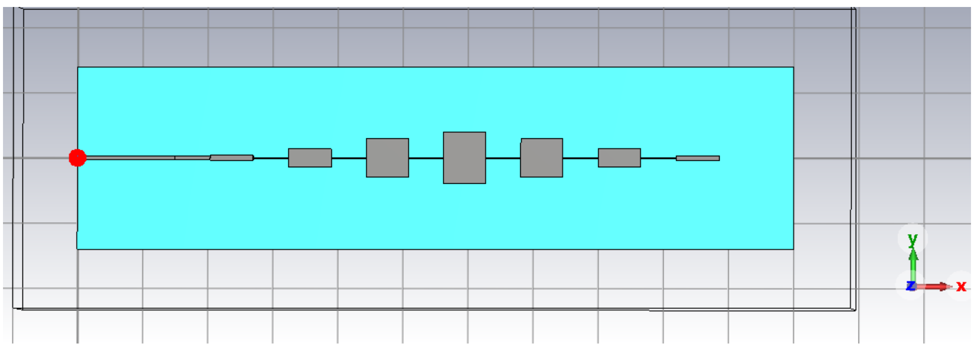

(b) 3D CST simulation model of the linear series-fed antenna subarray.

Figure 2.1: Linear series-fed radar antenna subarray.

After these adjustments-primarily by reducing the length of the patches-the simulation results exhibited a resonant frequency centered around 77 GHz, as shown in Figure 2.2b, thereby confirming the effectiveness of the modified geometry. It offers $S_{11} \leq -10dB$ over the operating bandwidth of 1.4 GHz.

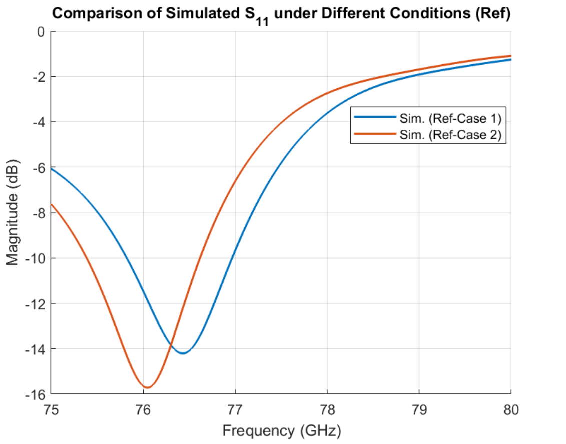

(a) Simulated S11 curves reproduced from reference studies. (Curves regenerated are based on Ref. Case 1 [13] and Ref. Case 2 [12], corresponding to two sets of sub-array parameters.)

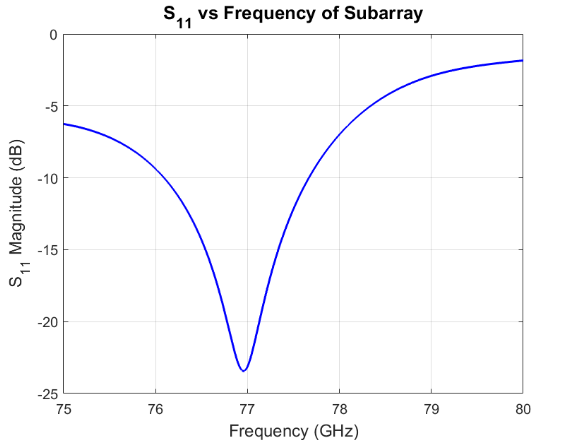

(b) Simulated S11 performance of the proposed sub-array design.

Figure 2.2: Simulated S11 performance comparison

In this design, the antenna element structure was extended into a 2-transmit and 4-receive MIMO radar system based on spacing parameter provided in [13]. A schematic of the 6-element MIMO radar antenna system, comprising 2 transmit and 4 receive channels, is shown in Figure 2.3. The module measures 22.645 mm × 19.3 mm and is designed on a 0.25 mm thick RTD5880LZ substrate ($\varepsilon_r = 2.0$, $\tan\delta = 0.0021$).

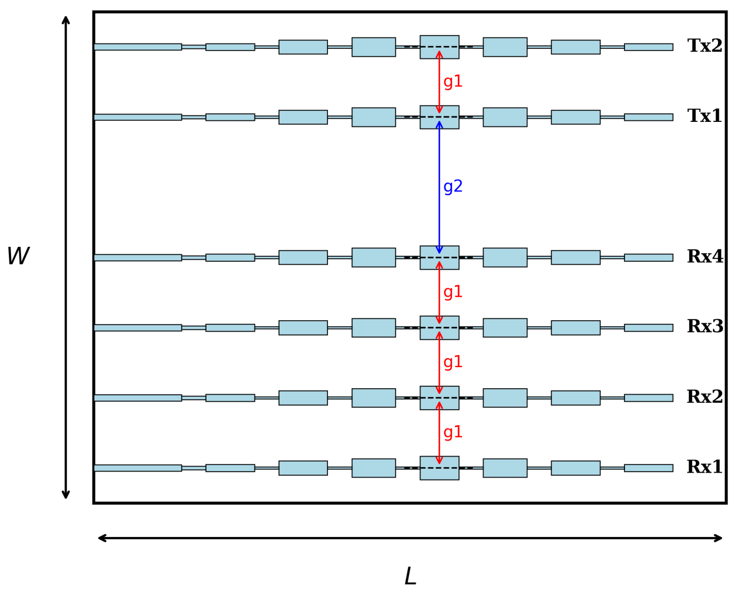

Figure 2.3: Schematic of the 6-element MIMO radar antenna with $g_1 = 1.94$ mm, $g_2 = 4.4$ mm, $W = 19.3$ mm, and $L = 22.654$ mm. The subarray dimensions are also adjusted to $L_1 = L_2 = 1.32$ mm and $L_3 = L_4 = 1.35$ mm.

Figures 2.4a and 2.4b show the input matching (S11) and the separation between antenna sub-arrays, but only the Tx1 antenna is excited in this case. Tx1, as the edge element of the Tx group, is used here to represent the behavior of the entire Tx and Rx groups. This simplification is justified because simulations were performed for all subarrays, and they have comparable realized gain in the main beam directions. Differences occur primarily at the angular ranges of -78° to -120° and 70° to 120°, mainly due to variations between the Tx and Rx groups. At the operating frequency and boresight direction, the realized gain is mostly determined by the horizontal polarization (H-pol) with maximum realized gain approximately 10 dB, whereas the cross-polarization (X-pol) component is effectively minimized ($\leq$ 0 dB). Therefore, the realized gain is predominantly influenced by the co-polarization component. The antenna shows effective impedance matching, with S_{11} values below –10 dB, and displays high isolation exceeding 19 dB over a bandwidth greater around 1.3 GHz. Figures 2.4c and 2.4d illustrate the 2D azimuth radiation pattern and the 3D far-field radiation pattern, respectively, with excitation applied to Tx1. Here, ϕ is defined as the angle from the x-axis to the y-axis, and θ as the angle from the z-axis to the x-axis. The $\phi = 90^\circ$ cut in both 2D and 3D figures corresponds to the y–z plane.

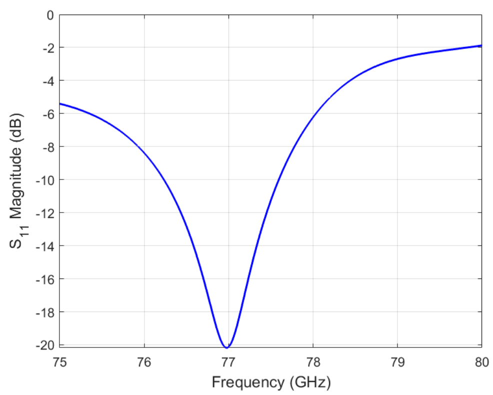

(a) S11 of Tx1 antenna

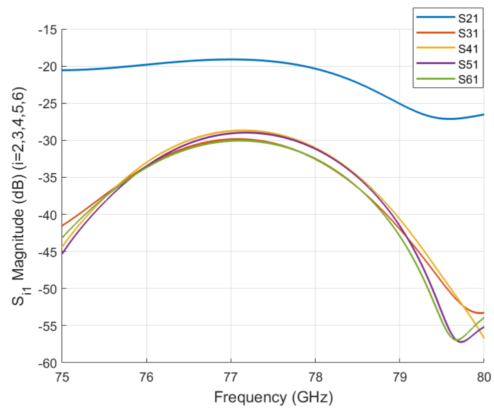

(b) Si1 ($i = 2$ to 5) of Tx1 antenna

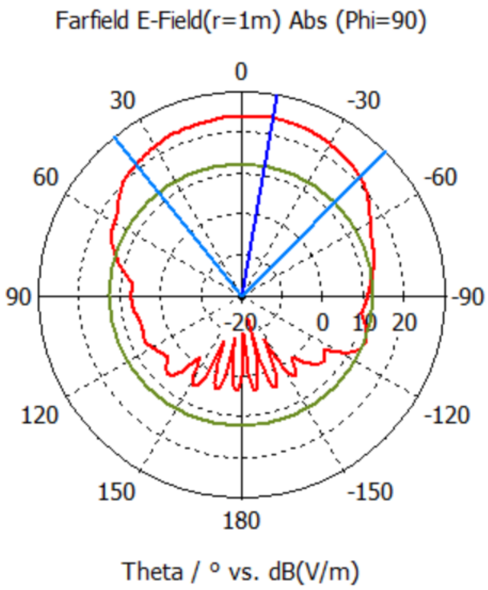

(c) Azimuth E-field pattern

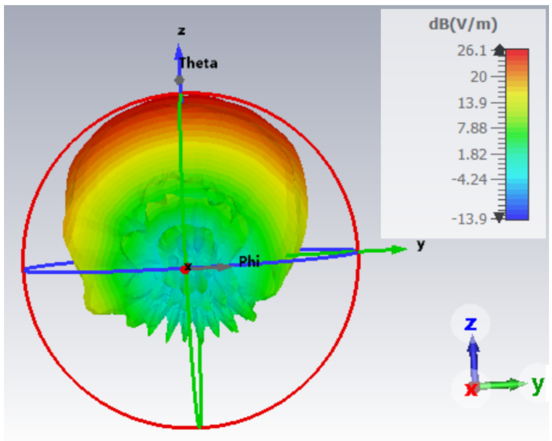

(d) 3D E-field pattern

Figure 2.4: Simulated electromagnetic characteristics of the Tx1 antenna in the presence of the other antennas.

2.2 Material Effects on Signal Transmission

To investigate the potential impact of environmental and structural surface layers on automotive radar signal behavior, a simplified multilayer dielectric model was developed as an initial approximation. The electromagnetic interactions between incident signals and the bumper system were rigorously examined using the Floquet modal method, enabling the isolation and preliminary analysis of the effects introduced by these layers. Floquet theory is well suited for periodic or quasi-periodic structures; this approach efficiently captures wave propagation phenomena, including reflection, transmission, and diffraction, within complex layered media exhibiting periodicity. This method drastically cuts down on simulation time and computing expense compared to expanding the research to more complicated scenarios. This unit-cell model offers a baseline validation framework to evaluate the accuracy and consistency of the multilayer electromagnetic modeling. When the water film thickness is varied, the resulting modifications in the simulated response are continuous and interpretable. Similarly, differences in droplet size and spacing result in physically consistent trends. It should be noted that this initial model focuses exclusively on the layered materials and does not incorporate the antenna structure itself.

To accurately assess the influence of surface coatings and environmental layers on radar performance, the bumper, paint, and water film were modeled as distinct dielectric layers, each characterized by its complex relative permittivity $\varepsilon_r = \varepsilon' - j\varepsilon''$. In this study, material properties are consistently described using the real part of the relative permittivity ε' and the loss tangent $\tan\delta = \frac{\varepsilon''}{\varepsilon'}$, providing a concise yet effective representation for electromagnetic simulation.

Automotive exterior components generally have wall thicknesses of 2.5 ± 0.25 mm, while larger elements, such as bumpers, are engineered with around 3 mm thickness to guarantee sufficient structural integrity, manufacturability, and surface quality, hence preventing flaws such as warping or sink marks [25]. A plastic bumper substrate ($\varepsilon_b = 2.76$, $\tan\delta_b = 0.012$) with a thickness of 3 mm and a paint layer 0.1 mm thick ($\varepsilon_p = 9$, $\tan\delta_p = 0.1$) was used to reflect typical polymer-based automotive materials and the painting layer [12].

The water film permittivity, however, exhibits strong frequency and temperature dependence. Due to the lack of exact data at 77 GHz (see Table 2.1), permittivity values measured at 80 GHz and 20°C ($\varepsilon_w = 8.84$, $\tan\delta_w = 1.716$) were used as an approximation [26]. Table 2.2 summarizes the electrical properties of the materials used in the simulation model.

Table 2.1: Permittivity of water near 77 GHz at different temperatures (data adapted from [26].)

Frequency (GHz)	**Temperature** (°C)	Real part ε'	Imaginary part ε''
70	10	7.97	13.59
70	20	9.78	17.11
70	30	11.26	20.04
80	20	8.84	15.17
80	30	9.87	18.23

Table 2.2: Electrical properties of materials used in simulation

Material	**Thickness [mm]**	ε_r	$\tan\delta$
Plastic bumper substrate	3.0	2.76	0.012
Paint layer	0.1	9.00	0.10
Water (80 GHz, 20°C)	–	8.84	1.716

In the Floquet simulation framework, the multilayer materials were modeled as homogeneous dielectric layers within a small periodic unit cell. This unit cell represents the fundamental repeating section of the bumper surface. Floquet boundary conditions were applied on the lateral boundaries to simulate an infinite periodic structure, enabling an initial, yet effective, analysis of electromagnetic wave interactions with the layered materials.

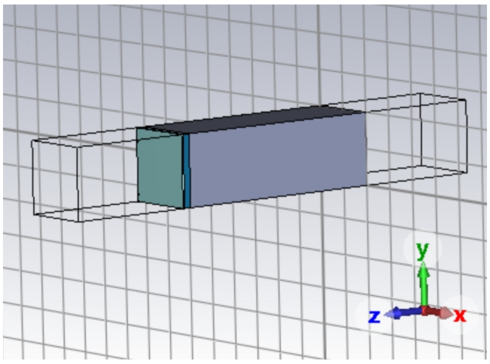

(a) Thin water film model illustrating the film thickness $h = 12$ μm.

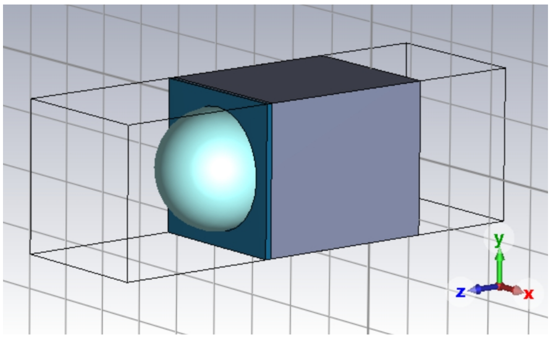

(b) Hemispherical water droplet model illustrating droplet diameter $d = 2$ mm, and size of the cell $s = 2.5$ mm.

Figure 2.5: Rainwater Model on Automotive Bumper

Environmental variations in water film thickness and the size of water droplets were also parameterized to study their effects on the transmission coefficients. In this study, the modeling of rainwater accumulation on the bumper surface follows the approach proposed in [12], where rainwater is represented by two different forms: a continuous thin water layer (see Figure 2.5a) and discrete hemispherical droplets (see Figure 2.5b). The thin film model assumes a uniform layer of varying thickness $h = 12$, 19, and 25 μm depending on the rain rate, while the droplet model uses hemispheres with diameter $d = 2$ mm in unit cells of size $s = 2.5$ and 3.0 mm, and $d = 3$ mm in unit cells of size $s = 3.5$ and 4.0 mm. A full overview of these configurations is provided later in Table 2.6 and Table 2.7. For simplicity, non-uniform water layers and non-uniform droplet distributions are not considered. This dual modeling approach enables a comprehensive analysis of the electromagnetic effects of rainwater on the automotive radar signal propagation through the bumper.

The simulation results reveal that the thin water film has a limited effect on the transmission coefficients, and variations in film thickness cause only modest differences. In contrast, discrete water droplets induce a significant impact, with droplet size and unit cell dimensions strongly influencing the results. These findings demonstrate the validity of the simulation framework in capturing the influence of environmental water on radar signal propagation. Moreover, they suggest that droplet accumulation on bumper may have a stronger impact on antenna performance than uniform water layers.

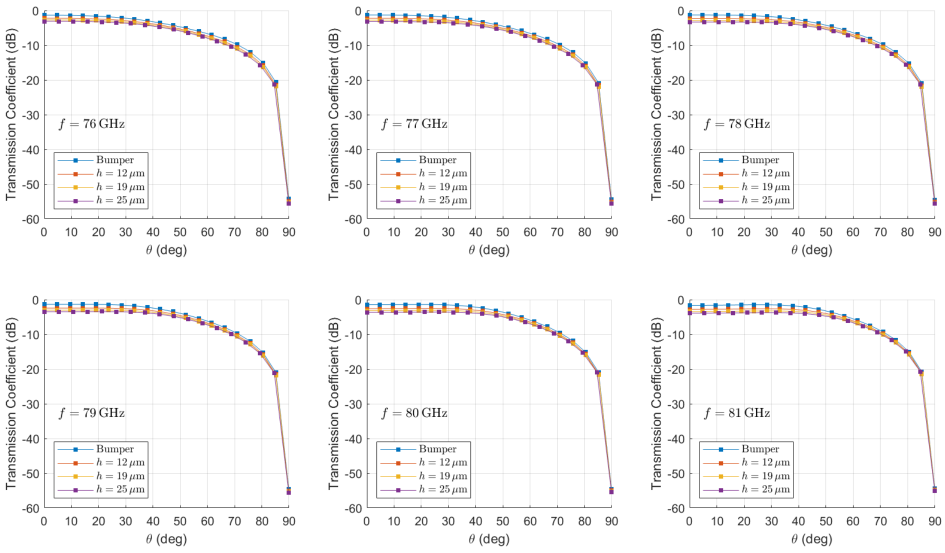

Figure 2.6: Effect of water film on transmission coefficient at 76-81 GHz.

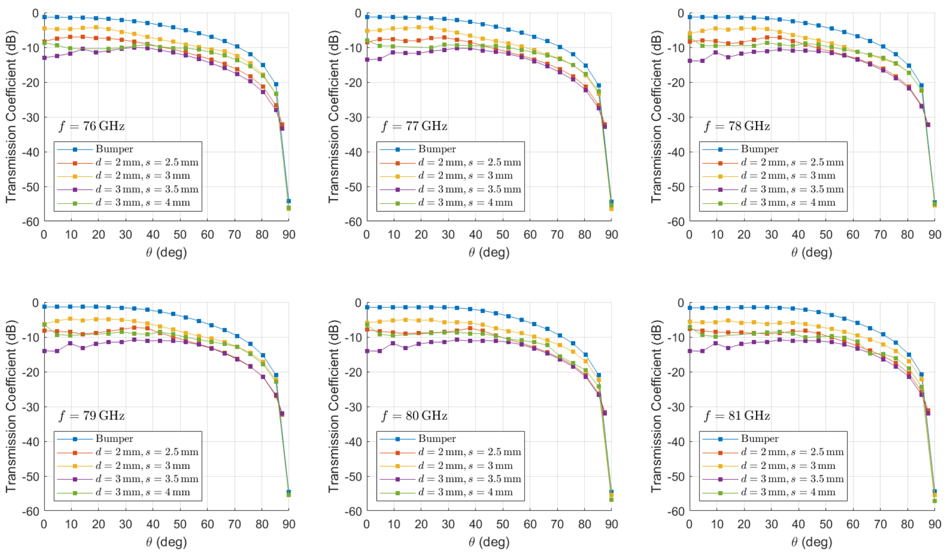

Figure 2.7: Effect of water droplets on transmission coefficient at 76-81 GHz.

2.3 Bumper Model

2.3.1 Bumper Structure Modeling

To investigate the impact of bumper geometry on antenna performance, we consider two straightforward bumper models: flat and curved bumper model as shown in Figure 2.8.

Flat Bumper Model

This model consists of a simple rectangular plate positioned in front of the antenna with distance of 20 mm (as reported in [12]), serving as a reference to isolate geometric effects

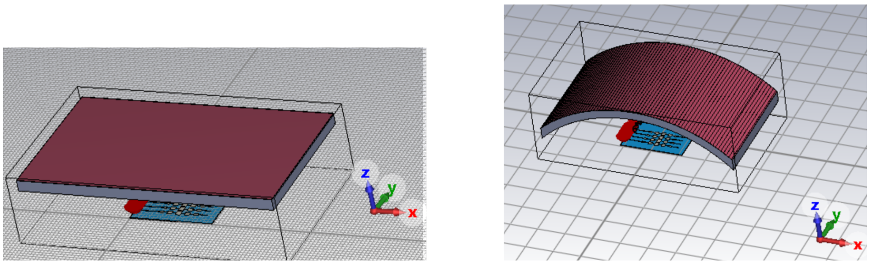

(a) Flat Bumper Model (b) Curved Bumper Model

Figure 2.8: Comparison of flat and curved bumper geometries used in electromagnetic simulation.

without curvature. The bumper sizes used in the simulation are listed in Table 2.3, with the reference bumper size (70 × 40 mm) taken from [12]. Figure 2.9 shows (a) the reflection coefficient (S_{11}) for each bumper model, (b) the far-field realized gain in the $\phi = 0°$ plane, and (c) the far-field realized gain in the $\phi = 90°$ plane. The subsequent analysis of the array performance, including its response under different exterior influences and potential blockages, is presented using this set of plots. In particular, the $\phi = 90°$ realized gain is of special interest, as it corresponds to the plane used for subsequent DoA scanning and angle-of-arrival calculations. Figure 2.9 shows that the presence of the bumper introduces some distortion, while variations in bumper size within this range have little effect on the attenuation of the realized gain pattern. Notably, significant attenuation is observed around 30° and −50° in $\phi = 90°$ plane. Moreover, the simulation time remains of the same order of magnitude for all sizes. Therefore, in the following analysis, we adopt the 70 mm × 40mm bumper as the reference size. This choice allows sufficient space to incorporate the rainwater model in subsequent simulations while keeping the computational cost manageable.

Table 2.3: Bumper Sizes Used in Simulation (Width × Height in mm).

Case	1	2	3	4
Bumper Size (Length × Width)	70 × 40	60 × 40	50 × 40	40 × 40

Curved Bumper Model

The curved bumper is modeled as a segment of a circular cylindrical shell with varying radii and a fixed vertical height of 40 mm. An example of a curved bumper is shown in Figure 2.8b. For reference, the baseline flat bumper measures 70 mm × 40 mm. To ensure consistency across all simulations, each curved bumper is positioned 20 mm away from the antenna array. All bumper models are constrained within a spatial envelope of 70 mm × 40 mm × 20 mm.

Table 2.4: Curvature Radii of Bumper Models

Radius (mm)	60	55	50	45	40

The curved bumper is modeled as a segment of a circular cylindrical shell with varying radii (see Table 2.4) and a fixed vertical height of 40 mm. An example of a curved bumper is shown in Figure 2.8b. For reference, the baseline flat bumper measures 70 mm × 40 mm. To ensure consistency across all simulations, each curved bumper is positioned 20 mm away from the antenna array. All bumper models are constrained within a spatial envelope of 70 mm × 40 mm × 20 mm.

The impact of these different bumper geometries on antenna performance is evaluated in terms of impedance matching (S11) and far-field radiation patterns as in Figure 2.10. The changes in S11 are a little irregular, with the resonant frequency generally shifting upward by

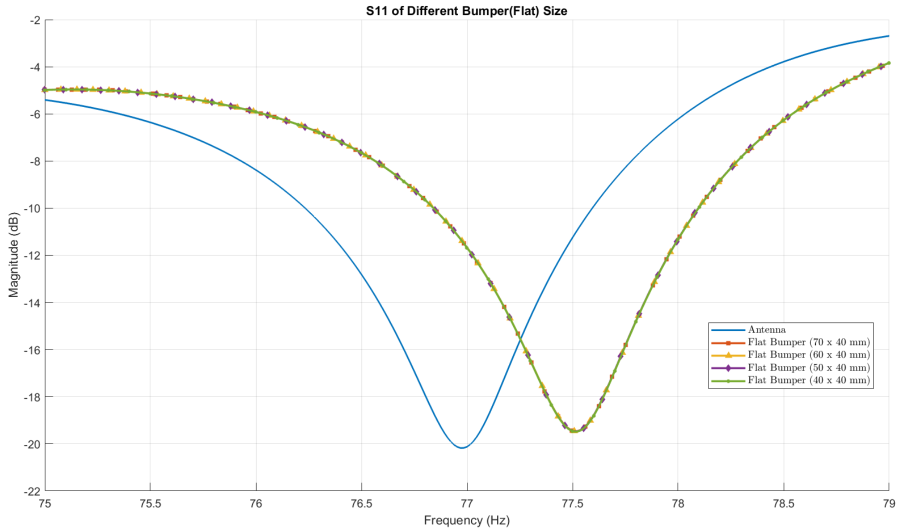

(a) Effect of Bumper Size on antenna parameters S11

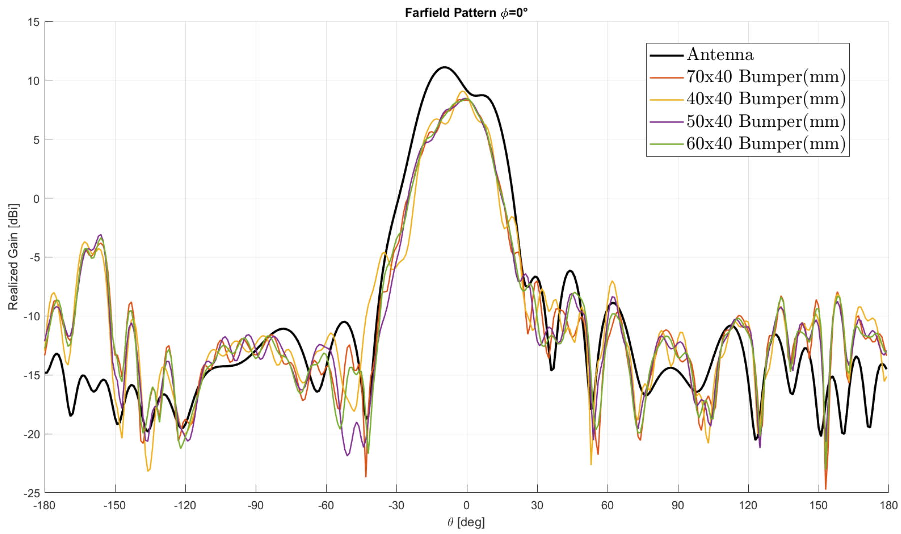

(b) $\phi = 0$ deg realized gain

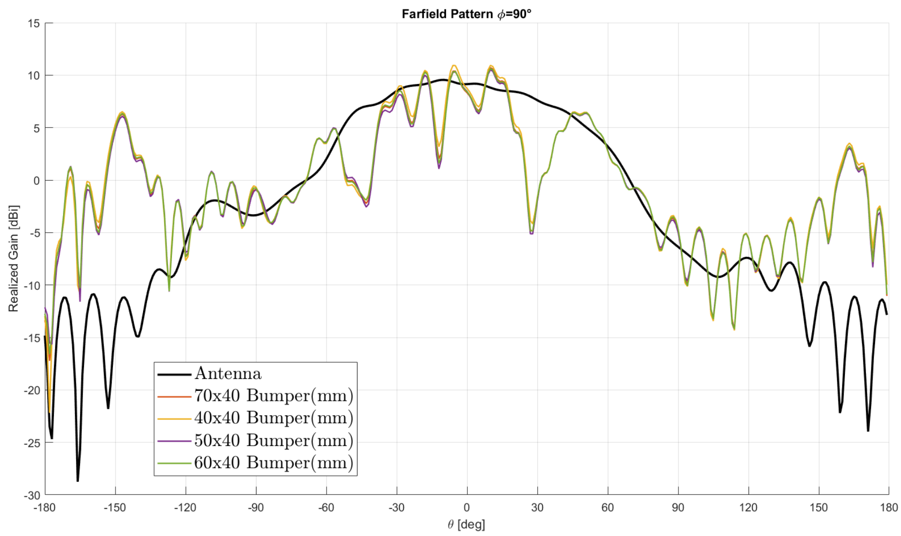

(c) $\phi = 90$ deg realized gain

Figure 2.9: Effect of flat bumper size variations on antenna subarray performance in terms of S11 and far-field realized gain.

approximately 0.5 GHz. Overall, the degree of bumper curvature has a similar effect on the realized gain, although the influence is slightly less consistent compared to that of bumper size. For each bumper configuration, the variation in realized gain trends is typically within 2 dB. Larger differences, up to around 5 dB, occur mainly near $\phi = 90^\circ$ and $\theta = 0^\circ$, but such extreme variations are limited to only a few angular points.

2.3.2 Impact of Bumper-to-Antenna Distance

The baseline size of the bumper model for this investigation is 70 mm × 40 mm. The distance between the bumper and the antenna was varied from 20 mm down to 5 mm, including intermediate values such as 17.5 mm, 15 mm, 12.5 mm, 10 mm, and 7.5 mm, to simulate various installation scenarios and manufacturing tolerances.

Table 2.5: Bumper-to-Antenna Distances Used in Simulation

Case	1	2	3	4	5	6
Distance (mm)	20	17.5	15	12.5	10	7.5

The presence of the bumper leads to an overall upward shift of the resonance frequency by approximately 0.5 GHz as shown in Figure 2.11a. Nevertheless, the antenna shows the best impedance matching at distances of 7.5 mm and 15 mm, where S11 reaches approximately -25 dB. This suggests that at these distances, the influence of the bumper may be minimized or even slightly beneficial due to near-field interactions. However, the distance has a significant impact on the realized gain at $\phi = 90^\circ$, with some configurations causing severe attenuation of up to around 10 dB, posing a serious threat to normal antenna operation. In certain cases (especially with the case when bumper is 17.5 mm away), even without considering environmental factors, inappropriate bumper distances can already substantially degrade antenna performance. In contrast, distances of 15 mm and 20 mm generally result in less extreme attenuation within the forward scanning range. Therefore, in the following analysis, we maintain a bumper distance of 20 mm.

2.4 Rainwater Modeling on Bumper Surface

The antenna is positioned 20 mm behind a bumper surface measuring 70 mm × 40 mm. To investigate the impact of surface water on antenna performance, two representative rainwater configurations are considered. Figure 2.12 illustrates these models: (a) a continuous thin water layer uniformly covering the bumper surface, and (b) discrete water droplets distributed over the bumper. These configurations are based on the surface water accumulation methods reported in [12] and are intended to represent varying levels and spatial distributions of rainwater, enabling assessment of their effects on electromagnetic wave propagation and antenna impedance characteristics.

2.4.1 Thin Film Layer Model

A continuous water film is represented by a homogeneous, paint-like layer covering the bumper surface. Different rainfall conditions are emulated by varying the film thickness. Table 2.6 summarizes the thickness levels considered in this study.

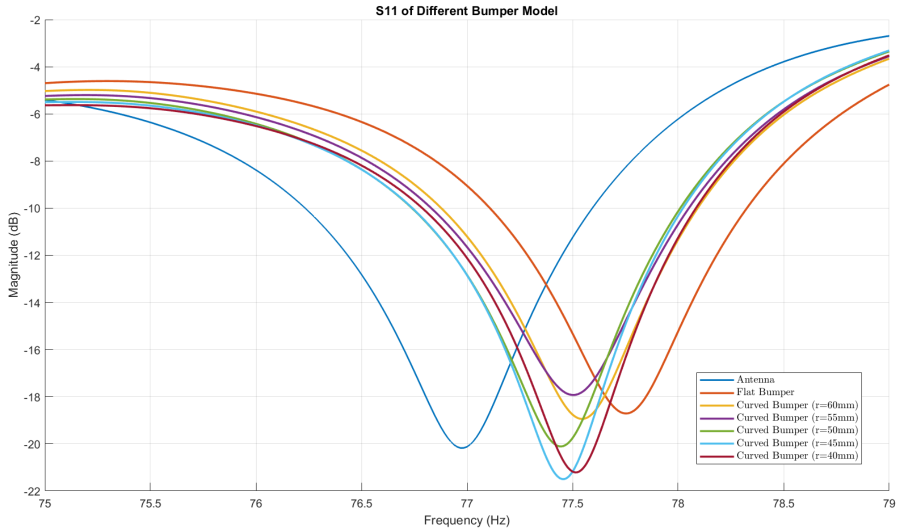

(a) Effect of Bumper Shape on antenna parameters S11

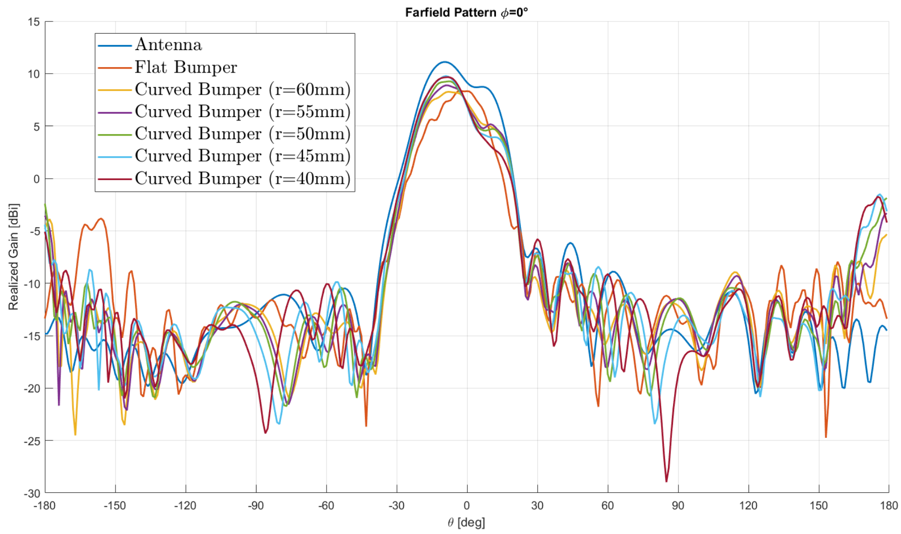

(b) $\phi = 0$ deg realized gain

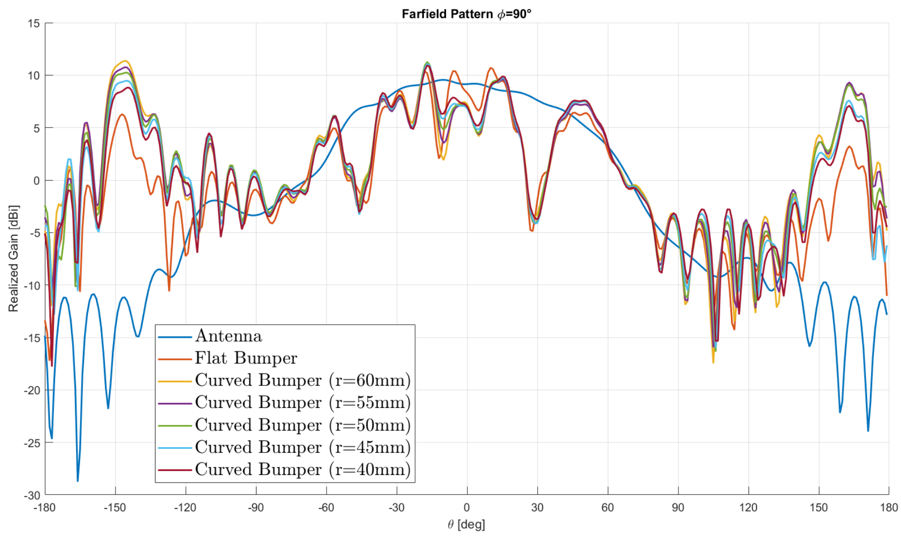

(c) $\phi = 90$ deg realized gain

Figure 2.10: Effect of bumper curvature on antenna subarray performance in terms of S11 and far-field realized gain.

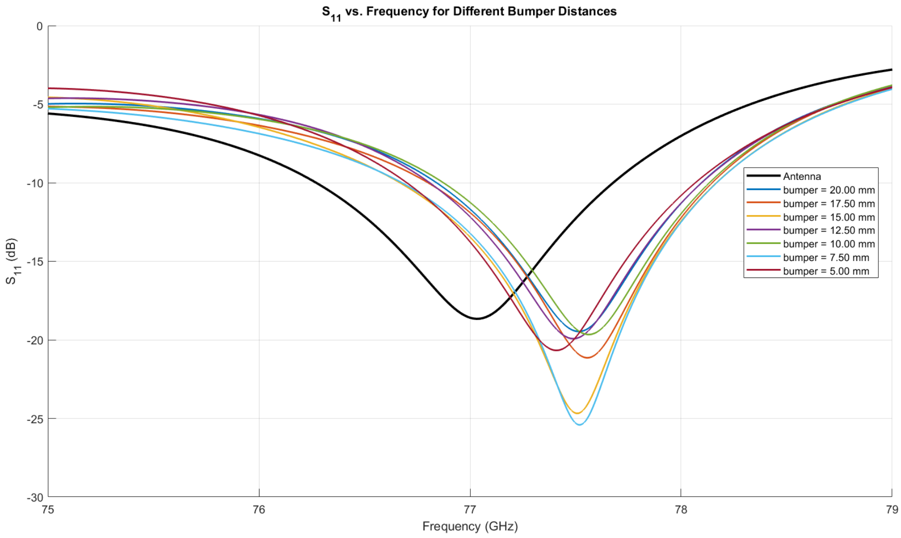

(a) Effect of Bumper-to-Antenna Distance on S11

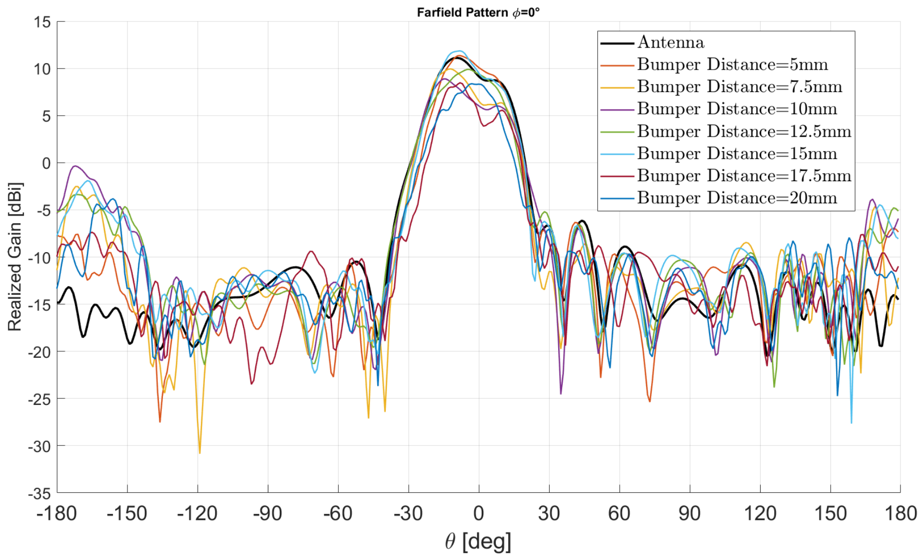

(b) $\phi = 0$ deg realized gain

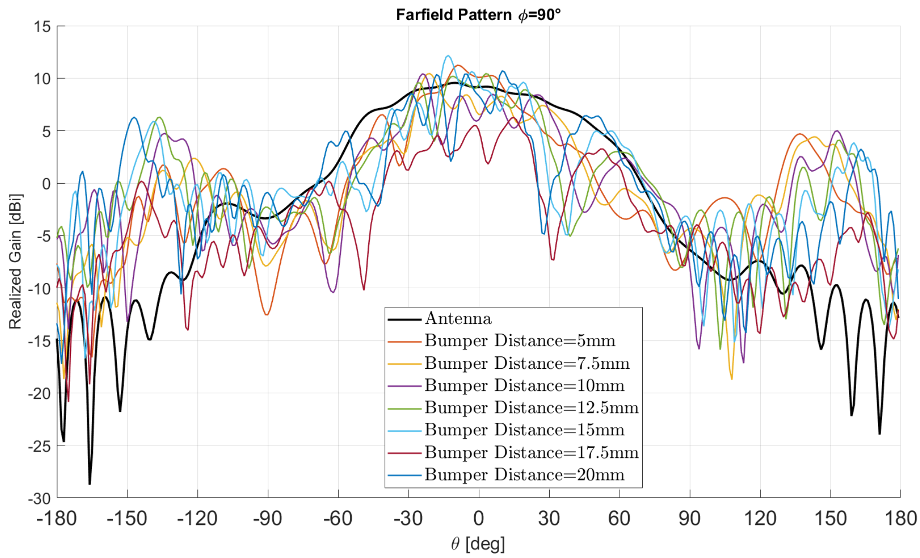

(c) $\phi = 90$ deg realized gain

Figure 2.11: Effect of varying bumper-to-antenna distances on antenna subarray performance in terms of S11 and far-field realized gain.

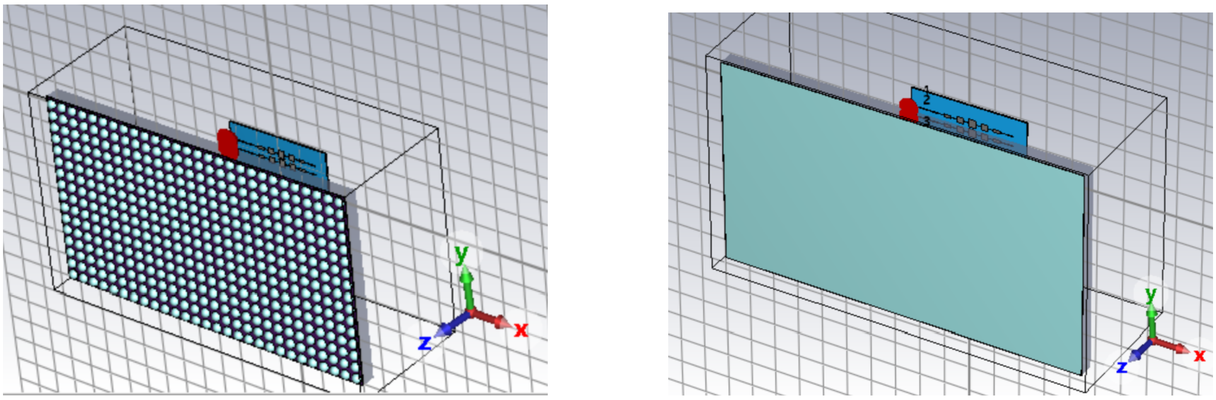

(a) Water Droplets Model

(b) Water Layer Model

Figure 2.12: Water droplets and thin layer over bumper geometries used in electromagnetic simulation.

Table 2.6: Water film thickness under different rainfall rates.

Rain rate RR (mm h^{-1})	10	40	80
Film thickness h (μm)	12	19	25

Here, h denotes the film thickness and RR represents the rainfall rate. Values reproduced from [12].

The presence of a uniform thin water layer on the curved bumper surface was found to influence the radar response as in Figure 2.13. Specifically, the thin layer increased the resonance frequency by approximately 0.8 GHz. Additionally, it caused an amplification of the far-field radiation pattern, particularly in the $\phi = 90°$plane around $\theta = \pm 180°$, indicating enhanced scattering in the lateral directions. These results suggest that even a relatively thin film of water can alter the electromagnetic characteristics of the bumper, which should be taken into account in robust radar system design. As shown in Figure 2.13, the legend entries represent a set of configurations of the proposed antenna for comparison:

- "Antenna": the standalone antenna without any bumper or rainwater layer.
- "Bumper": the antenna with the bumper mounted 20 mm in front of it, as previously described in Section 2.4, including a painting layer seamlessly applied on top of the bumper material. Hereafter, this configuration is referred to as the *bumper* configuration.
- "$h = 12, 19,$ and $25\ \mu$m ": the antenna with a rainwater layer of varying thicknesses (12, 19, and 25 μm) deposited directly on the front surface of the bumper (no air gap). For brevity, the described setup is hereafter referred to as the *water-layer* configuration.

The addition of the bumper shifts the antenna's resonant frequency upward by approximately $\Delta f = 0.8$ GHz compared to the standalone antenna. When a rainwater layer of varying thicknesses ($h = 12, 19,$ and $25\ \mu$m) is deposited on the bumper surface, the resonant frequency experiences a slight additional shift. However, this overall change does not significantly affect the antenna's operating frequency and bandwidth, indicating that the antenna performance remains largely robust under these conditions.

While the $\phi = 0°$ plane captures the impact on boresight far-field radiation, the DoA estimation requires observation along a plane corresponding to the target incidence direction. For this purpose, the primary observation plane is chosen at $\phi = 90°$. Scanning in this plane allows effective measurement of the angular characteristics of the incoming wave, providing accurate data for DoA analysis. All DoA results presented in this work are based on measurements taken in this $\phi = 90°$ plane. From the realized gain patterns in Figure 2.13c, it can be

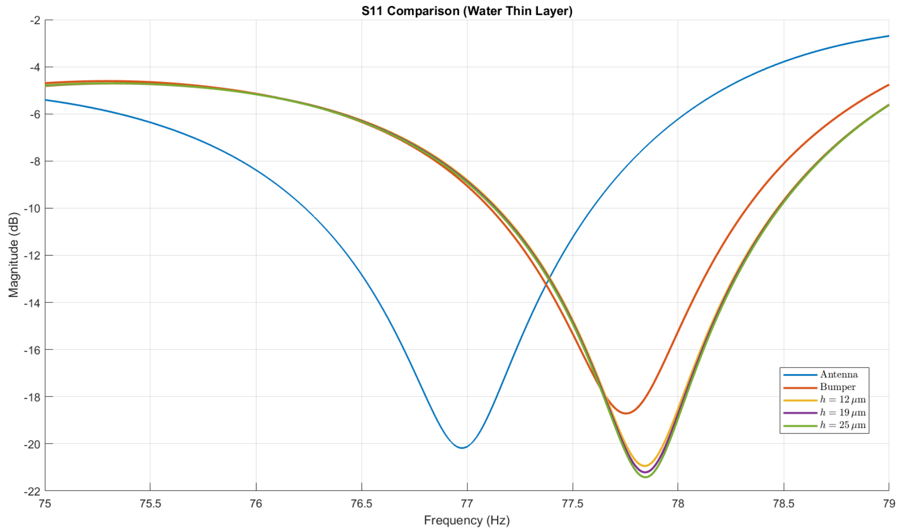

(a) Effect of continuous thin layer of rainwater on antenna parameters S11

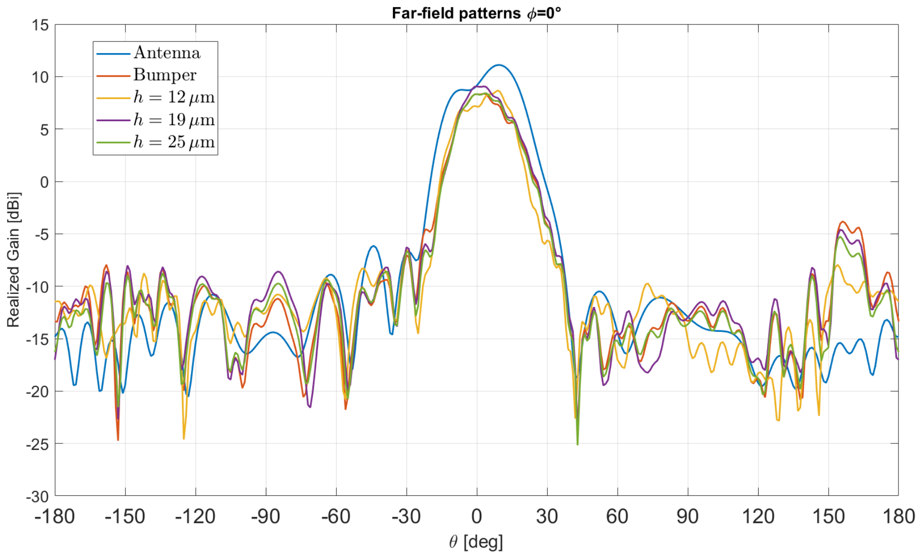

(b) $\phi = 0$ degrealized gain

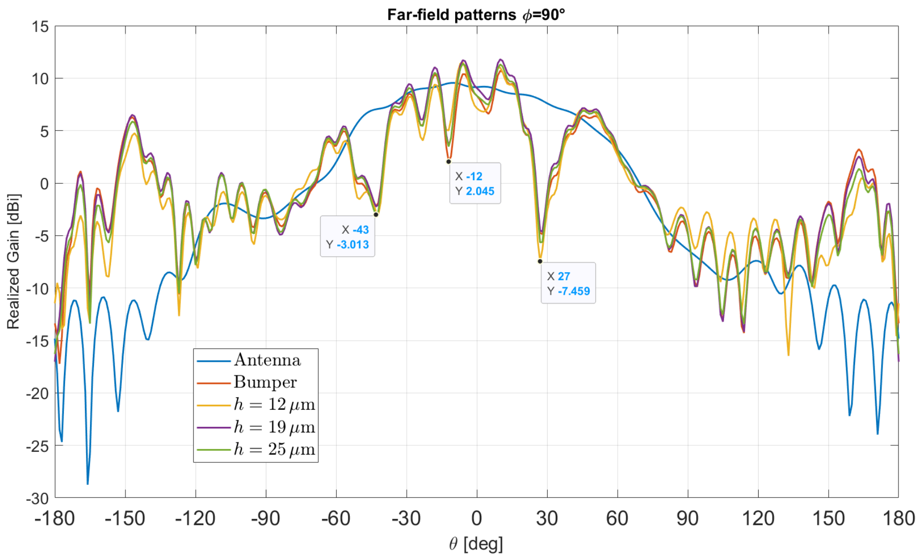

(c) $\phi = 90$ deg realized gain

Figure 2.13: Effect of thin water layers on antenna subarray performance in terms of S11 and far-field realized gain.

observed that the overall realized gain patterns of the bumper-only and bumper-with-water-layer configurations are highly consistent. The maximum variation between configurations is approximately 3 dB; however, such differences are rarely observed in the main radiation directions, where the variation typically remains within 1 dB. Despite this overall consistency, several localized deep attenuation notches are present, notably at 27° (−7.5 dB), −43° (−3.0 dB), and −12° (−2.0 dB).

2.4.2 Discrete Droplet Models

Water droplets are represented as hemispherical particles randomly distributed over the bumper surface to mimic localized water accumulation. Four representative configurations, differing in droplet size and unit cell dimensions, are summarized in Table 2.7.

Table 2.7: Simulation parameters for the four droplet configurations

	Case 1	Case 2	Case 3	Case 4
Droplet diameter d (mm)	2	2	3	3
Spacing (mm)	0.5	1	0.5	1
Unit cell size s (mm × mm)	2.5 × 2.5	3 × 3	3.5 × 3.5	4 × 4

Here, d denotes the droplet diameter and s represents the spacing between adjacent droplets.Parameter settings are adapted from [12].

As shown in Figure 2.14, the legend entries represent a set of configurations of the proposed antenna for comparison:

- “Antenna”: the standalone antenna without any bumper or rainwater layer.
- “Bumper”: the antenna with the bumper mounted 20 mm in front of it, as previously described in Section 2.4, including a painting layer seamlessly applied on top of the bumper material.
- “$d = 2$ mm, $s = 2.5$ mm” (and similarly for other d and s values): the antenna with a rainwater layer deposited on the bumper surface. Here, d denotes the droplet diameter and s represents the spacing between adjacent droplets as listed in Table 2.7. For brevity, this configuration is hereafter referred to as the *water-droplet* configuration. In the following sections, when ”case ”,”case 2”, ”case 3”, or ”case 4” is mentioned (or ”water droplet 1-4”), they correspond directly to the specific droplet parameters defined in Table 2.7.

Compared to the thin rainwater layers, rainwater droplets caused a more significant shift in the antenna response, increasing the resonant frequency by up to 1.2 GHz. Additionally, they led to stronger far-field suppression-up to a maximum of 10 dB reduction in the $\phi = 0°$ plane-highlighting their greater impact on electromagnetic performance under wet conditions (see Figure 2.14). Under the influence of water droplets, as shown in Figure 2.14c, several local minima are observed in the main radiation direction. The identified minima include Case 2 at −42° (−9.1 dB), Case 3 at −24° (−15.4 dB) and 1° (−13.7 dB), and Case 1 at 25° (−16.5 dB). Among these, the notches at −24° and 1° for Case 3 are notably deeper compared to the other configurations, whereas the minima at −42° and 25° exhibit substantial attenuation across all configurations.

These findings indicate that under wet weather conditions with non-uniform water deposition, the radar system may suffer more severe performance degradation compared to thin-film coverage, underscoring the need for weather-resilient radar enclosure design. The transmission performance is significantly lower for the droplet model compared to the continuous thin layer due to increased scattering and interference caused by discrete droplets. Larger droplets result in the worst transmission, acting like tiny lenses that scatter radar waves more strongly. For smaller droplets, larger spacing between them improves transmission, as electromagnetic waves can pass between droplets, whereas closely spaced droplets block the signal more effectively.

While the preceding analyses have highlighted how various structural factors, such as bumper geometry and mounting distance affected antenna performance, these are inherent design related influences. In contrast, rainwater represents an environmental factor that can change dynamically and unpredictably during operation. Motivated by this distinction, the following work focuses on modeling the impact of rainwater on the antenna and incorporating these effects into algorithm development for robust performance under adverse weather conditions.

2.5 Higher Resolution Antenna Model

In the initial setup, the antenna geometry was designed based on the dimensions reported in [12], in order to ensure consistency with prior studies. However, for the present work, the array configuration was modified by adopting a more common MIMO sub-array spacing. This adjustment serves two purposes: (i) it aligns the design with widely used MIMO radar architectures, and (ii) it increases the number of virtual antenna elements. The distance between the two transmitter sub-arrays was increased to four times the original spacing, $1.94\text{mm} \times 4 = 7.76\text{mm}$ (approximately two wavelengths). All other design parameters were preserved; only the transmitter sub-array spacing was modified, with the substrate and ground plane correspondingly extended to accommodate the enlarged array dimension. As a result, the number of available virtual antenna elements increases from 5 in the original design to 8 in the modified configuration. After the modification, the substrate dimensions (vertical × horizontal) changed from 19.4 mm × 22.645 mm to 25.12 mm × 22.645 mm.

The following graphs, Figures 2.16 and 2.17, present the far-field radiation patterns and reflection coefficients of the modified antenna, comparing the effects of the water-layer and water-droplet configurations on antenna performance. The rain water is still modeled as progressively thicker uniform water layers or four cases of water droplets applied to the bumper surface, based on same parameters used previously as in Table 2.6 and 2.7. And the legend corresponds to the legend system mentioned in section 2.4.1 and 2.4.2.In the following analysis, unless otherwise stated, all results refer to the modified antenna configuration shown in Figure 2.15b.

From these results, it can be observed that the modified antenna exhibits reduced sensitivity to rainwater droplets compared with the original setting, indicating improved robustness under adverse weather conditions. To further investigate, the realized gain is analyzed at specific angles for both water-layer and water-droplet configurations.

Under the water-layer conditions, the bumper and all water-affected configurations exhibited notably uniform performance. The largest difference in antenna gain across configurations was approximately only 1.6 dB at 23°, occurring between the baseline bumper-obstructed array setup without water layer (−2.3 dB) and the heaviest water-layer configuration (−3.9 dB). In Figure 2.16c, the realized gain shows clear notches at approximately −50° (−5.6 dB), −30° (2.6 dB), and 23° (−3.9 dB), which correspond to local minima collectively observed across all scenarios, rather than in any individual case, reflecting the consistent shape of the radiation patterns.

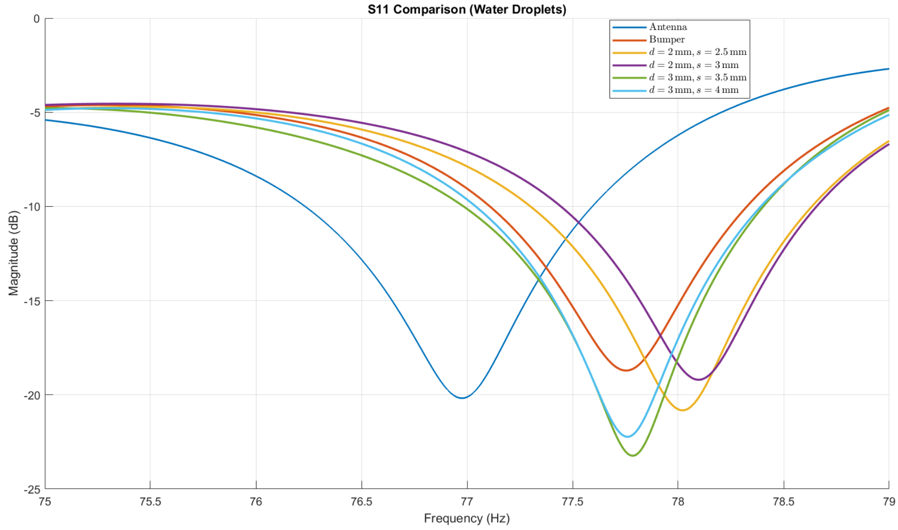

(a) Effect of droplets of rainwater on antenna parameters S11

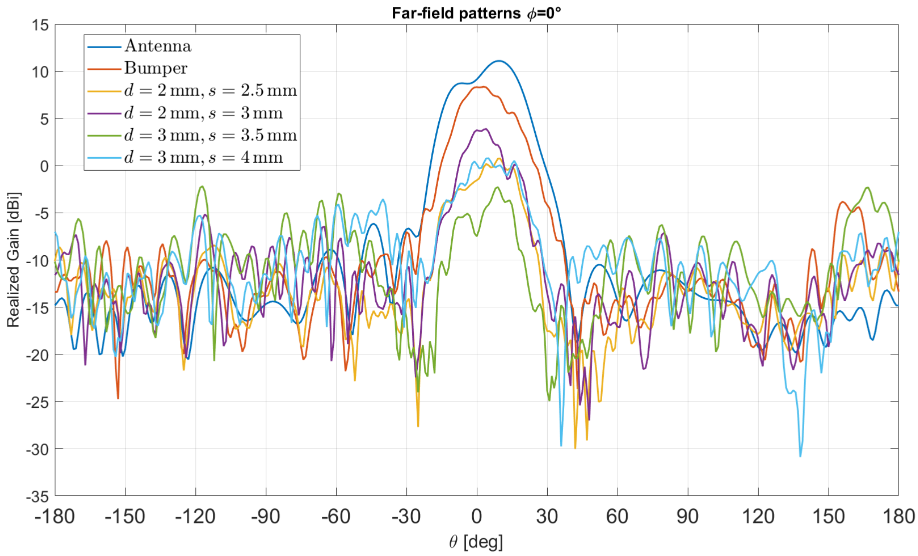

(b) $\phi = 0$ deg realized gain

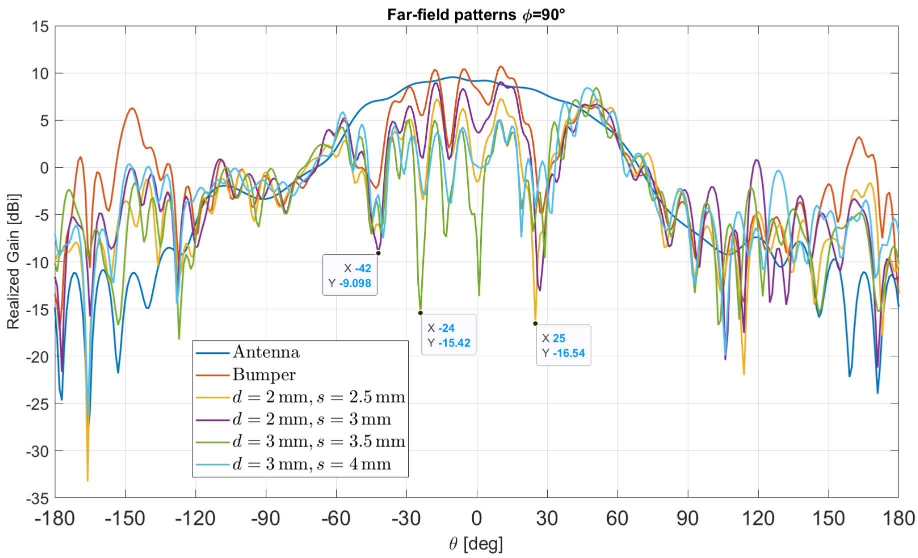

(c) $\phi = 90$ deg realized gain

Figure 2.14: Effect of water-droplet configurations on the bumper on antenna subarray performance in terms of S11 and far-field realized gain.

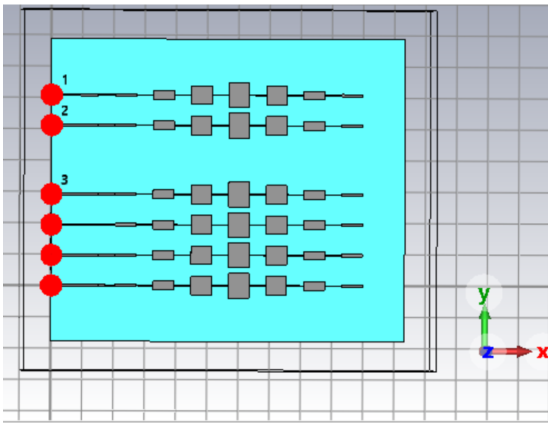

(a) Original antenna array configuration following the design in [12].

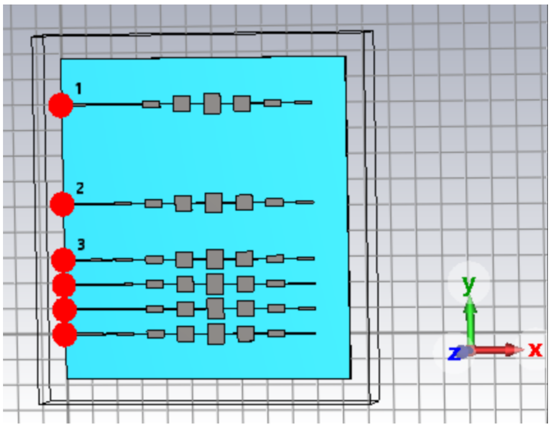

(b) Modified antenna array configuration adopted in further work.

Figure 2.15: Comparison of dense and sparse antenna array geometries.

In contrast to the relatively uniform attenuation observed under the water-layer conditions, the presence of water droplets introduces more localized and pronounced reductions in the realized gain. Here, Case 1, Case 2, and so on correspond to the water droplet configurations summarized in Table 2.7, as described in the experimental setup section. Across all water-droplet configurations, significant attenuation occurs in both positive and negative angular regions, with local minima forming notches in the radiation pattern in Figure 2.17c. For example, in the range 18°-26°, realized gain decreases below 0 dB, with the most pronounced attenuation observed near 22°. Within this range, the first water droplet case (Case 1) shows the most pronounced attenuation at 22° (−13.4 dB), followed by Case 2 reaches its minimum at 22° (−3.8 dB); the bumper-only obstructed case has its minima at 24° (−2.7 dB), and Case 3 at 24° (−7.3 dB), while Case 4 reaches its minimum at 26° (−7.1 dB).

Similarly, at negative angles, Case 3 exhibits several relatively narrow but deep notches at −4° (−11.3 dB), −18° (−3.0 dB), and −30° (−5.9 dB), whereas the other configurations show less pronounced attenuation at these angles. In contrast, a broader region of attenuation is observed around −47°, where Case 2 reaches the lowest realized gain of −7.8 dB. Within this wider notch region, nearby local minima are also observed for Case 3 at −51° (−6.4 dB) and for Case 1 at −49° (−6.1 dB). The detailed observations of these angular attenuation patterns provide a basis for subsequent algorithm testing and target detection studies under rainwater conditions.

2.6 Conclusion

In this chapter, electromagnetic models of a 77 GHz tapered 2Tx-4Rx MIMO subarray antenna, automotive bumper structures, and rainfall effects were first developed in CST to facilitate subsequent radar signal processing and algorithm evaluation. Based on established antenna design parameters, the subarray configuration was tuned to operate at the designated frequency of 77 GHz. To minimize simulation complexity, the edge transmit (Tx) subarray was chosen as a representative element, and its realized gain pattern was extracted and analyzed as a simplified depiction of the antenna's behavior.

Building upon the established antenna model, the material effects on signal transmission were investigated by positioning a bumper in front of the antenna array and systematically varying its properties. The bumper structure was modeled with different geometrical and positional parameters, including bumper size, curvature, and bumper-to-antenna distance, enabling a

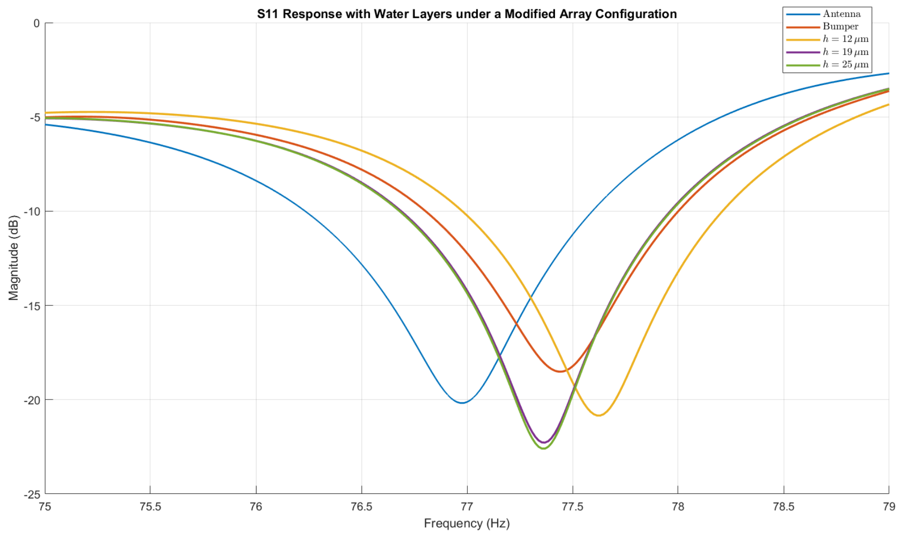

(a) Impact of water layers and bumper on the antenna performance: reflection coefficient (S11)

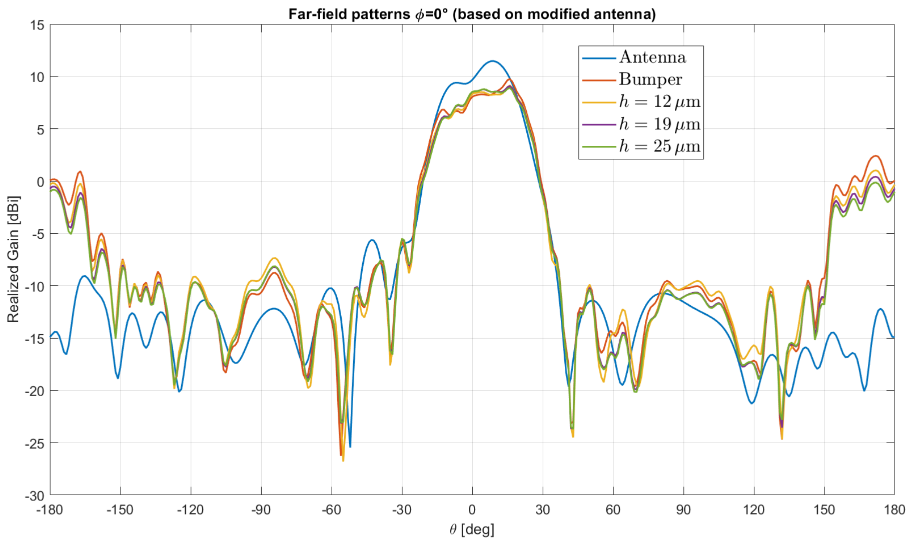

(b) $\phi = 0$ degrealized gain

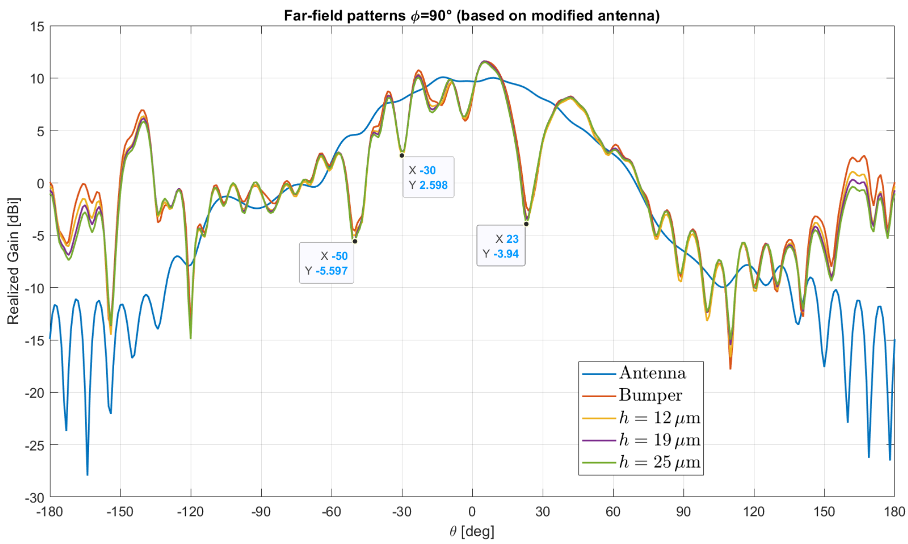

(c) $\phi = 90$ deg realized gain

Figure 2.16: Effect of thin water layers on higher resolution antenna subarray performance in terms of S11 and far-field realized gain

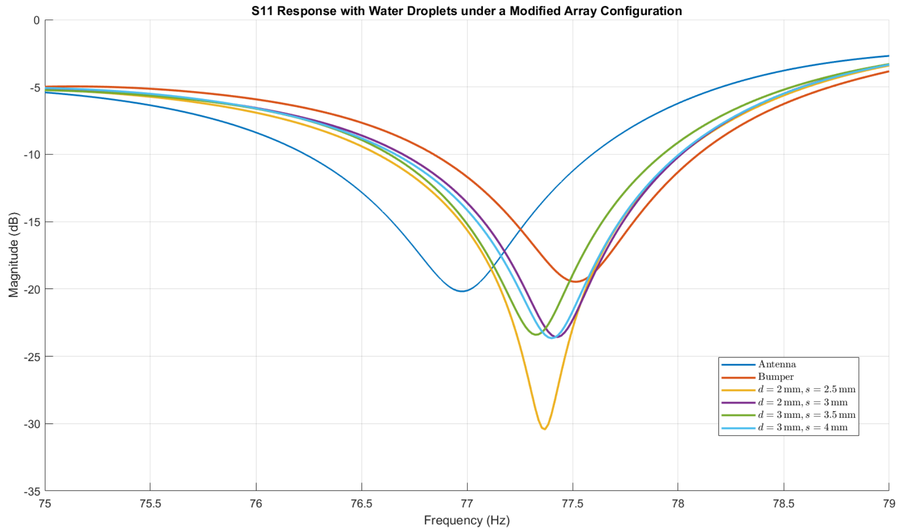

(a) Impact of water droplets and bumper on the antenna performance: reflection coefficient (S11)

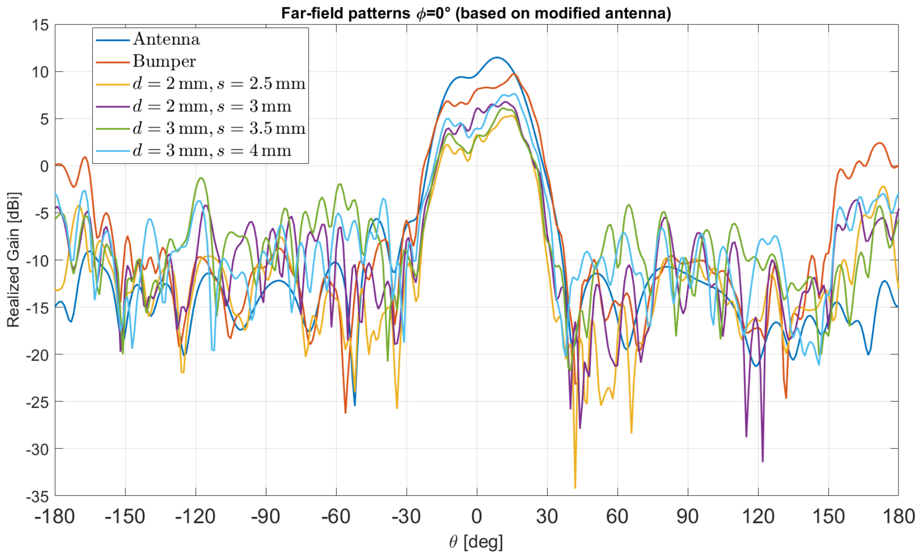

(b) $\phi = 0$ degrealized gain

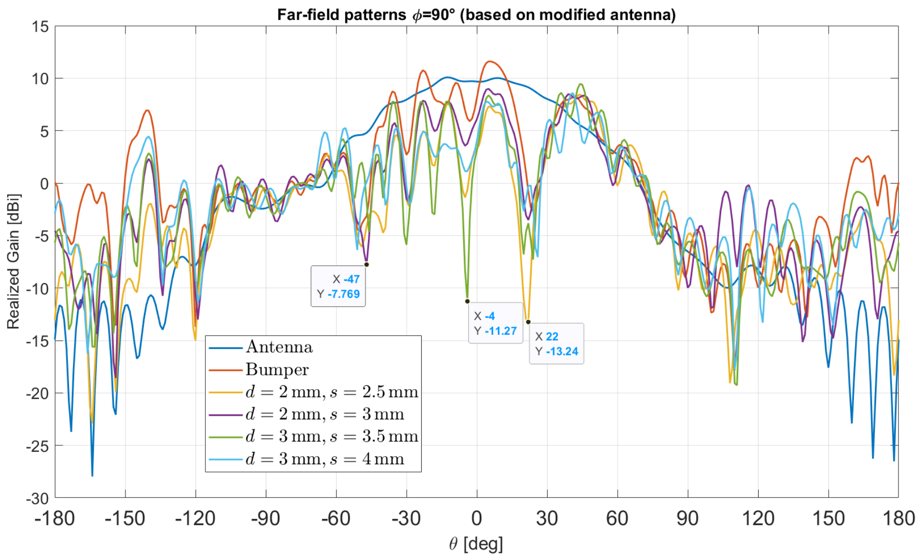

(c) $\phi = 90$ deg realized gain

Figure 2.17: Effect of water-droplet configurations on the bumper on higher resolution antenna subarray performance in terms of S11 and far-field realized gain.

quantitative evaluation of their impact on subarray performance. Comparisons between free-space conditions and various bumper configurations demonstrated attenuation and radiation pattern distortion introduced by the bumper. In particular, the bumper-to-antenna distance was found to cause significant variations in the realized gain pattern of the antenna subarray, indicating the need for careful calibration when assembling the antenna behind the bumper. In contrast, variations in bumper size and curvature resulted in relatively smaller changes in antenna performance.

To further approximate realistic environmental conditions, rainwater effects were subsequently incorporated by superimposing uniform water layers and discrete water droplets on the bumper surface.

To support further MIMO radar applications, the antenna configuration was refined by adjusting the transmit element spacing, resulting in a higher resolution antenna model. A comprehensive comparison was performed on this modified model across several scenarios, including free-space conditions, bumper obstruction, and bumper obstruction with overlaid rainwater layers or droplets of varying sizes. Key electromagnetic parameters, including S11 and realized gain patterns, were collected and evaluated, providing insight into the combined influence of structural and environmental factors on antenna performance. It has been observed that rainwater droplets of different dimensions on the bumper surface contributes to significant but different attenuation in subarray performance, while uniform water layers of varying thicknesses lead to very minor and more uniform performance degradation.

3 DoA Estimation Algorithms

3.1 FMCW Waveform and MIMO Configuration

3.1.1 FMCW Parameters

Previous chapter examined the electromagnetic characteristics of the automotive radar antenna system with full-wave CST simulations, focusing on the impact of bumper structures and precipitation on signal propagation. The simulations demonstrated that environmental and structural factors induce significant amplitude and phase distortions in the antenna's radiation characteristics, consequently modifying the effective antenna array signal perceived by the radar system. Building upon the electromagnetic modeling results obtained , this chapter shifts the focus to signal processing and DoA estimation for automotive FMCW MIMO radar. The degraded antenna responses obtained from CST simulations are incorporated into the radar signal model alongside the ideal array assumptions to evaluate their combined impact on DoA estimation algorithms. In addition to the degraded antenna responses derived from CST electromagnetic simulations, an ideal uniform linear array (ULA) model is also employed as a reference, with the array manifold directly generated in MATLAB under idealized assumptions. MATLAB serves as a signal processing platform to incorporate the CST-derived array responses and ULA with the FMCW waveform and MIMO configuration, facilitating a systematic assessment of Beamscan, MUSIC, and MVDR algorithms under representative bumper and water-induced situations. This two-step methodology delineates the separation between electromagnetic modeling and signal processing analysis, while ensuring that practical antenna and propagation effects are accurately represented in the DoA performance evaluation.

The radar system utilizes a frequency-modulated continuous-wave (FMCW) waveform, wherein the instantaneous frequency changes linearly over time during each chirp. The conveyed signal can thus be shown as a linearly frequency-modulated waveform. This modulation encodes the target distance through the time delay of the received echo, while the target's relative velocity introduces an extra Doppler frequency shift.

When the transmitted signal propagates toward a target, it is reflected back to the radar with a time delay τ proportional to the target range and a Doppler shift. The received signal is mixed with a replica of the transmitted signal, producing a beat signal whose frequency depends on both range and velocity.

The FMCW waveform is designed to achieve a target range resolution of $\Delta R = 1$ m. Using the standard radar relation

$$\Delta R = \frac{c}{2B}, \tag{3.1}$$

the required sweep (chirp) bandwidth B is

$$B = \frac{c}{2\Delta R} \approx \frac{3 \times 10^8 m/s}{2 \times 1\ m} = 150\ MHz. \tag{3.2}$$

To support a maximum unambiguous range $R_{\max} = 200m$, the maximum round-trip time is

$$\tau_{\max} = \frac{2R_{\max}}{c} \approx 1.333\mu s. \tag{3.3}$$

We select the chirp sweep time T_{sweep} such that target echoes are contained well within the chirp interval and to meet system timing requirements; in this design the sweep time is scaled to $T_{sweep} = 7.33\mu s$. The waveform sampling rate is chosen to match the instantaneous bandwidth requirement $f_s = 150\ MHz$.

After dechirping, the beat signals from all receive channels are sampled and arranged into a multi-dimensional structure indexed by fast time, slow time, and antenna channels. The fast-time dimension, corresponding to the samples within each chirp, represents range information; the slow-time dimension, defined by the chirp index, captures Doppler-induced phase variations associated with target velocity; and the spatial dimension, formed by the transmit–receive antenna pairs, encodes angular information. Collectively, these dimensions constitute a three-dimensional radar data cube comprising range, Doppler, and spatial samples.

The acquired radar data are subsequently processed to extract target parameters, including range, velocity, and angle. First, a one-dimensional fast-time Fourier transform (FFT) is applied to the beat signals from each receive channel to generate range profiles. Next, a slow-time FFT is performed along the chirp sequence for each range bin to produce range–Doppler maps, from which target velocity can be inferred. Range bins containing significant signal energy are then selected based on a threshold to suppress noise and reduce computational load. Finally, spatial processing techniques, such as conventional beamforming or high-resolution DoA algorithms, are applied across the virtual antenna array to estimate target angles.

The FMCW waveform generation, range-Doppler processing, and spatial DoA estimation using the Beamscan algorithm are implemented in MATLAB based on the official example ”Increasing Angular Resolution with Virtual Arrays” available at [27]. The CST-derived antenna realized gain in both amplitude and phase are incorporated into the MATLAB-based virtual array using the phased.CustomAntennaElement class, alongside an ideal uniform linear array (ULA) model to construct the radar data for DoA analysis for reference.

3.1.2 MIMO Configuration

To achieve high angular resolution, the radar employs a multiple-input multiple-output (MIMO) architecture consisting of $N_t = 2$ transmit antennas and $N_r = 4$ receive antennas. Two MIMO transmission schemes are implemented: time-division multiplexing (TDM) and phase-coded MIMO. In the TDM scheme, only one transmit antenna is active during each chirp while all receive antennas simultaneously capture the backscattered signals. By sequentially activating the transmit antennas across successive chirps, a virtual array of $N_{virt} = N_t \times N_r = 8$ elements is synthesized, and the DoA can be estimated based on the phase differences across the channels.

In contrast, the phase-coded MIMO scheme allows multiple transmit antennas to operate simultaneously, each modulated by an orthogonal phase code derived from a Hadamard matrix. The received superimposed signals are decoded to separate the contributions of each transmitter, after which the recovered channels are concatenated to construct the virtual array, enabling DoA estimation analogous to the TDM case. The MATLAB implementation follows the official Phased Array Toolbox example “Increasing Angular Resolution with MIMO Radars” [27], with the CST derived antenna realized gain incorporated into each virtual array element using ‘phased.CustomAntennaElement. This ensures that the simulated array accurately reflects the amplitude and phase characteristics of the practical antenna, while maintaining a reproducible and fully parameterized signal processing workflow.

To achieve transmit orthogonality, a Hadamard is applied across consecutive sweeps. And the Hadamard matrix of order two is given by

$$\mathbf{W} = \begin{bmatrix} 1 & 1 \\ 1 & -1 \end{bmatrix}. \tag{3.4}$$

During the m-th sweep, the transmitted signal from the k-th transmit antenna is expressed as

$$x_k^{(m)}(t) = w_k^{(m)} s(t), \quad k = 1, 2, \tag{3.5}$$

where $s(t)$ denotes the baseband FMCW waveform and $w_k^{(m)} \in \{+1, -1\}$ is the Hadamard phase coding coefficient.

Specifically, the coding vector for the m-th sweep is defined as

$$\mathbf{w}^{(m)} = \begin{cases} \begin{bmatrix} 1 \\ 1 \end{bmatrix}, & \text{if } m \text{ is odd,} \\ \begin{bmatrix} 1 \\ -1 \end{bmatrix}, & \text{if } m \text{ is even.} \end{cases} \tag{3.6}$$

Thus, both transmit antennas remain active during every sweep, while transmit orthogonality is preserved through phase coding across consecutive sweeps.

3.2 Beamscan Algorithm

3.2.1 Beamscan Algorithm Overview

The beamscan algorithm generates a conventional beam, scans it across the designated angular region, and displays the magnitude squared of the output [28]. Let the k-th snapshot vector in the frequency domain be defined as follows:

$$\mathbf{X}_k = \begin{bmatrix} x_k(1) & x_k(2) & \dots & x_k(N) \end{bmatrix}^T \tag{3.7}$$

For K snapshots, the Bartlett beamformer (conventional beamforming) spatial spectrum is given by:

$$\hat{P}_B(\theta) = \frac{1}{K} \sum_{k=1}^{K} \left| \mathbf{v}^H(\theta) X_k \right|^2 \tag{3.8}$$

$$= \sum_{k=1}^{K} \mathbf{v}^H(\theta) \left\{ \frac{1}{K} \mathbf{X}_k \mathbf{X}_k^H \right\} \mathbf{v}(\theta), \quad -\pi < \theta < \pi \tag{3.9}$$

(3.10)

where $\mathbf{v}(\theta)$ is the steering vector corresponding to angle θ. Here $\mathbf{v}(\theta)$ explicitly incorporates the angle-dependent amplitude (realized gain) and phase responses of the antenna elements obtained from CST simulations. These patterns can be embedded in MATLAB using the `phased.CustomAntennaElement` object, while an isotropic ULA can still be used for comparison via MATLAB `phased.ULA` object. Defining the sample spectral matrix as

$$\mathbf{C}_x = \frac{1}{K}\sum_{k=1}^{K}\mathbf{X}_k\mathbf{X}_k^H, \tag{3.11}$$

the Bartlett spatial spectrum can be equivalently written as

$$\hat{P}_B(\theta) = \mathbf{v}^H(\theta)\mathbf{C}_x\mathbf{v}(\theta). \tag{3.12}$$

$\hat{P}_B(\theta)$ provides an estimate of the spatial spectrum. In our application, we select the D prominent peaks of $\hat{P}_B(\theta)$ and label them as $\hat{\theta}_i$, where $i = 1, 2, \ldots, D$, under the assumption that the number of signals D is known beforehand.

3.2.2 Antenna–bumper–water layer analysis

In the water-layer scenario discussed in Chapter 2.5, the antenna array is positioned on the bumper model, such that the bumper obstructs the array's line of sight. Additional configurations correspond to progressively thicker water layers applied to the bumper surface, simulating increasing obstruction. The beamscan DoA estimation in this scenario utilizes steering vectors that incorporate the angle-dependent amplitude (Figure 2.13c) and phase responses of the antenna elements obtained from CST simulations as mentioned in previous beamscan formulation. For the MVDR and MUSIC algorithms, the same steering vectors are used, ensuring consistency across all DoA estimation methods; further details are omitted here for brevity, as the procedure is analogous to the Beamscan case. Test angles were selected based on the realized gain patterns obtained from CST simulations (Figure 2.13c), typically including one angle exhibiting pronounced attenuation and another angle with relatively minimal impact. This selection allows for a clear assessment of DoA performance under both strong and weak signal degradation.

The high consistency of all obstructed array conditions in water-layer model allows the subsequent analysis to concentrate on the minimum received power across configurations. The subsequent analysis focuses primarily on the minimum received power across configurations to evaluate DoA performance at different angles. The lowest power levels were recorded at -50° (-5.6 dB), 23° (-3.9 dB), and -30° (2.6 dB). Among all evaluated directions, the angles of 6° and -23° exhibited comparatively strong and stable responses, with power levels of approximately 11.5 dB and 10.7 dB, respectively. Consequently, these angles are adopted as reference points in the subsequent analysis.

Examining the TDM MIMO Beamscan results in Figure 3.1, distinct behaviors are observed at the tested angles. At 23° (in Figure 3.1a), the main-lobe amplitude is severely attenuated, falling below the surrounding sidelobes, making this angle effectively undetectable. At -30° (in Figure 3.1b), the main lobe is attenuated and slightly shifted from the true target direction, indicating that the DoA estimate is biased due to the obstruction. In contrast, at -50° (in Figure 3.1c), the lobe amplitude is reduced but remains sufficiently prominent for DoA estimation.

These observations indicate that the impact of water-layer obstruction on DoA performance is angle-dependent: some angles, like 23°, may become blind spots due to strong lobe suppression, while others, may remain detectable,or exhibiting a small angular bias in the estimated direction.

The same sets of test angles was evaluated under the Phase-Coded configuration in the water-layer scenario to assess the impact of waveform type on DoA performance. The received

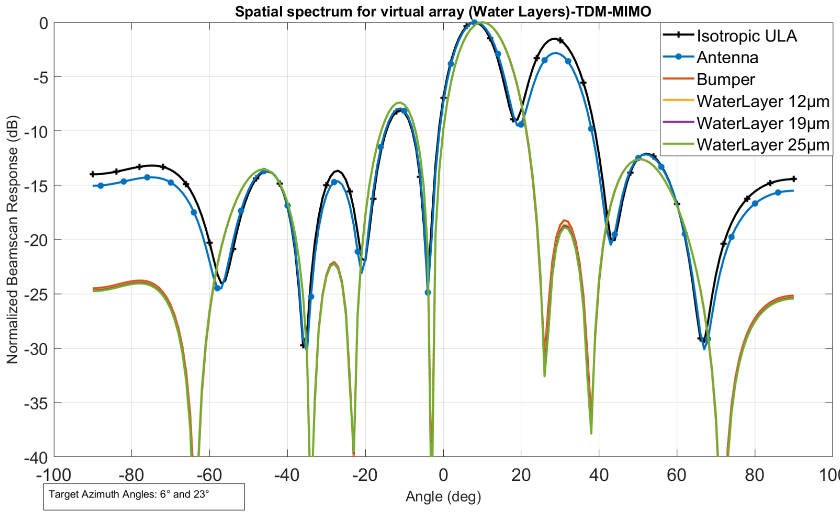

(a) Targets at 6° and 23°

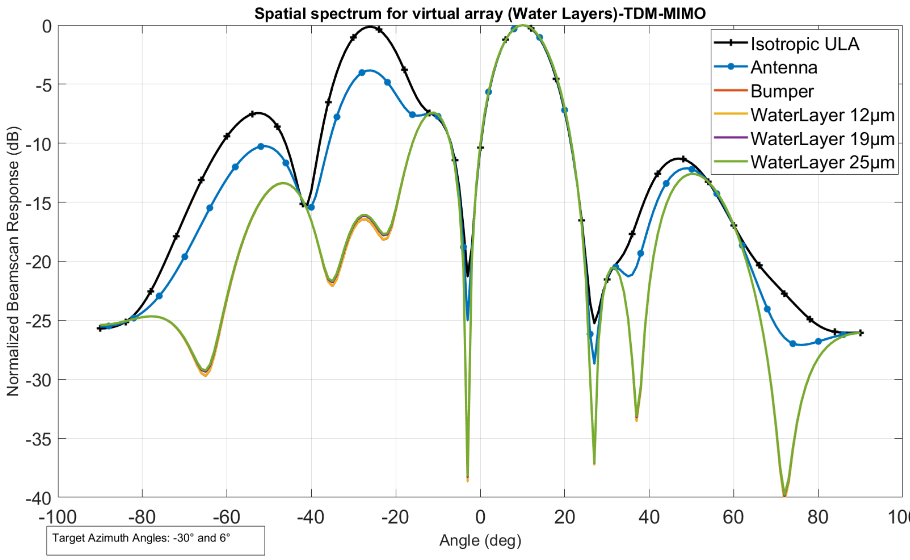

(b) Targets at −30° and 6°

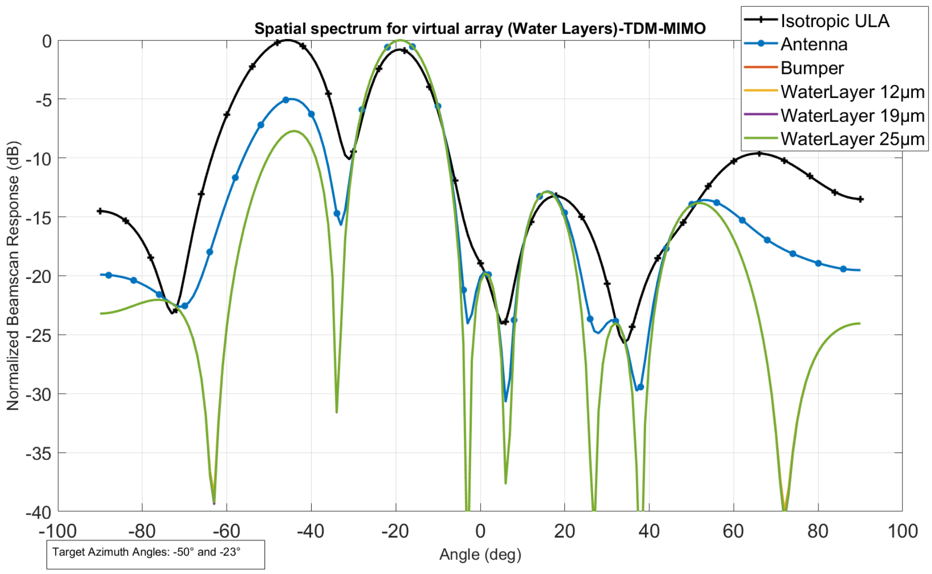

(c) Targets at −50° and −23°

Figure 3.1: Beamscan results of the TDM MIMO radar in the water-layer scenarios at the tested angles. In each test group, pronounced main-lobe attenuation is observed at (a)−30°, (b)23°, and (c)−50°, respectively.

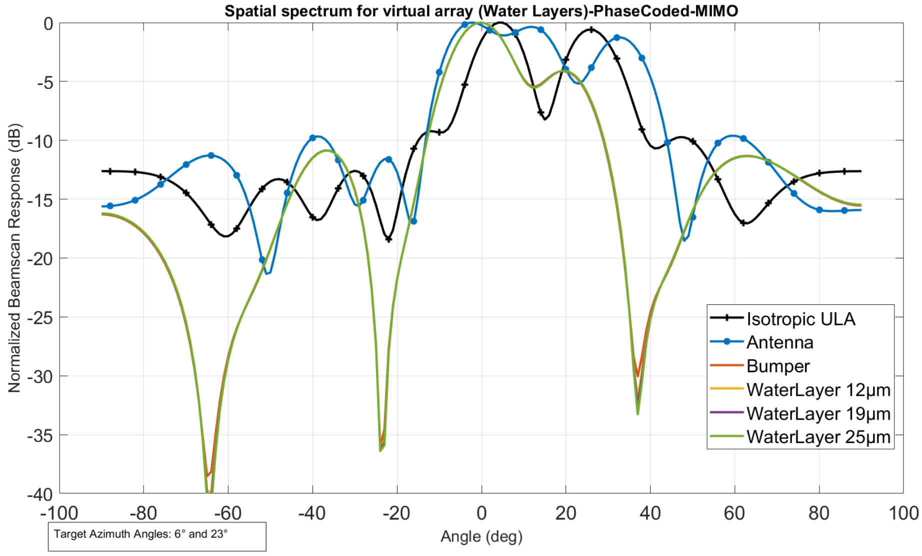

(a) Targets at 6° and 23°

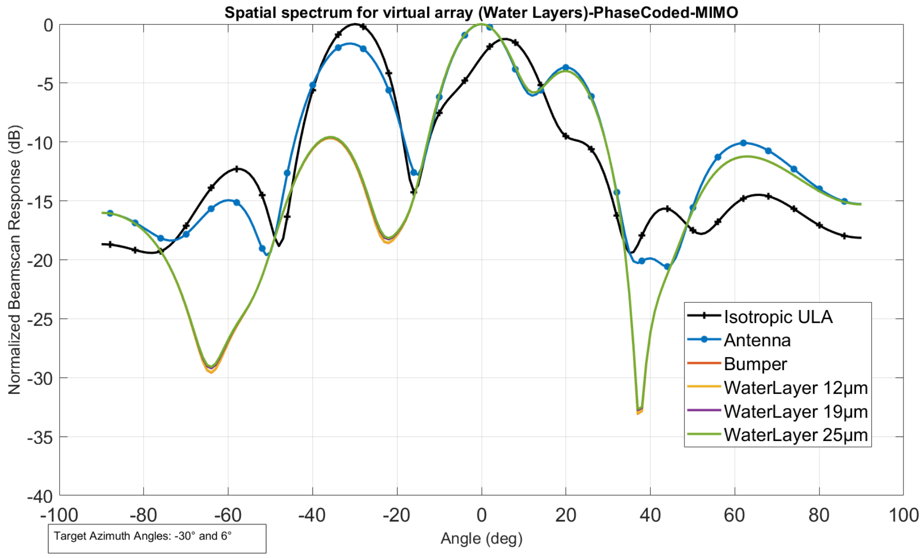

(b) Targets at $-30°$ and 6°

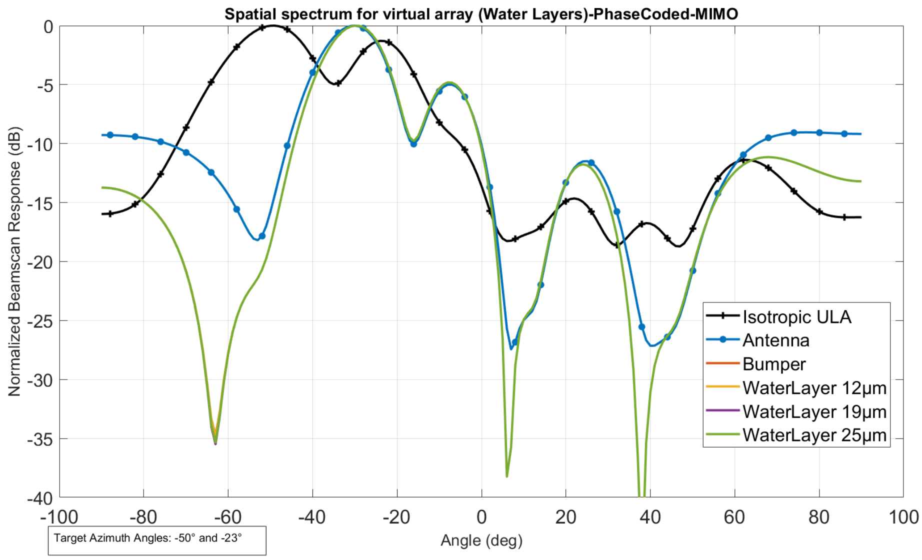

(c) Targets at $-50°$ and $-23°$

Figure 3.2: Beamscan results of phase-coded MIMO radar in the water-layer scenarios at the tested angles. In each test group, pronounced main-lobe attenuation is observed at (a) $-30°$, (b) 23°, and (c) $-50°$, respectively.

power responses measured with Beamscan are shown in Figure 3.2, which allows for direct comparison with the TDM MIMO radar results presented in Figure 3.1.

3.2.3 Antenna–bumper–water droplets analysis

Based on the observed radiation patterns (Figure 2.17c), with same FMCW configuration, tests on specific angles are employed to evaluate the impact of water-droplet configurations on target angle arrival estimation. As shown in Figure 2.17c, at positive angles, in the region between 18° and 25°, all cases except for the standalone array without any obstruction, exhibit a noticeable reduction, with gains falling below −10 dB. The most significant attenuation occurs at 22°, while the reference angle −23° remains comparatively less affected. The Beamscan spatial spectrum in Figure 3.3 for a virtual array demonstrates that at target azimuths corresponding to -23° and 22°, amplitude of the lobes are significantly reduced in the water-droplet cases,and is most severe for Case 1. The attenuation trend is consistent with the realized gain level for each case. In addition to the TDM-MIMO configuration, the same set of test angles was evaluated under the Phase-Coded waveform in the water-droplet scenario, as shown in Figure 3.4.

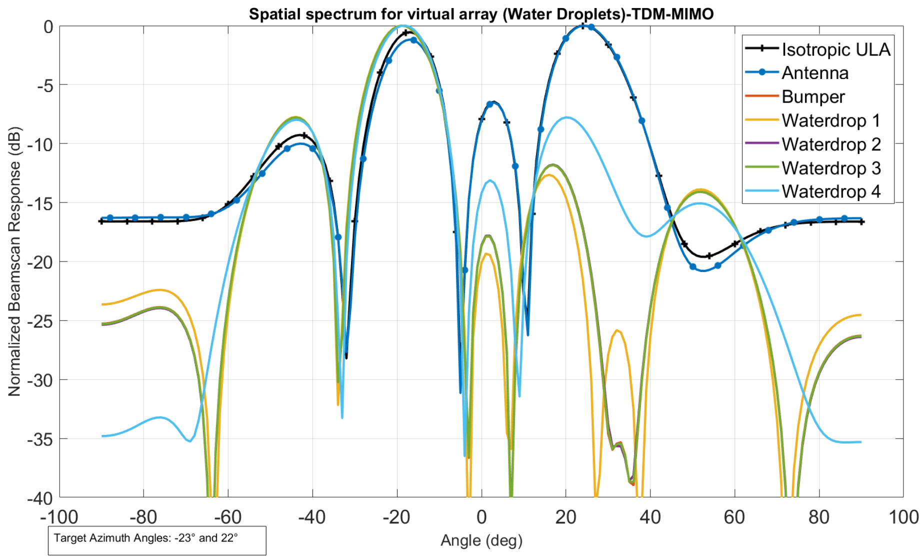

Figure 3.3: Beamscan result of TDM MIMO radar in the water-droplet scenario at the tested angles (−23° and 22°). Pronounced main-lobe attenuation is observed at 22° in this test.

Figure 3.5 presents the Beamscan result for tests at −18° and 10°, representing a negative-angle scenario where significant attenuation was observed. For Case 3, the realized gain at −18° experienced a reduction of approximately 12.4 dB, while other configurations were less affected. Although the peak was not completely eliminated, it exhibited a slight shift toward more positive angles, indicating that water droplet occlusion introduces both amplitude suppression and angular estimation bias. Similar effects were observed in the phase coded MIMO tests in Figure 3.6. the angular bias and main-lobe suppression are not specific to the radar waveform, but the phase coded waveform introduced a extra slight shift.

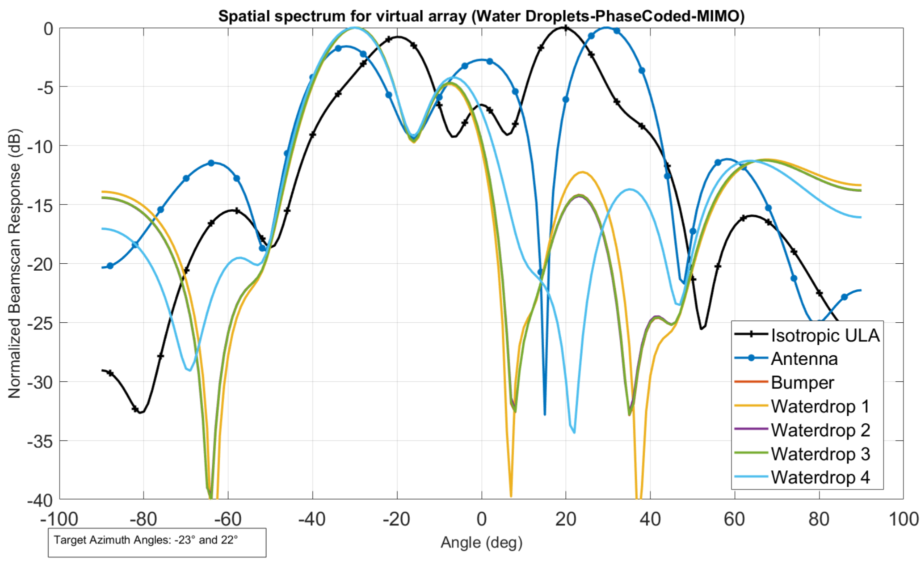

Figure 3.4: Beamscan result of phase-coded MIMO radar in the water-droplet scenario at the tested angles ($-23°$ and $22°$). Pronounced main-lobe attenuation is observed at $22°$ in this test.

3.3 MUSIC Algorithm

3.3.1 MUSIC Algorithm Overview

The MUSIC algorithm is an eigenvalue-based DoA estimation technique. Assuming the number of sources d is smaller than the number of sensors M ($d < M$), the received signal covariance matrix is given by:

$$\mathbf{R}_x = \mathbf{A}\mathbf{R}_s\mathbf{A}^H + \sigma^2\mathbf{I}_M \tag{3.13}$$
$$= \mathbf{U}_s(\mathbf{\Lambda}_s + \sigma^2\mathbf{I}_d)\mathbf{U}_s^H + \mathbf{U}_n(\sigma^2\mathbf{I}_{M-d})\mathbf{U}_n^H, \tag{3.14}$$

where $\mathbf{A} = [\mathbf{a}(\theta_1), \ldots, \mathbf{a}(\theta_d)]$ is the array steering matrix, $\mathbf{U}_s$ and $\mathbf{U}_n$ are the signal and noise subspaces, respectively, satisfying:

$$\text{span}(\mathbf{U}_s) = \text{span}(\mathbf{A}), \quad \mathbf{U}_n^H\mathbf{A} = 0. \tag{3.15}$$

In the above formulation, the array steering vector $\mathbf{a}(\theta)$ is not always assumed to be ideal. For the ideal reference scenario, an isotropic ULA is assumed for both transmit and receive antennas, and the corresponding array manifold is generated analytically in MATLAB utilizing the `phased.ULA` object. For practical cases, the steering vector includes angle-dependent realized gain and phase responses derived from comprehensive full-wave CST simulations. These non-ideal antenna patterns are incorporated into the array manifold utilizing the `phased.The CustomAntennaElement` object in MATLAB which enables the assignment of arbitrary magnitude and phase patterns to each individual antenna element. The DoAs $\{\theta_1, \ldots, \theta_d\}$ are estimated by finding the angles θ for which:

$$\mathbf{U}_n^H\mathbf{a}(\theta_i) = 0, \quad 1 \le i \le d. \tag{3.16}$$

Equivalently, the cost function is defined as:

$$J_{\text{MUSIC}}(\theta) = \frac{\|\mathbf{U}_n^H\mathbf{a}(\theta)\|^2}{\|\mathbf{a}(\theta)\|^2} \tag{3.17}$$
$$= \frac{\mathbf{a}^H(\theta)\mathbf{U}_n\mathbf{U}_n^H\mathbf{a}(\theta)}{\mathbf{a}^H(\theta)\mathbf{a}(\theta)}. \tag{3.18}$$

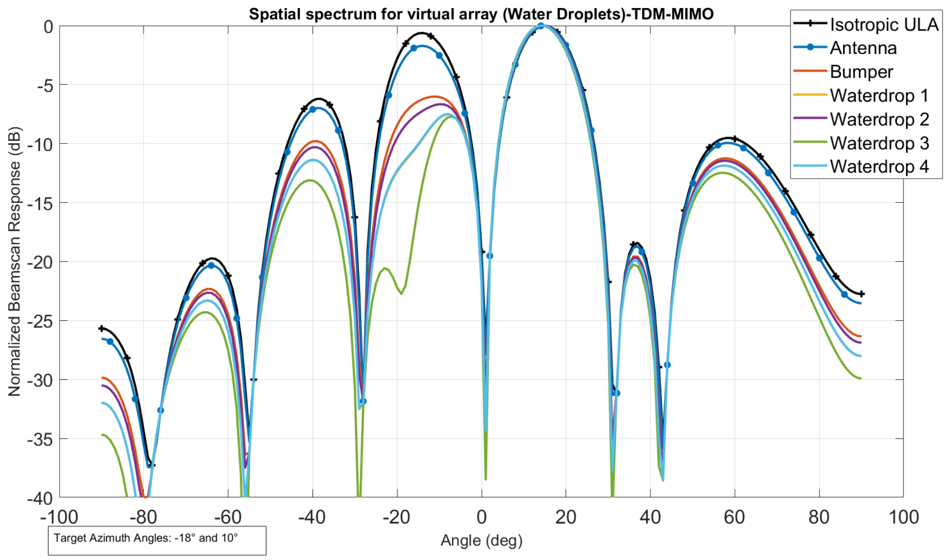

Figure 3.5: Beamscan result of TDM MIMO radar in the water-droplet scenario at the tested angles. Pronounced main-lobe attenuation is observed at $-18°$ in this test.

The MUSIC spectrum is usually plotted as the inverse of $J_{\text{MUSIC}}(\theta)$. When the number of sources is smaller than the number of sensors ($d < M$), and for $N \to \infty$ or SNR $\to \infty$, the algorithm provides statistically consistent DoA estimates by selecting the d lowest local minima of $J_{\text{MUSIC}}(\theta)$.

3.3.2 Antenna–bumper–water layer analysis

The MUSIC algorithm is applied using the same CST derived (in Chapter 2.5) steering vectors as in the Beamscan analysis, while a subset of representative angles is selected for evaluation.

Figures 3.7 and 3.8 present the MUSIC spatial spectra for TDM and Phase-Coded MIMO radars, respectively, under the water-layer scenario at the same test angles. While the Beamscan results directly reflect the main-lobe amplitude reductions observed in the radiation patterns, the MUSIC spectra exhibit a more complex behavior: severe attenuation can shift the peaks of the MUSIC spectrum, making it sometimes difficult to directly associate a specific peak with the corresponding radiation pattern attenuation or detectability blind spot. Overall, compared with Beamscan, the MUSIC algorithm produces significantly sharper and more distinct spectral peaks, leading to improved angular resolution and more accurate angle-of-arrival estimation. This advantage is especially apparent at angles where the received signal undergoes only minor attenuation, for which MUSIC reliably produces well-defined and accurately placed peaks. In situations with significant signal degradation due to external impediments, such as layers or drops of rainwater, MUSIC is comparatively less impacted than Beamscan. Although significant attenuation may lead to a drop in peak displacement or amplitude, the principal MUSIC peak typically remains discernible, facilitating dependable target detection even when Beamscan patterns are substantially altered.

MUSIC efficiently mitigates sidelobe-related ambiguities that frequently impede Beamscan-based analysis. Consequently, peak identification in the MUSIC spectrum is predominantly clear both via visual examination and automatic data processing, obviating the necessity for heuristic peak-selection criteria typically required for Beamscan. This characteristic renders MUSIC exceptionally adept for accurate DoA determination in challenging environmental settings.

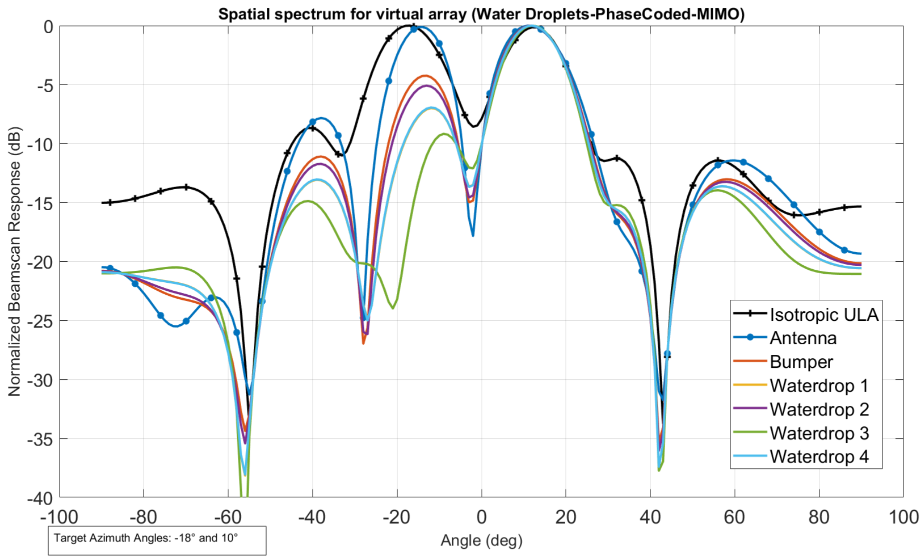

Figure 3.6: Beamscan result of phase-coded MIMO radar in the water-droplet scenario at the tested angles. Pronounced main-lobe attenuation is observed at -18° in this test.

3.3.3 Antenna–bumper-water droplets analysis

Figure 3.9 shows the MUSIC spatial spectrum of the TDM MIMO radar under bumper obstruction and water-droplet conditions, while Figure 3.10 presents the corresponding results for the phase-coded MIMO radar using the same set of test angles. Although the radiation pattern analysis indicates noticeable attenuation at -18°, the MUSIC spectra in both configurations are still able to resolve the target at this angle. A slight shift of the spectral peak is observed, which is attributed to the reduced signal strength and phase perturbations introduced by the water droplets. Nevertheless, the dominant peak remains clearly identifiable, demonstrating the robustness and stability of the MUSIC algorithm in angle-of-arrival estimation even under moderate radiation pattern degradation.

3.4 MVDR Algorithm

3.4.1 MVDR Algorithm Overview

Consider an array receiving a single plane-wave signal. The frequency-domain snapshot can be expressed as:

$$\mathbf{X}(\omega) = \mathbf{X}_s(\omega) + \mathbf{N}(\omega) \tag{3.19}$$

where the signal component is:

$$\mathbf{X}_s(\omega) = \mathbf{F}(\omega)\mathbf{v}(\omega; k_s) \tag{3.20}$$

Here, $\mathbf{v}(\omega; k_s)$ is the array manifold (steering) vector for a plane wave with wavenumber k_s. And $\mathbf{F}(\omega)$ is snapshot in frequency-domain of the source signal. The noise vector $\mathbf{N}(\omega)$ is assumed to be zero-mean with covariance matrix:

$$\mathbf{S}_n(\omega) = \mathbb{E}[\mathbf{N}(\omega)\mathbf{N}^H(\omega)] \tag{3.21}$$

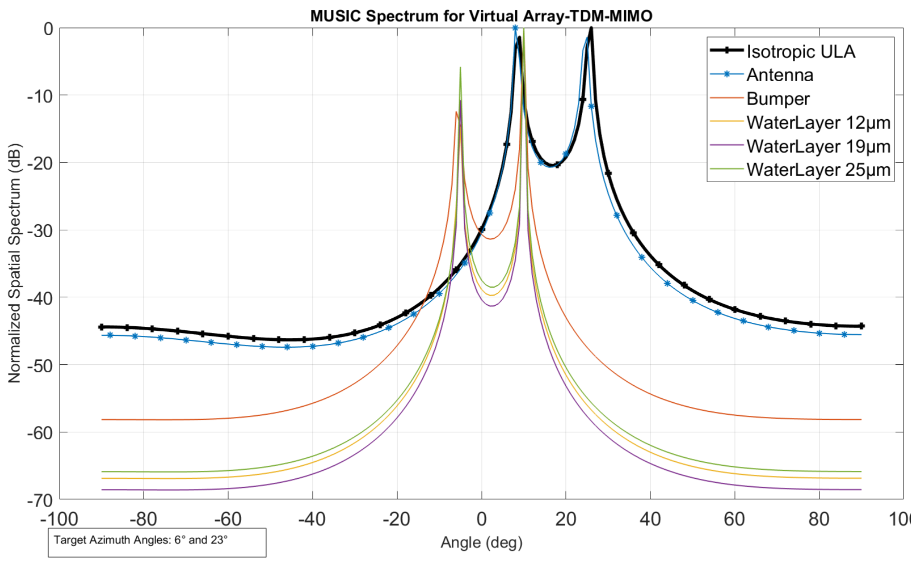

(a) Targets at 6° and 23°

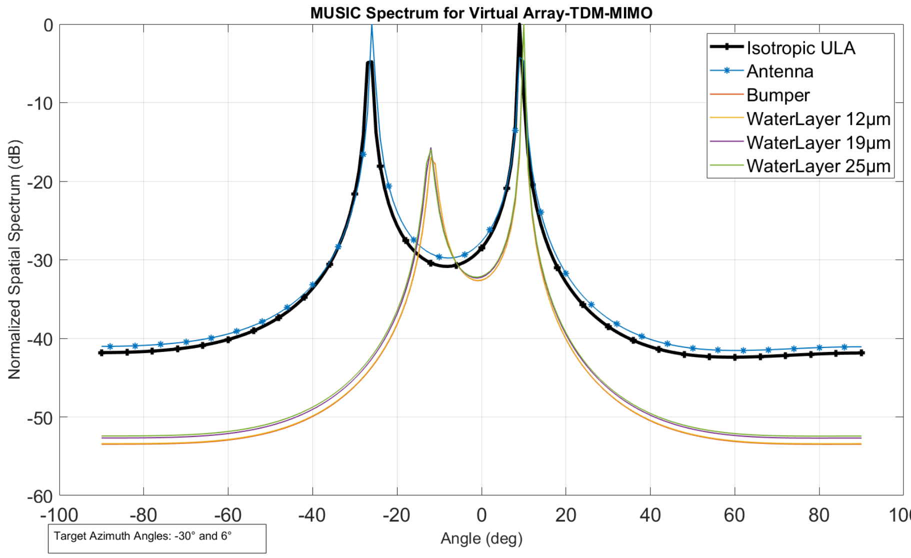

(b) Targets at −30° and 6°

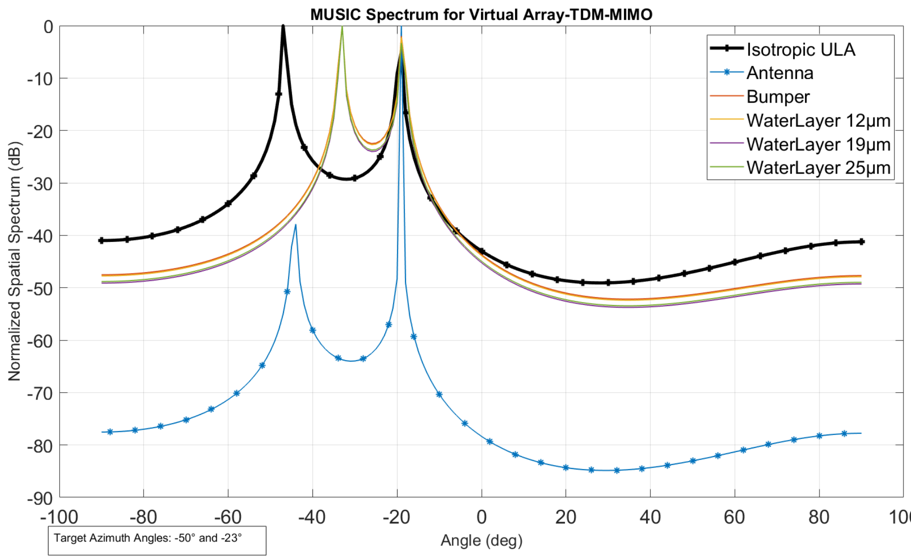

(c) Targets at −50° and −23°

Figure 3.7: MUSIC results of the TDM MIMO radar in the water-layer scenario at the tested angles.

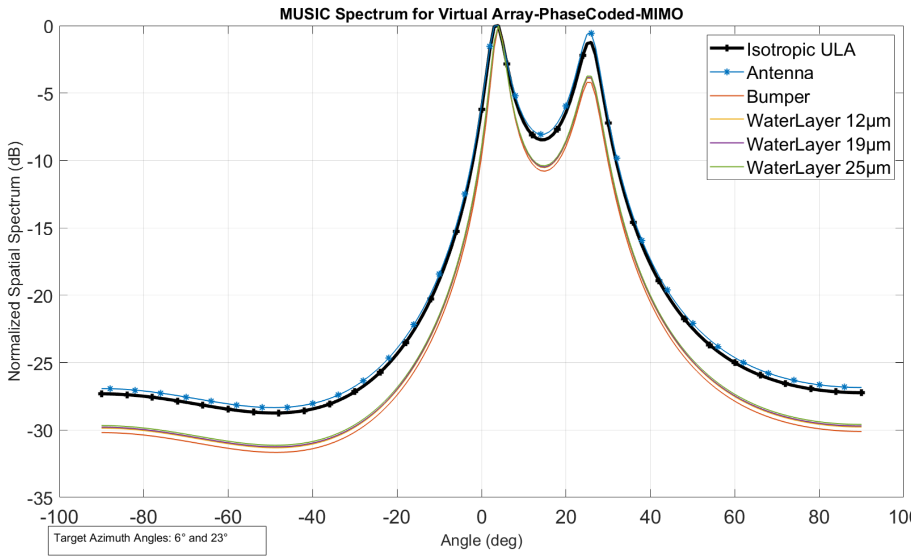

(a) Targets at 6° and 23°

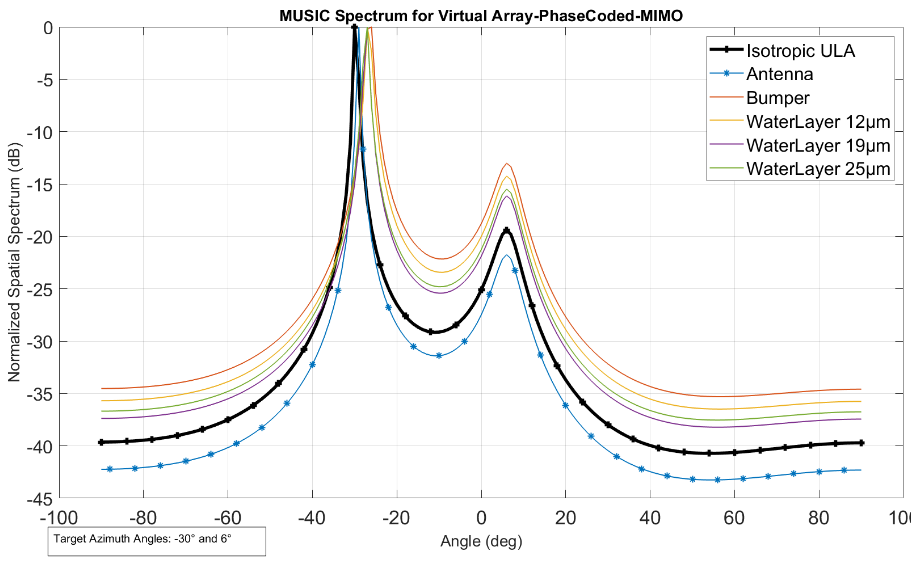

(b) Targets at $-30°$ and 6°

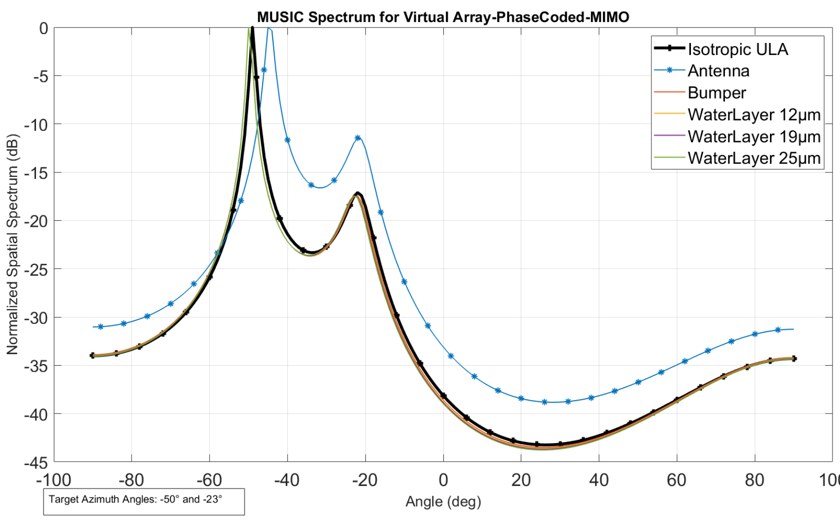

(c) Targets at $-50°$ and $-23°$

Figure 3.8: MUSIC results of the phase-coded MIMO radar in the water-layer scenario at the tested angles.

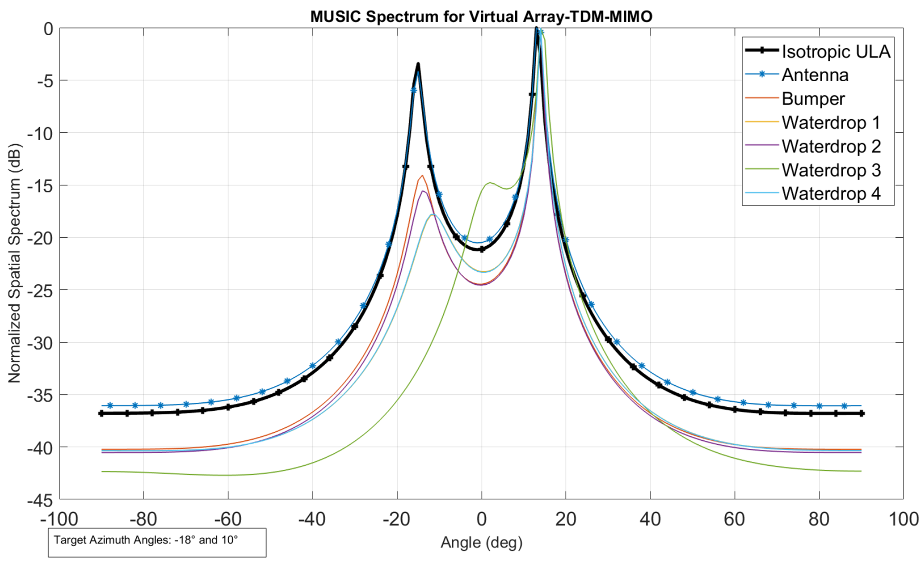

Figure 3.9: MUSIC spatial spectrum of the TDM MIMO radar in the water-droplet scenario, with targets located at -18° and 10°.

The beamformer output is given by:

$$\mathbf{Y}(\omega) = \mathbf{w}^H(\omega)\mathbf{X}(\omega) \tag{3.22}$$

$$= \underbrace{\mathbf{w}^H(\omega)\mathbf{X}_s(\omega)}_{\text{signal term}} + \underbrace{\mathbf{w}^H(\omega)\mathbf{N}(\omega)}_{\text{noise term } Y_n(\omega)}. \tag{3.23}$$

The mean-square value of the output noise is then given by

$$\mathbb{E}\left[|\mathbf{Y}_n(\omega)|^2\right] = \mathbf{w}^H(\omega)\mathbf{S}_n(\omega)\mathbf{w}(\omega), \tag{3.24}$$

This expression leads to the MVDR optimization problem [29] . The MVDR beamformer aims to maintain a distortionless response in the desired signal direction, and minimize the output noise power:

$$\min_{\mathbf{w}} \quad \mathbf{w}^H\mathbf{S}_n\mathbf{w} \tag{3.25}$$

$$\text{subject to} \quad \mathbf{w}^H\mathbf{v} = 1 \tag{3.26}$$

Finally, the MVDR weight vector is:

$$\boxed{\mathbf{w}_{\text{MVDR}} = \frac{\mathbf{S}_n^{-1}\mathbf{v}}{\mathbf{v}^H\mathbf{S}_n^{-1}\mathbf{v}}} \tag{3.27}$$

The corresponding spatial power spectrum is:

$$P_{\text{MVDR}}(\omega) = \frac{1}{\mathbf{v}^H(\omega)\mathbf{S}_n^{-1}(\omega)\mathbf{v}(\omega)} \tag{3.28}$$

The array steering vector $\mathbf{v}(\omega; k_s)$ incorporates the angle-dependent amplitude of realized gain and phase responses of the antenna elements obtained from CST simulations. These practical antenna patterns are embedded in MATLAB using the `phased.CustomAntennaElement` object. An ideal isotropic ULA can also be used as a reference via the `phased.ULA` object.

The array steering vector $\mathbf{v}(\omega; k_s)$ explicitly incorporates the angle-dependent amplitude and phase responses of the antenna elements, as obtained from CST full-wave simulations. These

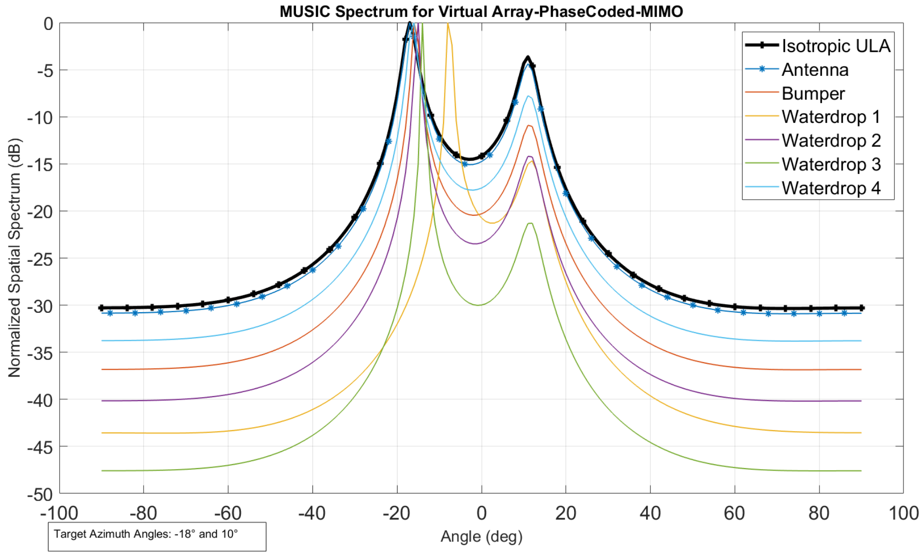

Figure 3.10: MUSIC spatial spectrum of the phase-coded MIMO radar in the water-droplet scenario, with targets located at $-18°$ and $10°$.

practical antenna patterns are embedded in MATLAB using the `phased.CustomAntennaElement` object. For comparison, an ideal isotropic ULA can also be employed via the `phased.ULA` object.

3.4.2 Antenna–bumper–water layer analysis

Figure 3.11 presents the MVDR spatial spectra of the TDM MIMO radar under water-layer conditions. In this configuration, transmit antennas operate sequentially in time to preserve orthogonality, and the resulting spectra illustrate the estimated directions of arrival for targets located at the selected azimuth angles. The three test cases include both high-gain directions and angles previously identified as exhibiting increased attenuation in the radiation pattern analysis.

Figure 3.12 shows the corresponding MVDR results for the Phase-Coded MIMO radar under the same water-layer conditions. In this case, all transmit antennas operate simultaneously using distinct phase codes, enabling signal separation without time multiplexing. Overall, the MVDR spectra obtained from both transmission schemes exhibit similar angular responses, indicating that the presence of a uniform water layer introduces relatively consistent attenuation without causing severe distortion in the MVDR-based DoA estimation.

3.4.3 Antenna–bumper–water droplets analysis

Figures 3.13 and 3.14 show the MVDR spatial spectra of the TDM and phase-coded MIMO radars, respectively, for the water-droplet scenario with targets located at $-18°$ and $10°$. As discussed in the radiation pattern analysis, the $-18°$ direction experiences noticeable attenuation due to water droplet obstruction. Nevertheless, both transmission schemes are able to resolve the target at this angle using MVDR processing, with the dominant peak remaining clearly identifiable. A slight reduction in peak amplitude and minor angular deviation can be observed, reflecting the impact of signal degradation, while overall DoA estimation performance remains stable.

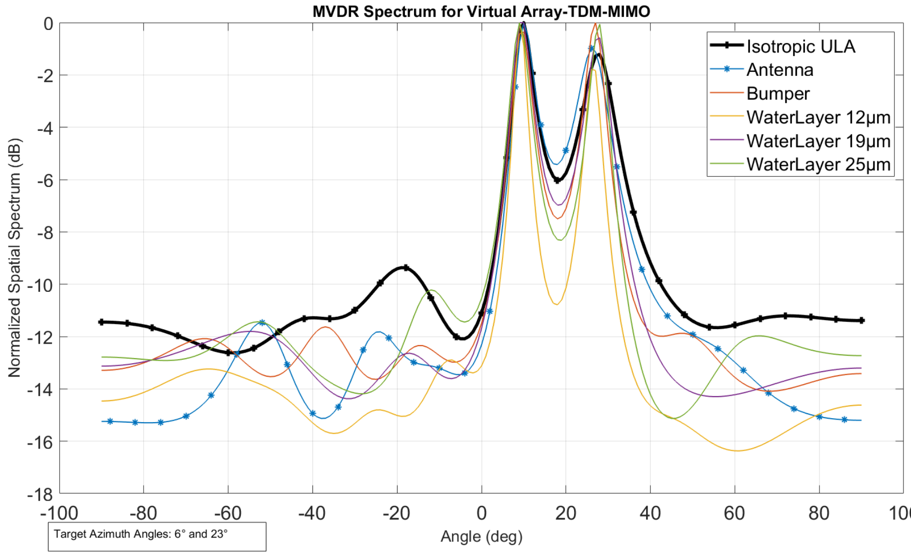

(a) Targets at 6° and 23°

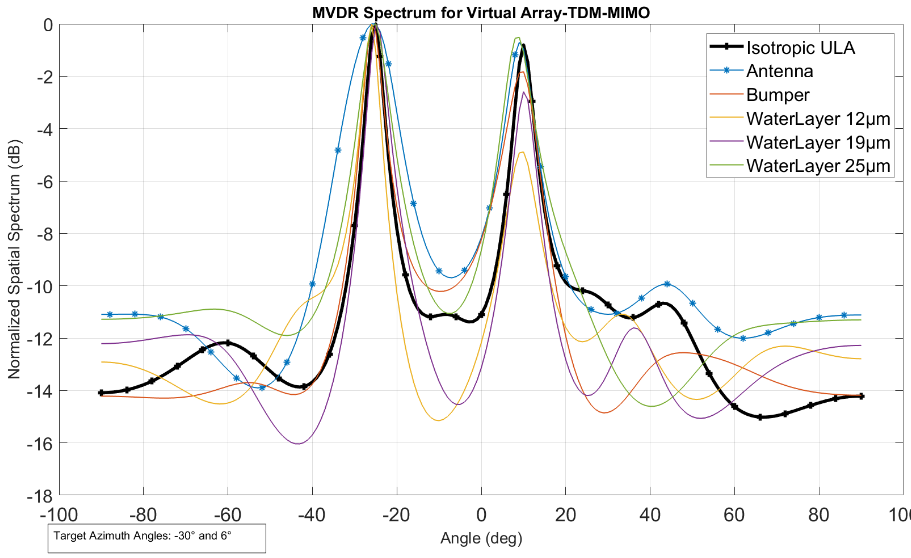

(b) Targets at −30° and 6°

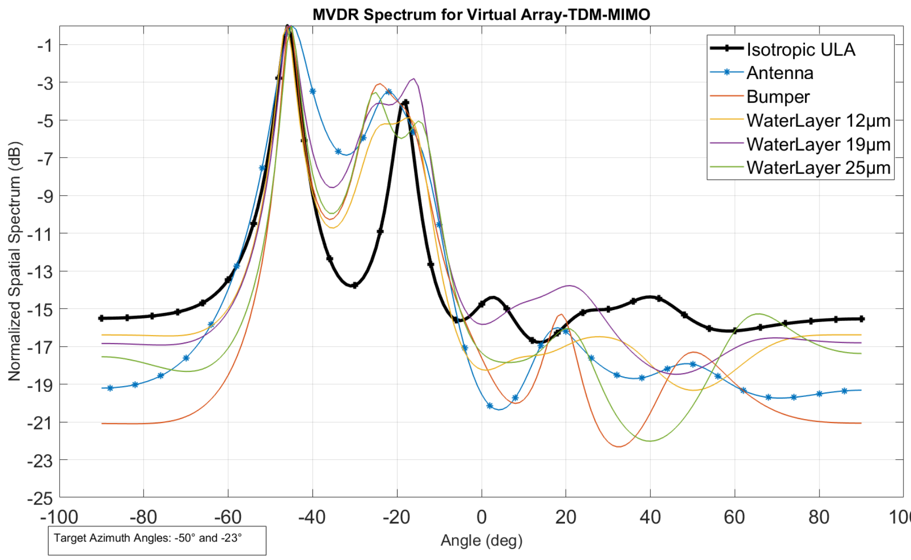

(c) Targets at −50° and −23°

Figure 3.11: MVDR results of the TDM MIMO radar in the water-layer scenario at the tested angles.

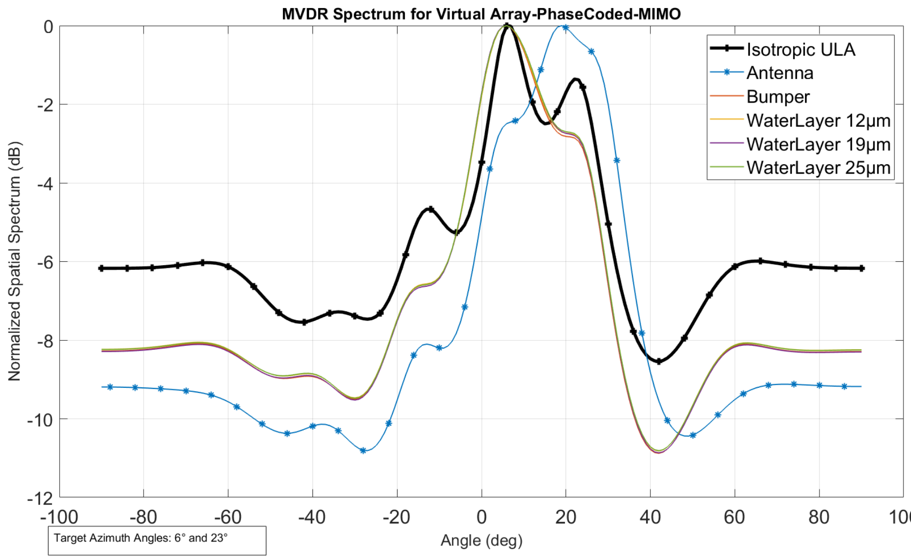

(a) Targets at 6° and 23°

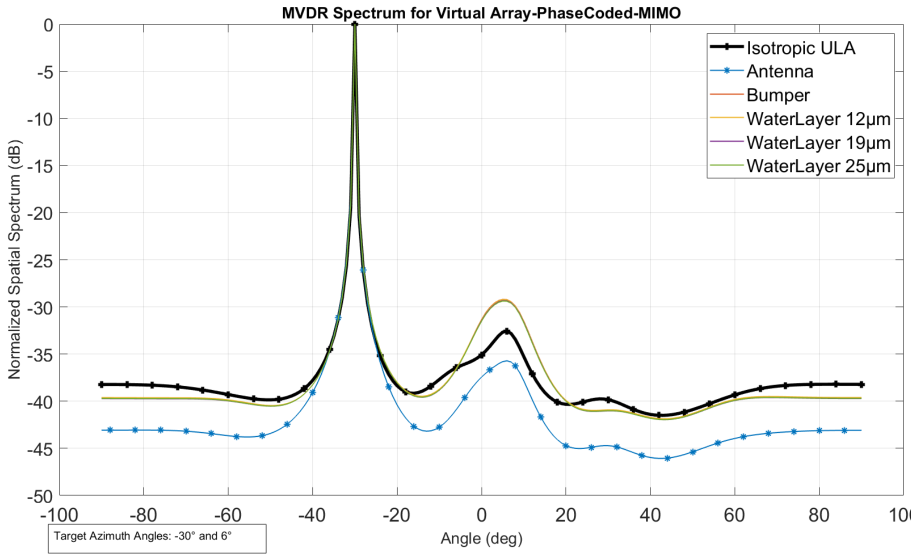

(b) Targets at $-30°$ and 6°

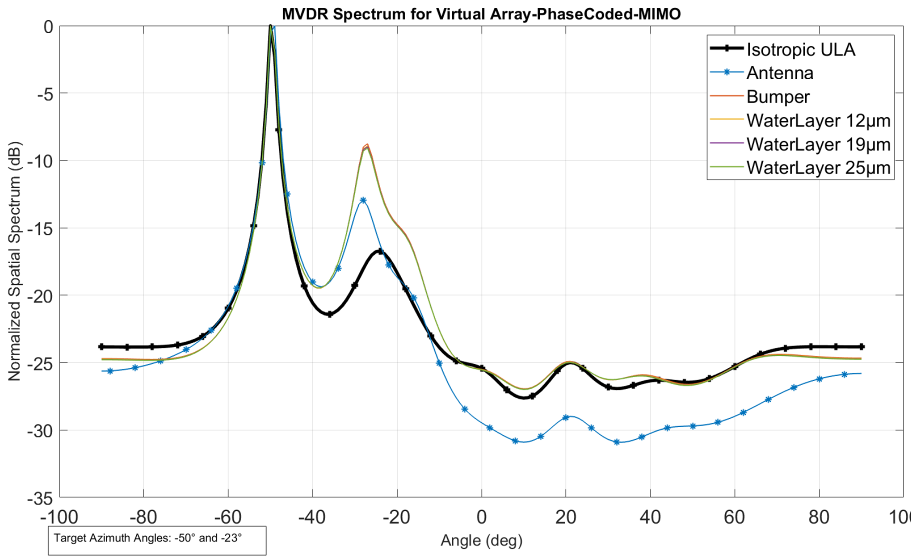

(c) Targets at $-50°$ and $-23°$

Figure 3.12: MVDR results of the phase-coded MIMO radar in the water-layer scenario at the tested angles.

Figures 3.15 and 3.16 present the corresponding MVDR results for the more challenging case of targets at $-30°$ and $10°$. In the angular region around $-30°$, severe attenuation was previously identified in the radiation pattern analysis. Although residual peaks may still be observed, their reduced prominence and positional instability highlight the limitations of MVDR-based DoA estimation under strong environmental obstruction.

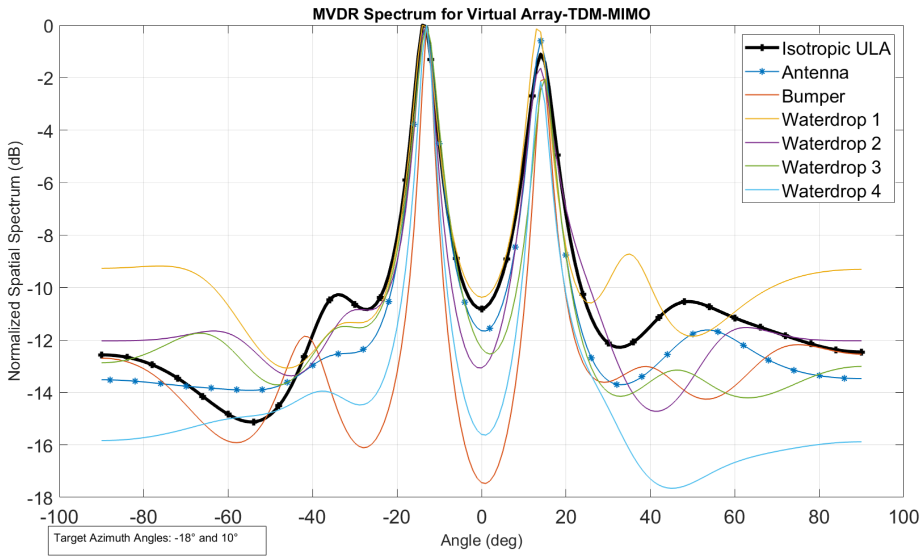

Figure 3.13: MVDR spatial spectrum of the TDM MIMO radar in the water-droplet scenario, with targets at $-18°$ and $10°$.

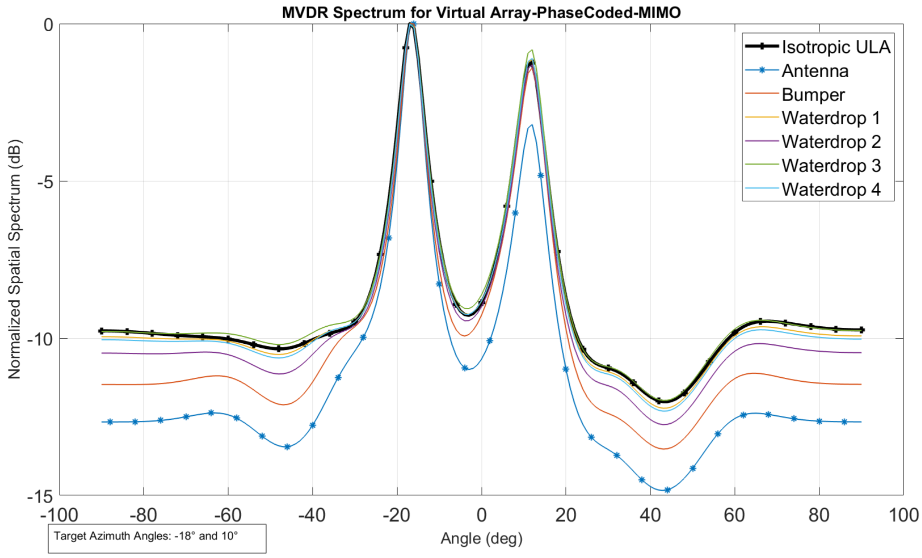

Figure 3.14: MVDR spatial spectrum of the phase-coded MIMO radar in the water-droplet scenario, with targets at $-18°$ and $10°$.

3.5 Conclusion

In this chapter, the deterministic DoA estimation performance under realistic electromagnetic conditions was investigated by incorporating the EM-level antenna responses obtained in Chapter 2 into FMCW radar signals with a Time-Division Multiplexing and Phase-Coded

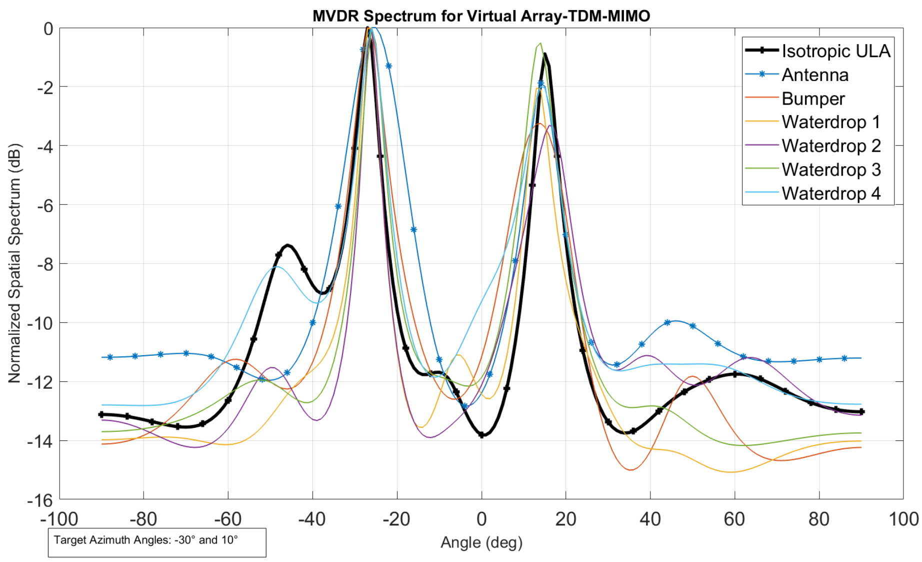

Figure 3.15: MVDR spatial spectrum of the TDM MIMO radar in the water-droplet scenario, with targets at $-30°$ and $10°$.

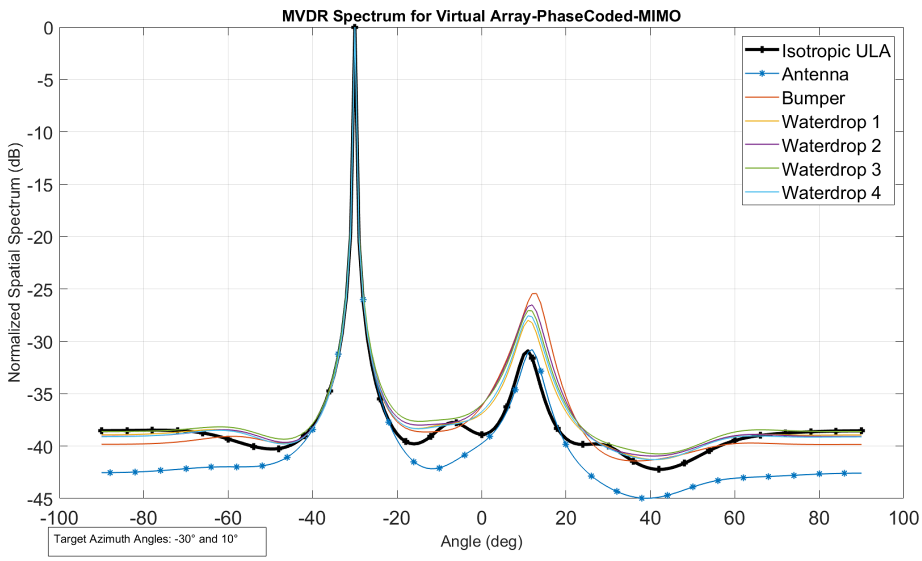

Figure 3.16: MVDR spatial spectrum of the phase-coded MIMO radar in the water-droplet scenario, with targets at $-30°$ and $10°$.

MIMO framework respectively. The considered antenna responses include attenuation and distortion caused by bumper blockage, as well as additional degradation introduced by uniform water layers or discrete water droplets, with the line-of-sight subarray and an ideal ULA used as reference models. For each deterministic test, two angles were selected from the realized gain pattern for comparison: one corresponding to a local minimum (high-loss direction) and another corresponding to a comparatively higher gain direction (low-loss reference).

The Beamscan algorithm exhibited a strong correspondence between the realized gain pattern and the spatial response. At high-loss angles, signal attenuation led to reduced spatial spectrum peaks, resulting in degraded or ambiguous DoA estimates, indicating a high sensitivity to amplitude variations caused by environmental obstruction. In contrast, the MUSIC and MVDR algorithms showed a weaker one-to-one correspondence between realized gain degradation and deterministic DoA performance. Overall, MUSIC exhibits improved robustness under moderate attenuation. In several cases, these algorithms maintained distinguishable spatial spectrum peaks under noticeable rain-induced attenuation, although performance degradation was still observed under severe attenuation.

The ideal ULA model implemented in MATLAB provides the best overall DoA performance, while the subarray-based model achieves slightly degraded yet comparable results. For uniform water layer cases, different water layer thicknesses lead to similar DoA performance, consistent with the similar trends observed in the realized gain patterns. In contrast, for discrete water droplet cases, certain angular ranges show consistently poor performance across all scenarios, while noticeable differences are observed among different droplet configurations. These deterministic findings provide a foundation for the stochastic DoA analysis presented in Chapter 4.

4 Statistical Results and Comparative Analysis

4.1 Performance Evaluation

In the previous case study, the angle estimation algorithms were first tested using fixed, predetermined angles, allowing for a controlled evaluation of their basic functionality. This approach illustrates that the algorithms function correctly under controlled settings, although it does not comprehensively characterize their performance in more realistic scenarios characterized by random and arbitrary target angles.

To evaluate the accuracy of angle estimation in random angular settings, target azimuth angles are randomly and consistently generated within a detection range of $-60°$ to $60°$. Each test set comprises two target angles, with a total of 1000 test sets utilised, yielding $N_{\text{sample}} = 2000$ angle samples. The same estimation procedures, peak detection strategy, and parameter settings as those used in the fixed-angle analysis in Chapter 3 are employed here; the random-angle experiments simply repeat the estimation process over a large number of trials to obtain statistically meaningful results.

An angular-bin-based RMSE (root mean square error) analysis is first performed to investigate the angle-dependent characteristics of the estimate algorithms. The complete angular range is segmented into bins of $10°$ width, and the RMSE is calculated for each bin utilising the samples whose true angles reside within the respective angular interval. The bin-wise RMSE offers a localised assessment of estimate precision, facilitating the identification of angular regions prone to estimation inaccuracies. This analysis is crucial when water layers, droplets, and bumper structures are present, as propagation distortions and structural impacts may differentially affect various angular locations.

Following the angular-bin analysis, the overall estimation performance is evaluated using the RMSE and the MAE (mean absolute error) over all test samples. The RMSE is defined as follows: $\hat{\theta}_i$ represents the estimated angle of the i-th sample, and θ_i denotes the corresponding true angle.It should be noted that the value of N differs depending on the evaluation context. For the angular-bin based RMSE, N corresponds to the number of angle samples whose true angles fall within a specific angular bin. For the overall RMSE, N represents the total number of angle samples across all test sets, which is 2000 in this study.

$$\text{RMSE} = \sqrt{\frac{1}{N}\sum_{i=1}^{N}(\hat{\theta}_i - \theta_i)^2}, \tag{4.1}$$

and the MAE is given by

$$\text{MAE} = \frac{1}{N}\sum_{i=1}^{N}\left|\hat{\theta}_i - \theta_i\right|, \tag{4.2}$$

4.1.1 Beamscan Algorithm

The Beamscan algorithm estimates the angles of arrival by evaluating the spatial spectrum of the received signal. The resulting spectrum typically exhibits multiple peaks, corresponding to potential source directions, along with pronounced sidelobes. In our observations, a potentially largest sidelobe often occurs near -8 dB. To mitigate the effect of these sidelobes, a threshold of -8 dB is applied, and all peaks above this threshold are identified.

Among the identified peaks, the two with the largest amplitudes are selected as the estimated angles, since the estimator provides two measurements simultaneously. For example, if the estimated angles are $(\hat{\theta}_1, \hat{\theta}_2) = (-30^\circ, 20^\circ)$ and the corresponding true angles are $(\theta_1, \theta_2) = (-25^\circ, 23^\circ)$, the estimates are assigned to the true angles based on their relative magnitudes. That is, $\hat{\theta}_1$ is associated with θ_1 and $\hat{\theta}_2$ with θ_2. This assignment ensures a consistent calculation of RMSE and MAE across multiple realizations. In the worst-case scenario, when only a single peak exceeds the threshold, both estimated angles are assigned the value of this peak. This ensures that the RMSE and MAE can still be computed consistently, even when the spectrum does not provide two clearly resolvable peaks.

Antenna–bumper–water layer analysis

Figure 4.1 presents the RMSE across angular bins, providing a detailed view of estimation accuracy. Under ideal conditions with a uniform linear array (ULA), the estimator achieves minimal RMSE and MAE throughout the angular spectrum. The presence of the bumper and water layers increases errors in specific ranges, notably between -60° and -40° and 20° to 30°, with the largest deviations near the negative angular boundary. This pattern aligns with the realized gain in Figure 2.16c, which shows significant attenuation at the extremes and in the 20°–30° range. Moreover, the realized gain curves for different obstructed conditions nearly overlap, which explains why angular RMSE, overall MAE in Figure 4.2b, and RMSE in Figure 4.2a exhibit very similar values and trends, indicating that the observed metric behavior is consistent and reasonable.

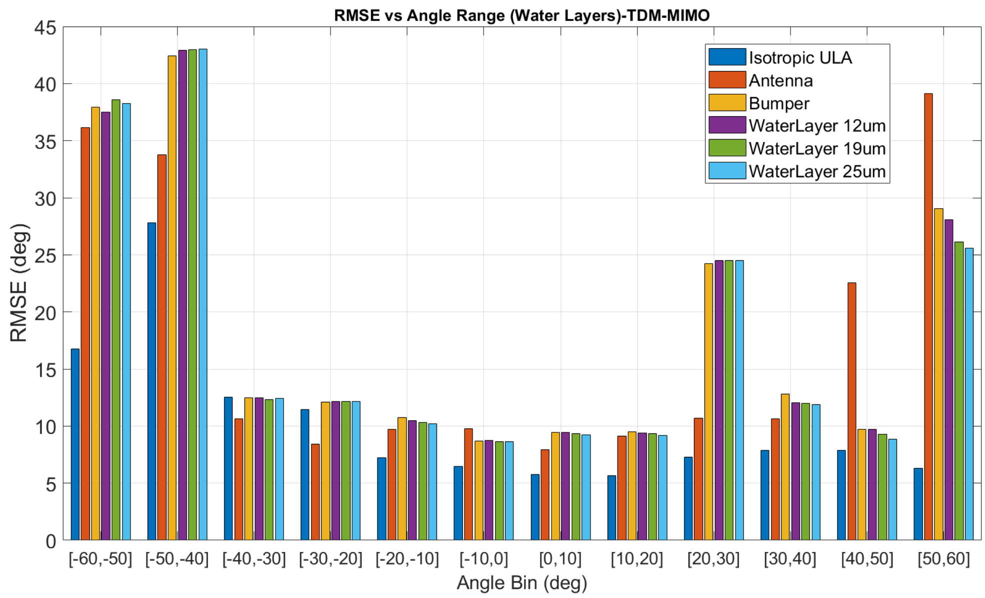

Figure 4.1: RMSE performance per angular bin using Beamscan with TDM MIMO radar under water-layer conditions.

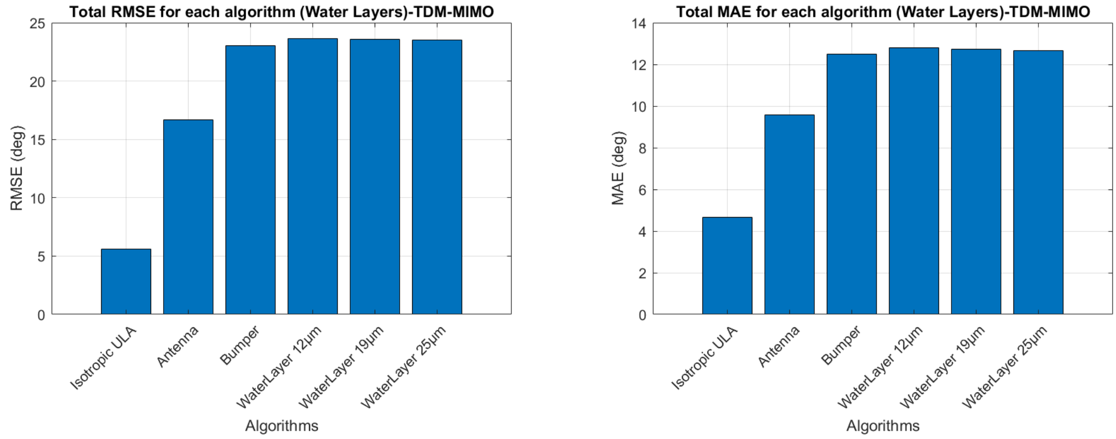

(a) RMSE (b) MAE

Figure 4.2: Performance comparison in terms of RMSE and MAE using Beamscan with TDM MIMO radar under water-layer conditions.

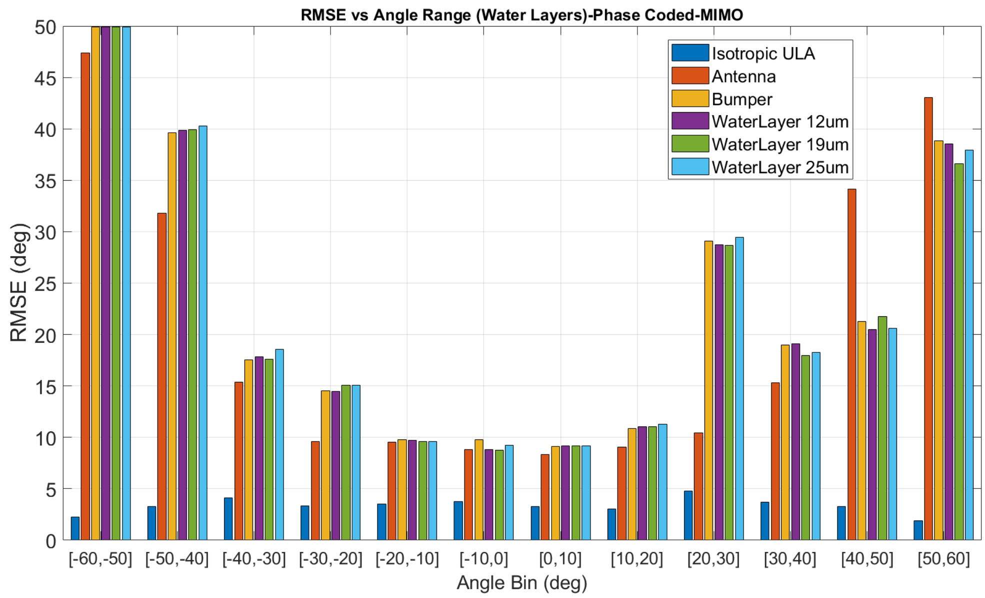

Figure 4.3: RMSE performance per angular bin using Beamscan with phase-coded MIMO radar under water-layer conditions.

Antenna–bumper–water droplets analysis

Figure 4.5 presents the RMSE across angular bins under water drop conditions. Compared to the water-layer cases, the overall deviations are larger, with particularly poor performance observed in the $-60°$ to $-40°$ and $20°$ to $30°$ bins. Among the four water-droplet scenarios, the first and third case exhibit trends akin to the others across the angular spectrum; yet, its RMSE is often markedly elevated, suggesting more severe estimating errors.

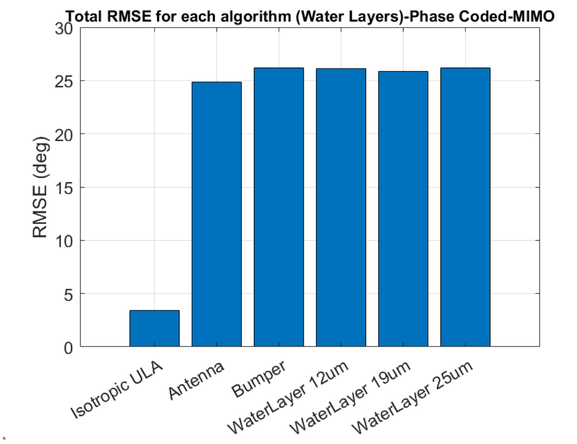

(a) RMSE

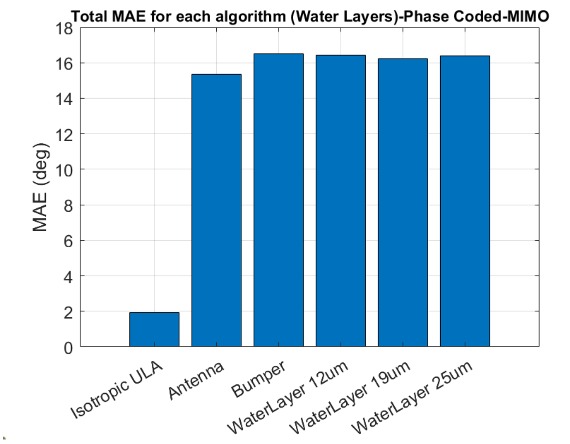

(b) MAE

Figure 4.4: Performance comparison in terms of RMSE and MAE using Beamscan with phase-coded MIMO radar under water-layer conditions.

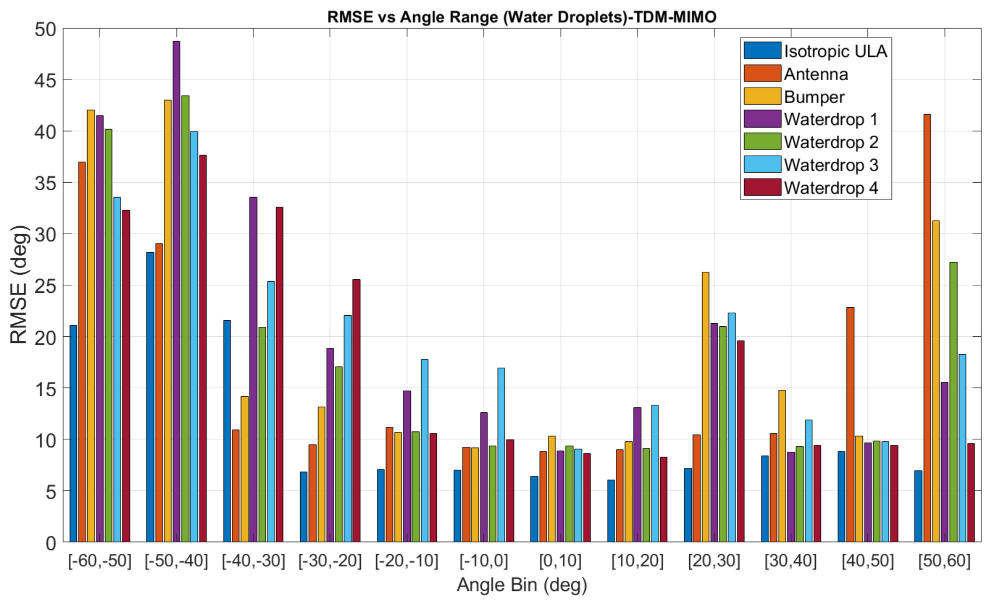

Figure 4.5: RMSE performance per angular bin using Beamscan with TDM MIMO radar under water-droplet conditions.

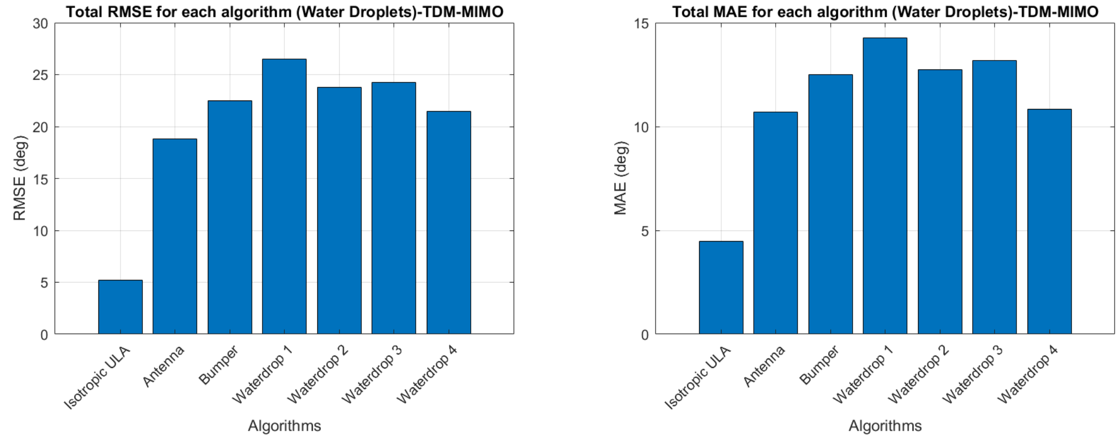

(a) RMSE (b) MAE

Figure 4.6: Performance comparison in terms of RMSE and MAE using Beamscan with TDM MIMO radar under water-droplet conditions.

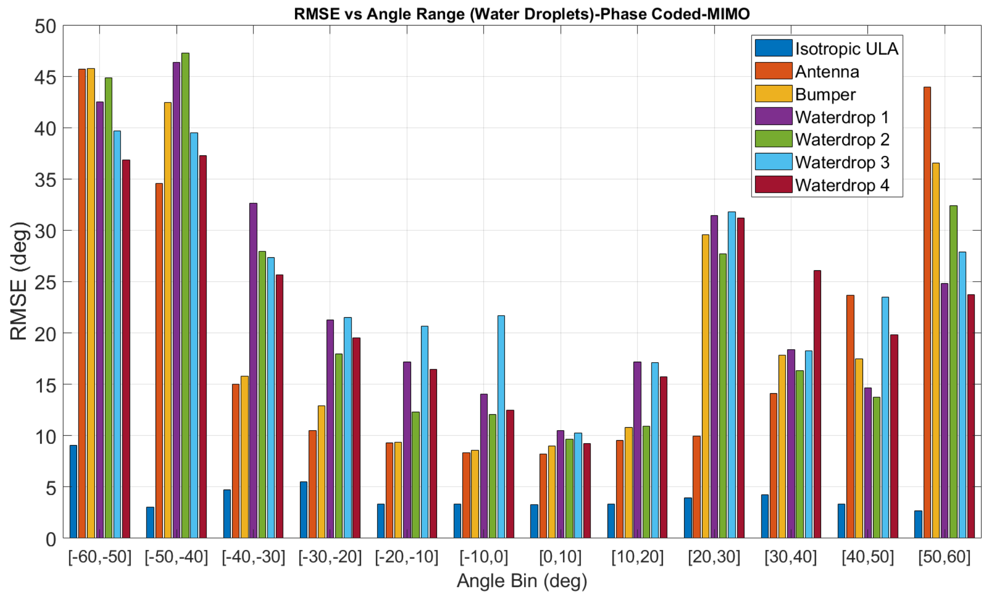

Figure 4.7: RMSE performance per angular bin using Beamscan with phase-coded MIMO radar under water-droplet conditions.

4.1.2 MUSIC Algorithm

The MUSIC algorithm generates sharper peaks that remain generally unaffected by adjacent interference. Therefore, no threshold is implemented; the angles associated with the two most prominent peaks are directly taken as the estimations. If a single peak is present, two identical estimates are assigned, as in the Beamscan method. In this project, spatial smoothing was applied to the array data to mitigate the effects of coherent sources and improve covariance matrix estimation, further enhancing the performance of MUSIC and achieving the best possible angular accuracy under the given conditions.

Figure 4.9 is the RMSE across bins for the TDM MIMO antenna. Examining the RMSE of MUSIC algorithm shows generally low values, with most bins around 4°, indicating good and fairly uniform angular resolution. In scenarios with the water layer, only two bins exceed RMSE of 15°, suggesting that the majority of angle estimates remain accurate. The bins with

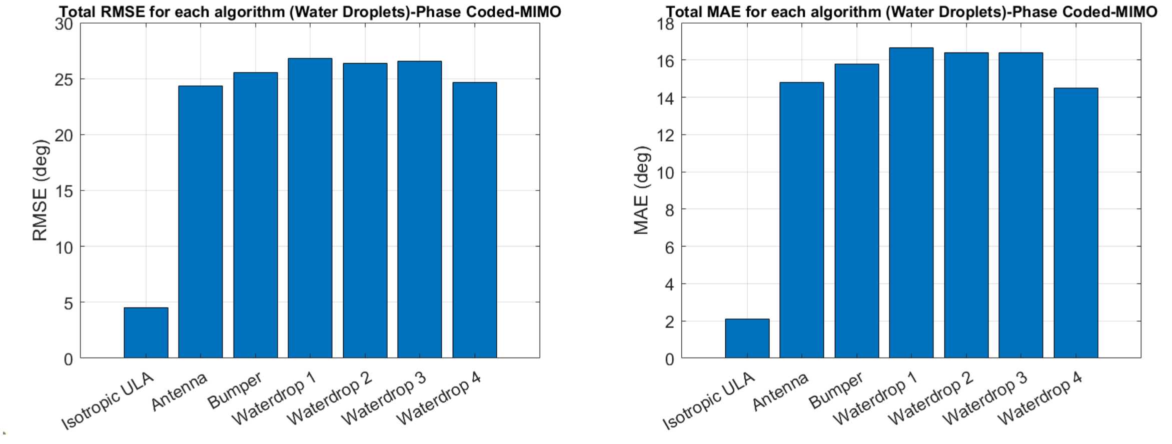

(a) RMSE (b) MAE

Figure 4.8: Performance comparison in terms of RMSE and MAE using Beamscan with phase-coded MIMO radar under water-droplet conditions.

the largest RMSE occur in the $-50°$ to $-40°$ and $-60°$ to $-50°$ regions, as well as $20°$ to $30°$, which correspond to areas of significant loss in the antenna's realized pattern (Figure 2.16c), explaining the localized increase in estimation error.

Regarding overall performance metrics as shown in Figure 4.10, both the overall RMSE and MAE are highly consistent between the cases with the bumper alone and with the bumper plus water layer obstructed subarray, with values less than $14°$ for the former and around $6°$ for the latter. This indicates that the overall angular estimation is robust to environmental variations such as blockage and partial signal attenuation. Comparisons with a ULA array reveal that the ideal ULA achieves an RMSE of approximately $3°$, demonstrating superior performance in ideal, unobstructed conditions. In contrast, arrays with obstructions yield an RMSE of about $7°$, which, while higher than TDM MUSIC under ideal conditions, remains within acceptable limits.

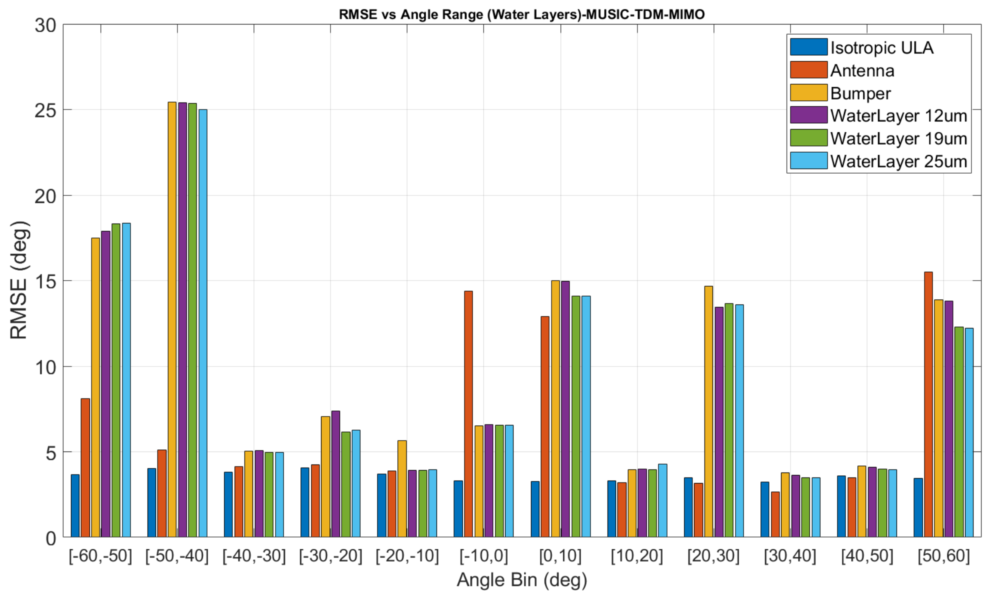

Figure 4.9: RMSE performance per angular bin using MUSIC with TDM MIMO radar under water-layer conditions.

Examining the RMSE across bins in Figure 4.11 for the Phase-Coded MUSIC algorithm shows

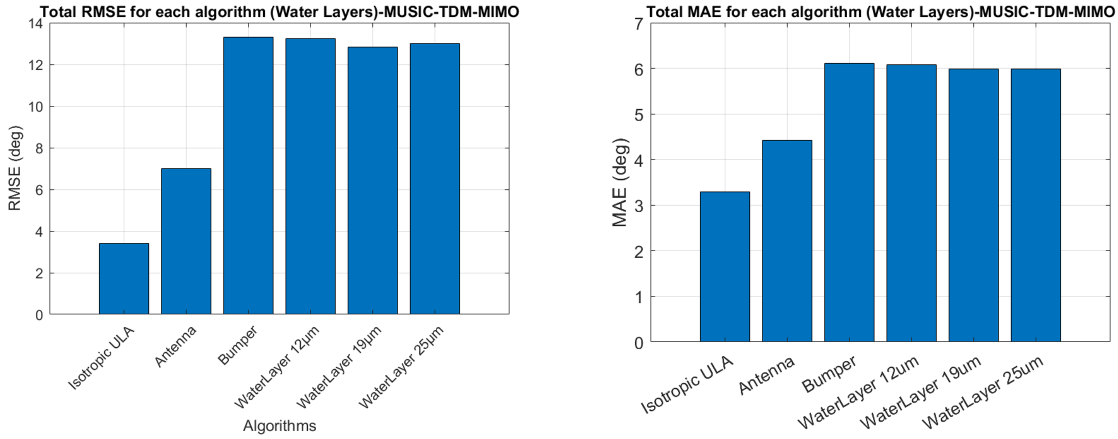

(a) RMSE (b) MAE

Figure 4.10: Performance comparison in terms of RMSE and MAE using MUSIC with TDM MIMO radar under water-layer conditions.

performance that is generally similar to the TDM case, but slightly better overall. Both the overall RMSE and MAE in Figure 4.12 are highly consistent between the cases except ULA or unobstructed antenna, with values less than 9° for the former and around 3° for the latter.

Angle-bin level RMSE remains relatively low in most regions, but noticeable increases are observed in the 20° to 30° and −60° to −50° ranges, similar to the TDM case. Additionally, the −30° to −20° region shows slightly degraded performance, which corresponds to a notch in the antenna's realized gain pattern. More pronounced degradation occurs in the 40° to 50° and 50° to 60° ranges, likely due to errors introduced by the Phase-Coded signal processing itself during the encoding and decoding stages. These errors can affect the MUSIC subspace decomposition. Further investigation of test sets covering this angular range revealed that, except for the ULA, other array configurations frequently miss a peak near 50°. The absence of a peak in these bins significantly increases the local RMSE, explaining the larger errors observed in this angular region.

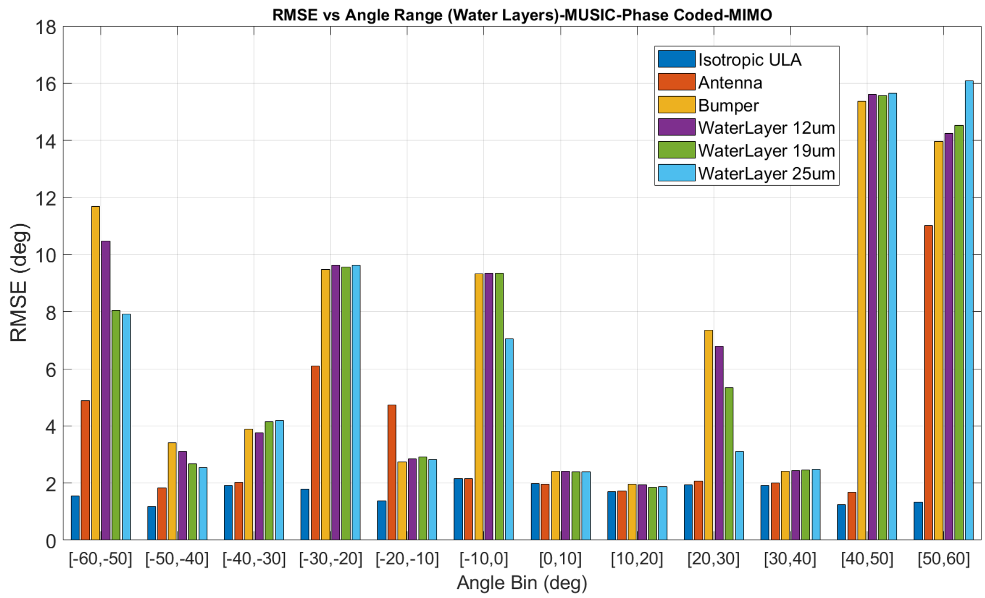

Figure 4.11: RMSE performance per angular bin using MUSIC with phase-coded MIMO radar under water-layer conditions.

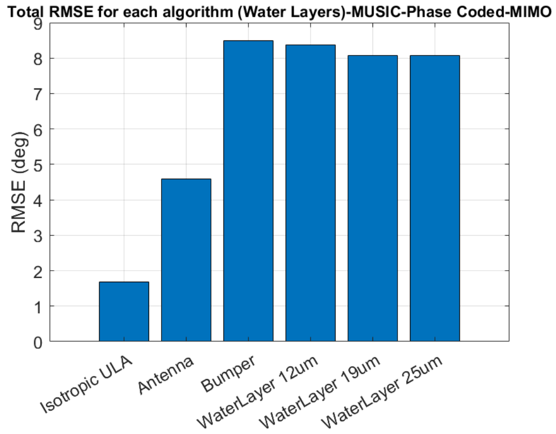

(a) RMSE

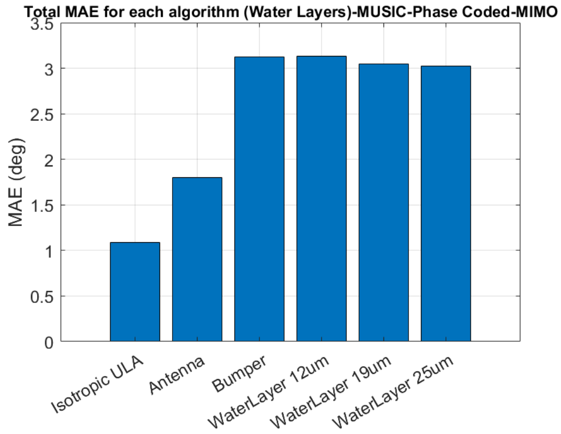

(b) MAE

Figure 4.12: Performance comparison in terms of RMSE and MAE using MUSIC with phase-coded waveform under water-layer conditions.

Examining the angle bin level RMSE for the TDM MUSIC algorithm in the water-droplet scenario in Figure 4.13, the worst performance occurs in the $-50°$ to $-40°$ range, with the most extreme case, water-droplet Case 1, reaching an RMSE of approximately 30°, which is rare among all MUSIC configurations. The next highest errors are observed in the $-60°$ to $-50°$ bins, again with water-droplet Case 1 performing worst. These regions correspond to a relatively wide loss area around $-47°$ in the antenna's realized pattern. Additional increases in RMSE are noted in the $-10°$ to 0° and 20° to 30° bins, which coincide with smaller notches in the realized gain in Figure 2.17c.

As a result of these localized errors, the overall RMSE is highest for water-droplet Case 1, approximately 13°, while other arrays with obstruction scenarios show overall RMSE values around 8°, which still represents reasonably good performance.

Figure 4.15 illustrates the performance of the Phase-Coded MUSIC algorithm in the water-droplet scenario. Overall, the algorithm maintains robust angular estimation, comparable to the water-layer scenario for the same MIMO configuration, with RMSE smaller than 11° for most cases as shown in Figure 4.16.

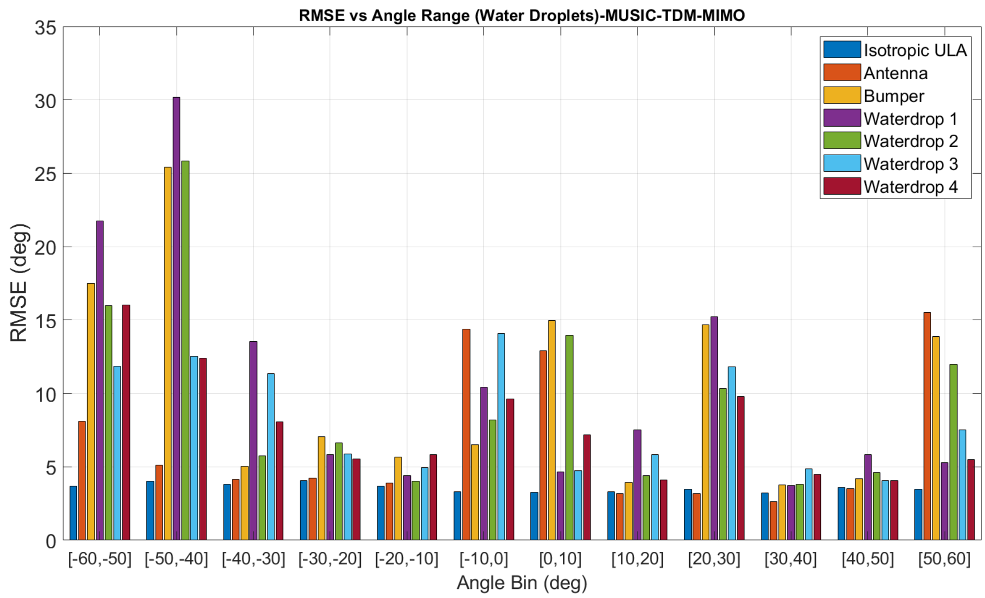

Figure 4.13: RMSE performance per angular bin using MUSIC with TDM MIMO radar under water-droplet conditions.

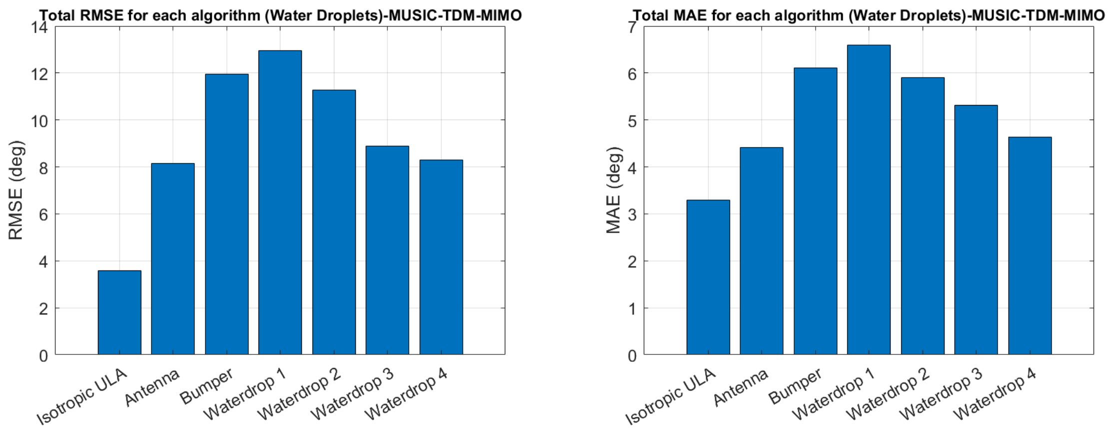

(a) RMSE

(b) MAE

Figure 4.14: Performance comparison in terms of RMSE and MAE using MUSIC with TDM MIMO radar under water-droplet conditions.

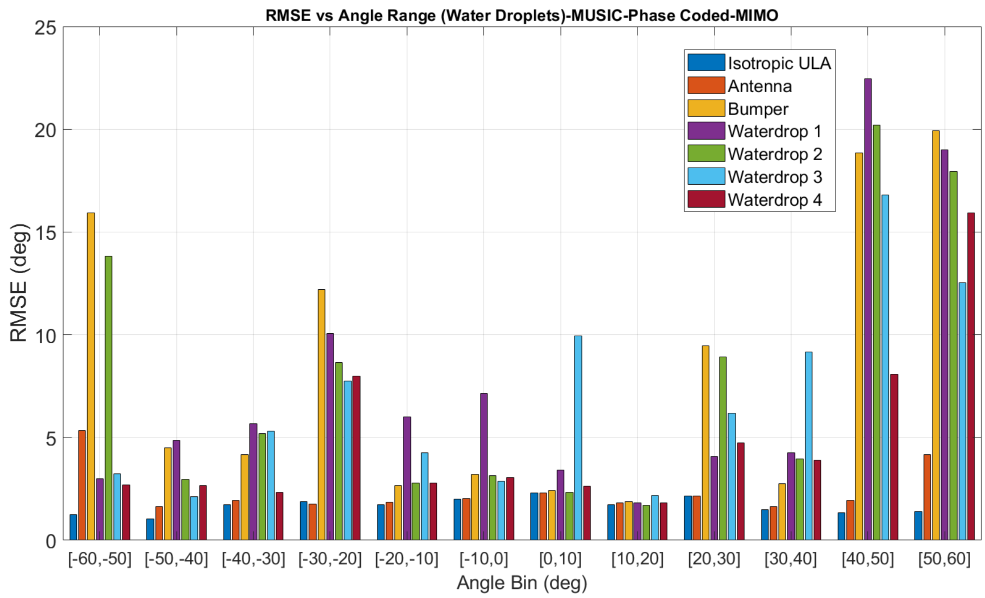

Figure 4.15: RMSE performance per angular bin using MUSIC with phase-coded MIMO radar under water-droplet conditions.

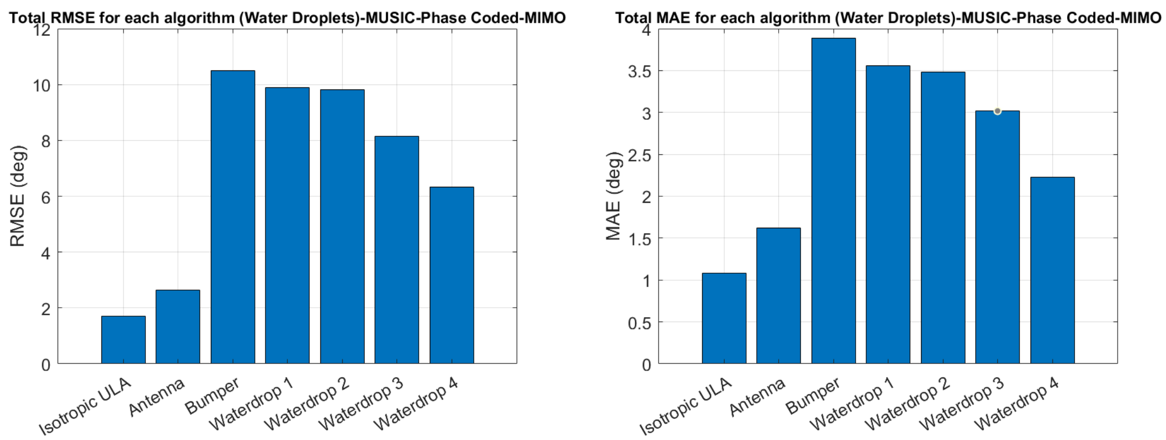

(a) RMSE

(b) MAE

Figure 4.16: Performance comparison in terms of RMSE and MAE using MUSIC with phase-coded waveform under water-droplet conditions.

4.1.3 MVDR Algorithm

In this section, the performance of the MVDR algorithm is evaluated for both TDM and Phase-Coded MIMO radar configurations under two propagation scenarios: water-layer and water-droplet conditions. Figures 4.17, 4.19, 4.21 and 4.23 present the bin-level RMSE. Figure 4.18, 4.20, 4.22 and 4.24 present the angle bin level RMSE and overall performance metrics (RMSE and MAE).

While MUSIC benefits from distinct peaks unaffected by neighboring interference, MVDR yields more continuous spectral patterns. Nonetheless, the identical peak-based methodology is employed: the prominent peaks in the MVDR response are identified, and the corresponding angles are regarded as estimates. The experimental results demonstrated that the MVDR angle spectrum for TDM MIMO displays prominent peaks, with two targets generating pronounced and closely spaced spectral peaks, thereby enabling precise peak detection by the algorithm. In contrast, Phase-Coded MIMO exhibits a greater variance in peak amplitudes between two targets. Despite the two peaks remaining visually distinct, establishing a singular threshold for the automatic filtration of spectral variations from non-target angles is challenging.

When two target peaks are distinctly separated, this effect has negligible influence on detection. While two targets are in close proximity, the MVDR spectrum may exhibit a singular dominant peak, with adjacent variations potentially misidentified as additional peaks by the algorithm, resulting in an elevated RMSE.

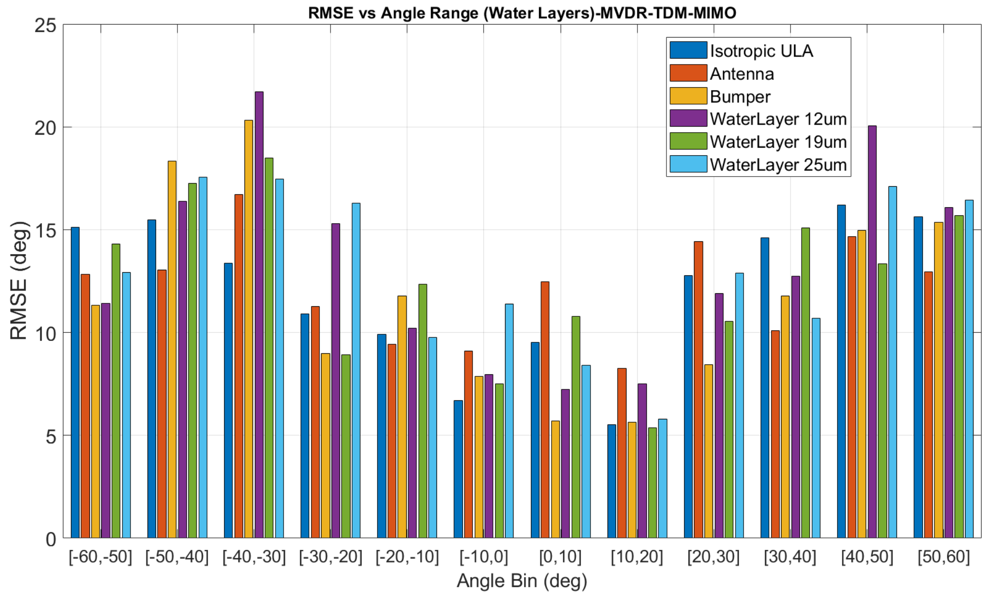

Figure 4.17: RMSE performance per angular bin using MVDR with TDM MIMO radar under water-layer conditions.

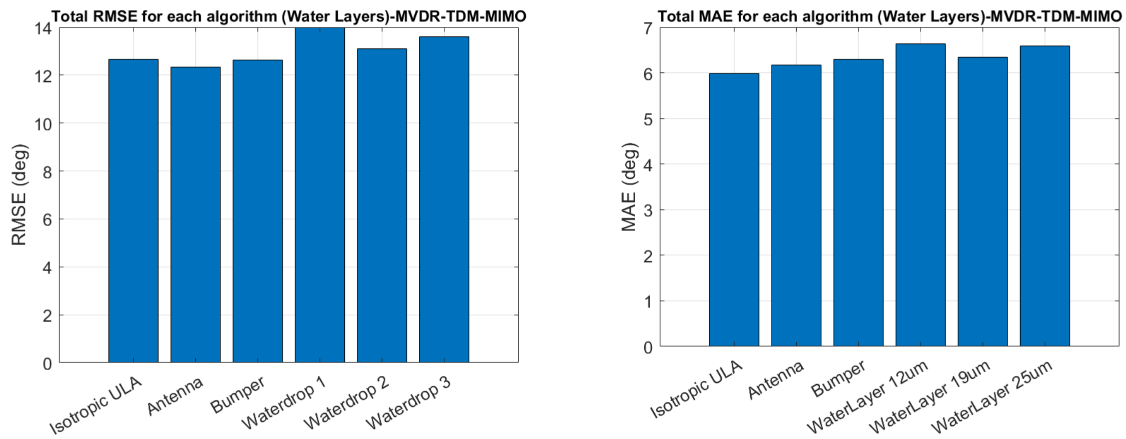

(a) RMSE

(b) MAE

Figure 4.18: Performance comparison in terms of RMSE and MAE using MVDR with TDM MIMO radar under water-layer conditions.

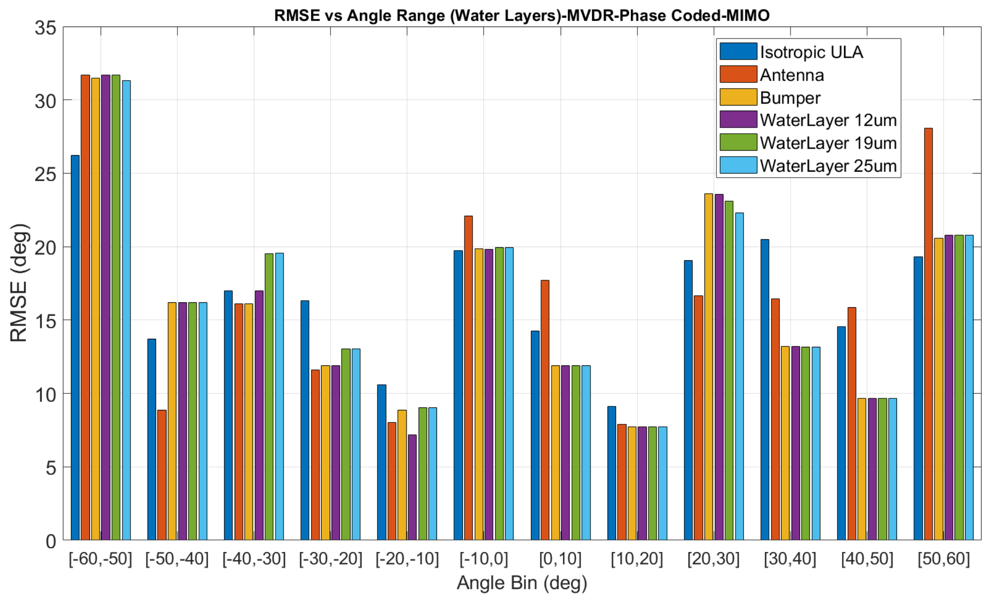

Figure 4.19: RMSE performance per angular bin using MVDR with phase-coded waveform under water-layer conditions.

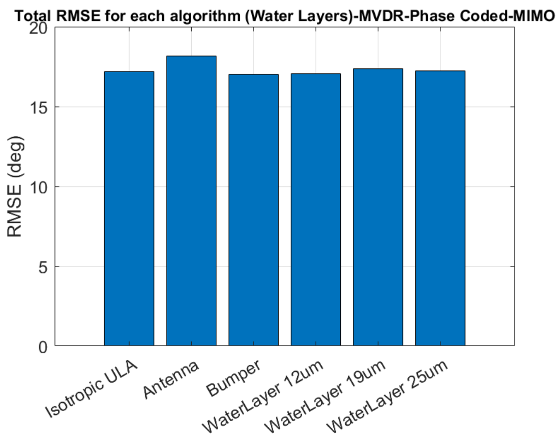

(a) RMSE

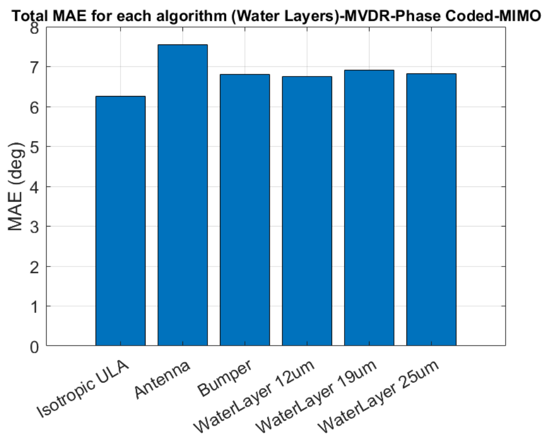

(b) MAE

Figure 4.20: Performance comparison in terms of RMSE and MAE using MVDR with phase-coded waveform under water-layer conditions.

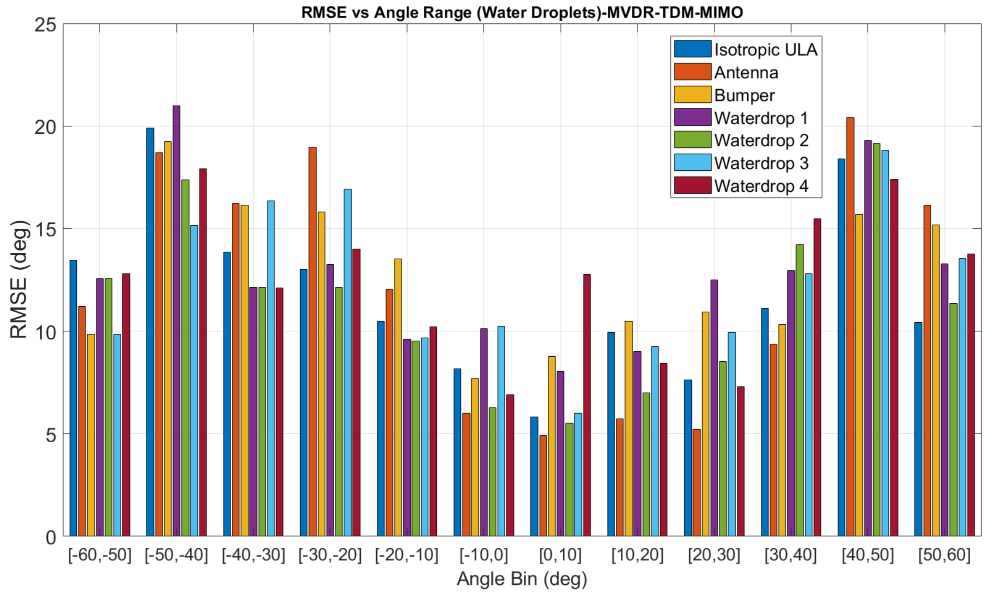

Figure 4.21: RMSE performance per angular bin using MVDR with TDM MIMO radar under water-droplet conditions.

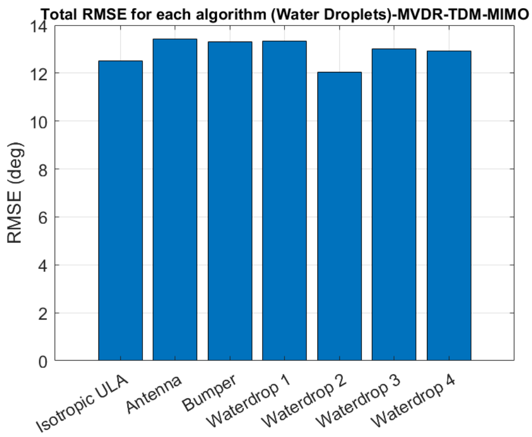

(a) RMSE

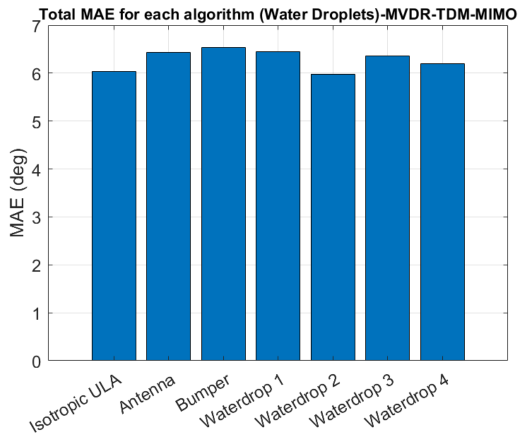

(b) MAE

Figure 4.22: Performance comparison in terms of RMSE and MAE using MVDR with TDM MIMO radar under water-droplet conditions.

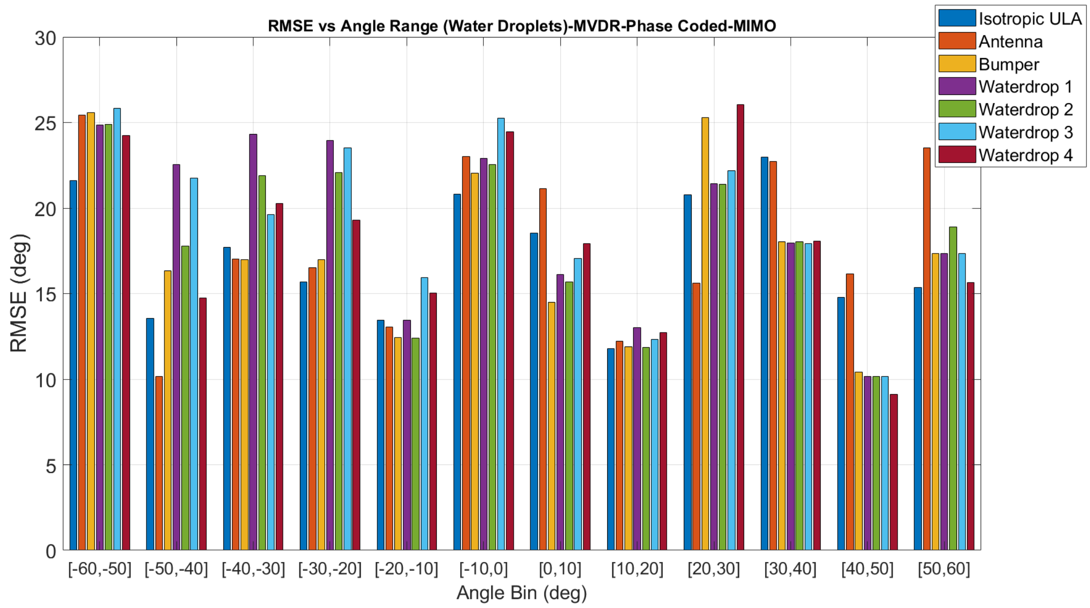

Figure 4.23: RMSE performance per angular bin using MVDR with phase-coded waveform under water-droplet conditions.

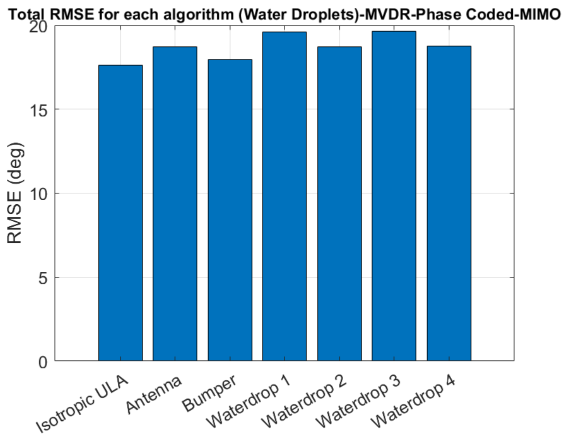

(a) RMSE

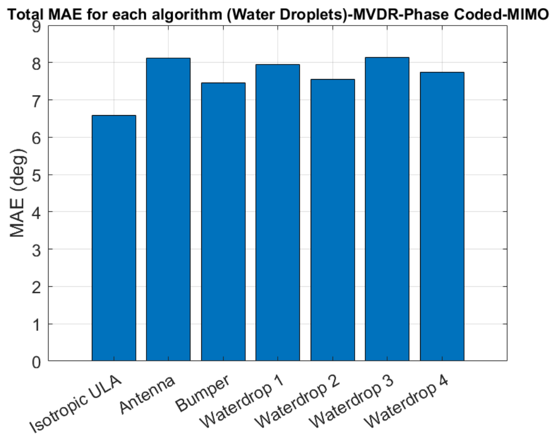

(b) MAE

Figure 4.24: Performance comparison in terms of RMSE and MAE using MVDR with phase-coded waveform under water-droplet conditions.

Quantitatively, the overall RMSE for TDM MVDR remains below 14° for both water-layer and water-droplet scenarios, with minimal difference between the two. For Phase-Coded MVDR, the overall RMSE is approximately 18° in both scenarios. While BeamScan exhibits good performance in most cases except ULA, the latter, used as a reference, performs poorly under MVDR, indicating that the algorithm's overall robustness is limited. Consequently, the influence of environmental factors such as bumpers or other propagation losses becomes less significant. These results highlight the necessity of adopting optimization strategies if MVDR is employed in practical scenarios.

4.1.4 Conclusion

The evaluation of TDM and Phase-Coded MIMO configurations using MUSIC, MVDR, and BeamScan algorithms demonstrates distinct performance characteristics under various environmental conditions. MUSIC consistently provides sharp and well resolved spectral peaks, enabling robust DoA estimation with low RMSE and minimal sensitivity to array blockage. MVDR produces smoother spectra and limited performance without additional optimization. Beamscan relies on peak thresholding (-8 dB) to mitigate sidelobe effects and generally performs well with ULA arrays under ideal conditions, but environmental obstructions introduce localized estimation errors, particularly in angular regions with reduced realized gain. Overall, MUSIC provides the best angular accuracy and stability across scenarios, whereas MVDR and BeamScan require careful tuning or array design considerations to maintain reliable performance in practical deployments. Table 4.1 compares the overall RMSE performance for different algorithms and MIMO configurations. Here, the "Obstructed Array" refers to array setups with a bumper induced blockage, including scenarios with and without additional water droplets. The values reported in Table 4.1 represent approximate RMSE and MAE measurements instead of strict bounds.

Table 4.1: Overall RMSE and MAE comparison for different algorithms, MIMO schemes, and array models

Algorithm	MIMO	Array Model	RMSE (°)	MAE (°)
BeamScan	TDM	ULA	5	5
		Unobstructed Array	19 – 20	9
		Obstructed Array	25	12-14
	Phase-Coded	ULA	5	2
		Unobstructed Array	24	15
		Obstructed Array	25	16
MUSIC	TDM	ULA	3	3
		Unobstructed Array	7	4
		Obstructed Array	13 – 14	6 – 7
	Phase-Coded	ULA	2	1
		Unobstructed Array	5	1.7
		Obstructed Array	8-12	3 – 4
MVDR	TDM	ULA	12	6-7
		Unobstructed Array	13 – 14	6-7
		Obstructed Array	13 – 14	6-7
	Phase-Coded	ULA	17	6
		Unobstructed Array	18	7
		Obstructed Array	19 – 20	7

4.2 Conclusion and Recommendations for Future Work

This thesis examined the effects of realistic electromagnetic deterioration, such as bumper obstruction and rainwater deposition, on car radar Direction of Arrival estimation. Prior research frequently presumed optimal antenna arrays and neglected to consider environmental impairments, resulting in a deficiency in comprehending the impact of amplitude attenuation and phase distortion on algorithmic efficacy. The proposed methodology presents a comprehensive EM algorithm evaluation framework, incorporating high-fidelity realised gain patterns directly into FMCW MIMO radar simulations and assessing Beamscan, MUSIC, and MVDR under both deterministic and stochastic scenarios.

The methodology was executed in three phases: initially, CST modelling of antennas and bumpers that included water-layer and droplet effects; subsequently, a deterministic analysis of Direction of Arrival (DoA) performance at typical high- and low-gain angles; and finally, statistical simulations of Root Mean Square Error (RMSE) and Mean Absolute Error (MAE) to evaluate algorithm robustness amidst environmental variability.

The findings indicate that Beamscan is significantly influenced by amplitude loss, displaying considerable errors at low-gain angles, hence validating its susceptibility to environmental attenuation noted in deterministic simulations. Conversely, MUSIC regularly attains the lowest RMSE and MAE, exhibiting significant resilience to partial signal degradation owing to its subspace-based processing and spatial smoothing techniques. MVDR exhibits optimal performance with well-separated targets but demonstrates heightened susceptibility to closely spaced targets and spatial sidelobe variations, especially during Phase-Coded MIMO operation.

Comparisons with prior studies validate that including realistic antenna effects yields a more precise and quantitative assessment than presuming ideal arrays, underscoring the robustness of MUSIC and the susceptibility of Beamscan. The proposed methodology offers a replicable pipeline that connects EM-level antenna deterioration to both deterministic and stochastic DoA performance, offering a useful tool for algorithm assessment and radar system design in actual automotive settings.

The framework can be expanded to accommodate dynamic environmental conditions, implement adaptive algorithmic compensation, integrate comprehensive radar systems and utilise computational optimisation through surrogate models, thereby augmenting the predictive capability and applicability of the evaluation framework.

Bibliography

[1] T. Neumann, “Analysis of advanced driver-assistance systems for safe and comfortable driving of motor vehicles,” *Sensors*, vol. 24, no. 19, 2024. [Online]. Available: https://www.mdpi.com/1424-8220/24/19/6223

[2] J. Nidamanuri, C. Nibhanupudi, R. Assfalg, and H. Venkataraman, “A progressive review: Emerging technologies for adas driven solutions,” *IEEE Transactions on Intelligent Vehicles*, vol. 7, no. 2, pp. 326–341, 2022.

[3] Z. Peng, C. Li, and F. Uysal, *Modern Radar for Automotive Applications*. The Institution of Engineering and Technology, 2022. [Online]. Available: https://digital-library.theiet.org/doi/abs/10.1049/SBRA553E

[4] Y. Xiao, F. Norouzian, E. Hoare, E. Marchetti, M. Gashinova, and M. Cherniakov, “Modeling and experiment verification of transmissivity of low-thz radar signal through vehicle infrastructure,” *IEEE Sensors Journal*, vol. PP, pp. 1–1, 03 2020.

[5] V. Winkler, “Range doppler detection for automotive fmcw radars,” in *2007 European Microwave Conference*, 2007, pp. 1445–1448.

[6] D. Johnson and D. Dudgeon, *Array Signal Processing: Concepts and Techniques*, ser. Prentice-Hall signal processing series. P T R Prentice Hall, 1993. [Online]. Available: https://books.google.nl/books?id=v_NSAAAAMAAJ

[7] I. Expósito, I. Chin, M. García Sánchez, I. Cuiñas, and J. Verhaevert, “Car bumper effects in adas sensors at automotive radar frequencies,” *Sensors*, vol. 23, no. 19, 2023. [Online]. Available: https://www.mdpi.com/1424-8220/23/19/8113

[8] H. Wonnemann, *Primer Surfacer, in Automotive Paints and Coatings*. John Wiley & Sons, Ltd, 2008, ch. 5, pp. 129–174. [Online]. Available: https://onlinelibrary.wiley.com/doi/abs/10.1002/9783527622375.ch5

[9] K.-F. Dössel, *Top Coats, in Automotive Paints and Coatings*. John Wiley & Sons, Ltd, 2008, ch. 6, pp. 175–210. [Online]. Available: https://onlinelibrary.wiley.com/doi/abs/10.1002/9783527622375.ch6

[10] J. C. Dash and D. Sarkar, “Impacts on automotive mimo radar performance due to permittivity variation of bumper material: Insights through bi-directional loss and antenna array ambiguity function,” in *2021 IEEE MTT-S International Microwave and RF Conference (IMARC)*, 2021, pp. 1–4.

[11] D. Schwarz, M. Linder, R. Riekenbrauck, R. Bord, and C. Waldschmidt, “Effects of bumper integration on low-, mid-, and high-resolution imaging radars,” in *2024 18th European Conference on Antennas and Propagation (EuCAP)*, 2024, pp. 1–5.

[12] N. Modi, B. M. Kumar, and J. Mukherjee, “Analysis of the effects of rainwater covered bumper on the automotive radar signals,” in *2024 18th European Conference on Antennas and Propagation (EuCAP)*, 2024, pp. 1–5.

[13] J. C. Dash, M. Parikh, N. Modi, J. Mukherjee, S. VR, T. SaiDeepak, and V. Dhoot, "Performance evaluation of automotive radar in the presence of bumper with multiple paint layers using bidirectional loss model," in *2021 15th European Conference on Antennas and Propagation (EuCAP)*, 2021, pp. 1–5.

[14] C. Winter, M. Korff, T. Fabbri, S. Holzknecht, I. Weber, and E. M. Biebl, "Permittivity determination method for multilayer automotive coatings for radar applications at 77 ghz," *IEEE Transactions on Microwave Theory and Techniques*, vol. 70, no. 4, pp. 2380–2388, 2022.

[15] Y. Xiao, F. Norouzian, E. Hoare, E. Marchetti, M. Gashinova, and M. Cherniakov, "Modeling and experiment verification of transmissivity of low-thz radar signal through vehicle infrastructure," *IEEE Sensors Journal*, vol. PP, pp. 1–1, 03 2020.

[16] E. Emilsson, "Radar transparency and paint compatibility a study of automobile bumper and bumper-skin complex permittivities for 77ghz microwaves," Ph.D. dissertation, 07 2019.

[17] R. O. Schmidt, "A signal subspace approach to multiple emitter location and spectral estimation," Ph.D. Dissertation, Stanford University, Stanford, CA, 1982, department of Electrical Engineering.

[18] R. Roy and T. Kailath, "Esprit-estimation of signal parameters via rotational invariance techniques," *IEEE Transactions on Acoustics, Speech, and Signal Processing*, vol. 37, no. 7, pp. 984–995, 1989.

[19] R. Roy, A. Paulraj, and T. Kailath, "Direction-of-arrival estimation by subspace rotation methods - esprit," in *ICASSP '86. IEEE International Conference on Acoustics, Speech, and Signal Processing*, vol. 11, 1986, pp. 2495–2498.

[20] S. Peng, B. X. Chen, and S. Q. Xu, "Gridless 2d doa estimation for sparse planar arrays via 2-level toeplitz reconstruction," *Signal Processing*, vol. 226, Jan 2025.

[21] H. Ruan, S. Balon, J. Wu, Q. Liu, J. Sun, and X. Wu, "A joint design of sparse array layout and doa algorithm for mmwave fmcw radar," in *2024 IEEE Radar Conference (RadarConf24)*, vol. 54. IEEE, 2024, pp. 1–6.

[22] H. Zheng, Z. Shi, C. Zhou, and A. L. de Almeida, "Coarray tensor completion for doa estimation," *IEEE Transactions on Aerospace and Electronic Systems*, vol. 59, no. 5, pp. 5472–5486, 2023.

[23] R. Zheng, S. Sun, H. Liu, H. Chen, and J. Li, "Interpretable and efficient beamforming-based deep learning for single snapshot doa estimation," *IEEE Sensors Journal*, 2023.

[24] P. Chen, Z. Cao, Z. Chen, and X. Wang, "Off-grid doa estimation using sparse bayesian learning in mimo radar with unknown mutual coupling," *IEEE Transactions on Signal Processing*, vol. 67, no. 1, pp. 208–220, 2018.

[25] Facfox. (n.d.) 8 key points you must know when designing the front bumper of your car. [Online; accessed 29-Sep-2025]. [Online]. Available: https://facfox.com/docs/kb/8-kep-points-you-must-know-when-designthe-front-bumper-of-your-ca

[26] H. Liebe, G. Hufford, and T. Manabe, "A model for the complex permittivity of water at frequencies below 1 thz," *International Journal of Infrared and Millimeter Waves*, vol. 12, pp. 659–675, 01 1991.

[27] MathWorks. (2025) Increasing angular resolution with mimo radars. MATLAB Phased Array Toolbox example, accessed Jan. 10, 2026. [Online]. Available: https://ww2.mathworks.cn/help/phased/ug/increasing-angular-resolution-with-mimo-radars.html

[28] *Parameter Estimation II*. John Wiley & Sons, Ltd, 2002, ch. 9, pp. 1139–1317. [Online]. Available: https://onlinelibrary.wiley.com/doi/abs/10.1002/0471221104.ch9

[29] *Optimum Waveform Estimation*. John Wiley & Sons, Ltd, 2002, ch. 6, pp. 428–709. [Online]. Available: https://onlinelibrary.wiley.com/doi/abs/10.1002/0471221104.ch6